NIST Technical Note
NIST TN 2269

Analysis of a Steel Gravity Frame with Composite Floor System Subjected to Compartment Fire (Test #2)

Mohammed A. Morovat
Joseph A. Main
Jonathan M. Weigand
Malcolm L. Ammons
Fahim H. Sadek
Long T. Phan

This publication is available free of charge from:
https://doi.org/10.6028/NIST.TN.2269

NATIONAL INSTITUTE OF
STANDARDS AND TECHNOLOGY
U.S. DEPARTMENT OF COMMERCE

NIST Technical Note
NIST TN 2269

Analysis of a Steel Gravity Frame with Composite Floor System Subjected to Compartment Fire (Test #2)

Mohammed A. Morovat, Joseph A. Main, Jonathan M. Weigand
Malcolm L. Ammons, Fahim H. Sadek, Long T. Phan
Materials and Structural Systems Division
Engineering Laboratory

This publication is available free of charge from:
https://doi.org/10.6028/NIST.TN.2269

October 2023

U.S. Department of Commerce
Gina M. Raimondo, Secretary

National Institute of Standards and Technology
Laurie E. Locascio, NIST Director and Under Secretary of Commerce for Standards and Technology

NIST TN 2269
October 2023

The policy of the National Institute of Standards and Technology is to use metric units in all its published materials. Because this report is intended for the U.S. building construction industry, in some cases U.S. customary units are used.

NIST Technical Series Policies

Publication History

Approved by the NIST Editorial Review Board on 2023-09-28

How to Cite this NIST Technical Series Publication

Morovat, M.A., Main, J.A., Weigand, J.M., Ammons, M.L., Sadek, F.H. and Phan, L.T. (2023) Analysis of a Steel Gravity Frame with Composite Floor System Subjected to Compartment Fire (Test #2). (National Institute of Standards and Technology, Gaithersburg, MD), NIST Technical Note (TN) NIST TN 2269. https://doi.org/10.6028/NIST.TN.2269

NIST Author ORCID iDs

Mohammed A. Morovat: 0000-0002-2691-6151
Joseph A. Main: 0000-0003-0621-3137
Jonathan M. Weigand: 0000-0002-6938-6197
Malcolm L. Ammons: 0000-0003-2033-9936
Fahim H. Sadek: 0000-0002-0424-5799
Long T. Phan: 0009-0009-4322-6193

Abstract

This report describes the development and validation of a computational modeling approach for steel gravity frames with composite floor systems subjected to fire exposure. A full-scale compartment fire test conducted on a two-story steel gravity frame structure with a composite concrete floor slab on steel decking was used in the validation process. The experiment was conducted under combined mechanical and fire loading in the National Fire Research Laboratory (NRFL) at the National Institute of Standards and Technology (NIST). The intent of the experiment was to evaluate the influence of the slab reinforcement on the structural performance of the composite floor assembly, which incorporated deformed steel reinforcing bars in contrast with the welded wire reinforcement used in the previous test in the series. The objective of the computational investigation, summarized in this report, was to validate the adequacy of the computational modeling approach to capture the primary structural behaviors and failure modes observed during the fire test conducted in the NIST NFRL and to provide additional insights into the structural performance through detailed modeling of the system response. The computational model of the composite floor system was developed using the LS-DYNA finite element software and incorporated detailed modeling of the system components, including the lightweight reinforced concrete floor slab on profiled steel decking, primary and secondary steel beams and supporting columns, shear stud connectors, and bolted steel shear connections. The model adequately predicted the large deformations observed in the fire test of the composite floor assembly and captured their predominant deformation mechanisms, including lateral distortional buckling of the steel beams supporting the composite floor. Results from this study can further implementation of the performance-based design approaches for structural-fire safety in the U.S. and worldwide.

Keywords

composite floor system; composite slab; steel-framed building; membrane action; simulation; structural analysis; thermal bowing; thermal restraint; thermomechanical analysis; reduced-order model for composite slab; shell element; validation; explicit analysis; LS-DYNA; elevated temperatures; fire resistance; compartment fire; ASTM E119; standard fire exposure.

Table of Contents

List of Tables

List of Figures

Preface

The study summarized in this report is part of a comprehensive multi-year research project being carried out at NIST on the development and validation of modeling approaches for performance-based design of structures subject to fire exposure. This project has been carried out in close coordination with a series of full-scale experiments in the National Fire Research Laboratory (NFRL) at NIST, in which steel gravity frames with composite floor systems were tested under combined fire exposure and mechanical loading. This report presents the first phase in a comparison of computational model results with experimental measurements from this test series, focusing on the second composite floor test specimen, designated CF2. In this first phase, experimentally measured temperatures were prescribed as nodal temperature histories in the computational model, and a temperature-dependent structural analysis was performed rather than a coupled thermal-structural analysis. This approach eliminated the need to account for the significant uncertainties associated with the heat transfer analysis, including the significant variability in the thermal properties of spray-applied fire-resistive materials (SFRM), thus allowing the validation of the modeling approach to focus on the temperature-dependent structural response to the fire-induced heating. However, the computational modeling approach presented in this study is suitable for coupled thermal-structural analysis, and future analyses will consider heat transfer analysis in conjunction with the structural analysis.

Future phases of the project will focus on further verification and validation of the proposed computational approach, using data from other tests in the NFRL composite floor test series (CF1 and CF3 Tests). The approach will then be used to conduct parametric studies to examine a wide range of parameters that impact both thermal and structural analysis, including variations in thermal and mechanical properties of structural and insulation materials subjected to elevated temperatures in both the heating and cooling stages of a fire. The validated computational approach will further be used to provide a better understanding of the contribution of columns and the thermal restraint provided by the cooler parts of the structure to the overall stability of the composite floor systems exposed to fire. The ultimate goal of the project is to produce experimentally validated computational tools and technical guidance to enable the development of performance-based standards for the cost-effective fire resistance design and assessment of structures.

Executive Summary

This report describes the development and validation of a computational modeling approach for steel gravity frames with composite floor systems subjected to fire exposure. A full-scale compartment fire test conducted on a two-story steel gravity frame structure with a composite lightweight reinforced concrete floor slab on steel decking was used in the validation process. The experiment was conducted under combined mechanical and fire loading in the NFRL at NIST. This test was the second in a series of three large-scale experiments conducted in the NFRL to evaluate how the fire resistance of full-scale composite floor systems is influenced by several factors, including the slab reinforcement details, the application scheme of spray-applied fire-resistive materials (SFRM) on the steel beams, and the details of the structural framing layout, including the type of bolted steel shear connections at the beam ends. The intent of this second test in the series (CF2 Test) was to evaluate the influence of the slab reinforcement on the structural performance of the composite floor assembly, which incorporated deformed steel reinforcing bars in contrast with the welded wire reinforcement used in the first test [Ramesh and Choe 2022]. The objective of the computational investigation, summarized in this report, is to validate the adequacy of the computational modeling approach to capture the primary structural behaviors and failure modes observed during the test and to provide additional insights into the structural performance through detailed modeling of the system response.

The computational model of the composite floor system was developed using LS-DYNA finite element software [LSTC 2016] and incorporated detailed modeling of the system components, including the lightweight reinforced concrete floor slab on profiled steel decking, primary and secondary steel beams (referred to as, respectively, girders and beams in this report) and supporting columns, shear stud connectors, and bolted steel shear connections. The steel beams, girders, and columns were modeled using shell elements. Shear studs and bolts were modeled with solid elements, using a macro-modeling approach in which a single solid element was used to represent each component, with stress-strain relationships calibrated to provide a specified load-deformation response. A reduced-order modeling approach, using alternating strips of shell elements to represent the thick and thin sections of the slab, was used to model the composite slab including the concrete slab, reinforcement, and profiled steel decking. Welds were modeled

as rigid links in the analysis, as weld failure modes were deemed not to govern the connections behavior in the test structure.

Temperature-dependent material properties for structural steel, shear studs, bolts, and the composite slab were explicitly considered in the computational model. The reductions in both strength and stiffness, as well as nonlinear stress-strain behavior, were considered in material characterization at elevated temperatures. More specifically, temperature-dependent mechanical properties were defined for different types of structural steel (ASTM A992 steel [ASTM International 2022a] for wide-flange sections and A36 steel [ASTM International 2019] for plates). Building on previous studies at NIST [Seif et al. 2016a and Seif et al. 2016b], an enhanced temperature-dependent stress-strain model was developed that uses a power-law formulation to achieve specified values of yield strength, ultimate strength, and the uniform strain at the onset of necking. Further, using the component-based connection modeling approach, a temperature-dependent mechanical model was developed for structural bolts as elements of the single-plate shear (shear tab) connections. Additionally, temperature-dependent stress-strain curves for shear studs were developed through a process involving the modification of an ambient-temperature load-slip model for shear studs for elevated-temperature conditions, and the calibration of the computational model of a single shear stud to match the load-slip data at different temperatures. An empirical load-slip model proposed by Ollgaard et al. [Ollgaard et al. 1971] for shear studs at ambient temperature was utilized in developing the material model for shear studs at elevated temperatures. Finally, the mechanical behavior of the composite slab at high temperatures of fire was established using stress-strain curves for concrete and steel at ambient and elevated temperatures from the Eurocode 2 (EC2) [EN 1992-1-2 2004]. Fracture of the bolts, shear studs, and steel reinforcing bars was modeled using a strain-based failure criterion in which a temperature-independent plastic strain at failure was specified for each component. Fracture was not considered for the ASTM A992 [ASTM International 2022a] and ASTM A36 [ASTM International 2019] structural steel components, because fracture of the bolted connections was deemed to be the governing failure mode.

The applied loads and temperatures in the computational model of the composite floor test closely followed the mechanical and thermal loads in the experiments. Mechanical loads (both external and gravity loads) were applied as point loads distributed on the composite slab in both the test bay and the surrounding areas. To model the thermal loading resulting from the compartment fire exposure, the temperature histories recorded at different locations on the composite floor and the steel frame during the fire test were specified as nodal temperature histories in the computational model. While the modeling approach used in this study is suitable for coupled thermal-structural analysis [Main et al. 2017, Jiang et al. 2020b], direct specification of nodal temperatures eliminated the need to conduct a heat transfer analysis and to account for all the uncertainties associated with such analysis, including the significant variability in the thermal properties of SFRM [Zhang et al. 2021]. This approach allowed the validation of the modeling approach to focus on the temperature-dependent structural response to the fire-induced heating. The scope of the modeling validation was further limited to rising fire temperatures up to the maximum gas temperature recorded in the CF2 Test.

The structural analysis of the composite steel frame in the fire was performed using the explicit algorithm in LS-DYNA software [LSTC 2016]. The analysis and validation were conducted for the heating phase of the fire up to the maximum upper-layer gas temperature achieved in the NIST NFRL CF2 Test. Geometric and material nonlinearities and contact between structural components of the composite floor system were accounted for in the analysis. Thermal material softening and deformations associated with thermal expansion were also accounted for in the simulation.

Analysis results, presented and discussed in this report, demonstrated that the computational model was able to capture the large deformations of the composite floor assembly and the resulting failure mechanisms, including the lateral distortional buckling of supporting steel beams and out-of-plane bending of the shear plates in the extended shear tab connections. The validated model was used to further expand observations from the NIST NFRL CF 2 Test, by allowing for the examination of stresses in bolts and axial forces in secondary beams that were not directly measured during the test. The modeling methodology and its results presented in this report can be used to further inform the implementation of the performance-based design approach for structural-fire safety.

1. Introduction

1.1. Background

The applicability of standard fire resistance ratings in predicting the complex behavior of steel frames with composite floor systems in fire has been a subject of ongoing research for decades. These research studies stemmed from observations in building fire incidents where the performance of steel framed buildings with composite floors differed from that prescribed by standard fire resistance ratings (e.g., the Broadgate Phase 8 fire [Mwangi 2017]). These differences are attributed to the system-level behavior, involving the tensile membrane action of composite slab related to restraint to thermal expansion and the role of connections in the overall stability of steel frames with composite floors in fire. This system-level behavior is not captured in standard fire resistance tests of individual structural components or sub-assemblies.

To address the potential shortcomings of the standard fire resistance rating tests to adequately reflect the behaviors and performance of steel-framed buildings with composite floors in fire, sub-assembly and large-scale structural fire tests have been conducted around the world (e.g., The Cardington tests [British Steel 1999], FRACOF project [Wald et all 2006], COSSFIRE project [Breunese et all 2011]). Both standard and non-standard fire exposures were investigated in the experiments.

Another experimental program included a series of three full-scale fire tests conducted at the NIST NFRL on composite floor systems subjected to compartment fires. The main intent of this experimental program was to study the system behavior of the composite floor systems, with different slab reinforcement details and different amounts of spray-applied fire-resistive materials (SFRM) on supporting beams, exposed to large enclosure fires that closely resemble the standard fire exposure defined in ASTM E119 [ASTM International 2022c]. The shear-tab beam-to-column, beam-to-girder, and girder-to-column connections were the same in the three tests conducted at the NIST NFRL. A gravity steel-framed, two-story building with three large replaceable sections of composite floor system, designed based on U.S. practices with a 2-hour fire-resistance rating, were tested in this program (see NIST Technical Note 2203 [Choe et al. 2022] for details on the test frame and composite fire test floor). In addition, this experimental program was conducted to generate technical information and data essential for the development and validation of predictive tools for the evaluation of structural performance of buildings in fire.

The authors performed a computational study to develop a validated modeling approach for composite floor systems exposed to fire loading based on the full-scale testing conducted at the NIST NFRL. As reported in previous publications [Main et al. 2017, Jiang et al. 2020b], the modeling approach used in this study was developed to be suitable for coupled thermal-structural analysis. However, in this study, temperatures measured during the composite floor fire test were specified as nodal temperature histories for all components of the composite floor system to model thermal loading resulting from the compartment fire exposure. Therefore, a temperature-dependent structural analysis, rather than a coupled thermal-structural analysis, was performed using the recorded temperature-time histories to validate the computational approach against the displacement and strain data obtained in the composite floor fire test. This approach eliminated the need to conduct a heat transfer analysis and to account for all the uncertainties associated with such analysis, including the significant variability in the thermal properties of SFRM [Zhang et al. 2021], allowing the model validation to focus on the temperature-dependent structural response. The scope of the modeling validation was further limited to rising fire temperatures up to the maximum gas temperature recorded in the NIST NFRL CF2 Test and thus did not include the post-fire cooling phase.

1.2. Report Outline

This report presents the development and validation of a computational modeling approach to evaluate the structural response of steel gravity frames with composite floor systems subjected to fire exposure. The modeled composite floor system consisted of a composite one-way pan joist concrete slab and commercial steel deck (20 gage Vulcraft 3VLI), supporting steel beams and girders, and beam-end and girder-end shear tab connections. Details of the modeling approach including the finite element discretization and material characterizations used to model different components of the composite floor system are described. Note that although the general-purpose finite element software package, LS-DYNA [LSTC 2016] was utilized in the modeling and validation process, the presented methodology can be applied in other finite element software packages with similar features and capabilities.

The report is organized as follows:

- **Chapter 2** presents a brief overview of the test specimen and the test setup used in the Composite Floor Test #2 (CF2 Test) conducted at the NFRL. Details of the design and construction of the two-story steel frame and its composite floor assembly in the CF2 Test along with information on the full-scale fire testing can be found in NIST TN 2165 and NIST TN 2203 [Choe et al. 2021, Choe et al. 2022] reports.
- **Chapter 3** provides details of the computational modeling approach developed to simulate the composite steel frame tested in the CF2 Test. Specifically, the materials modeling, composite shell representation of the floor slab, and numerical solution schemes are discussed.
- **Chapter 4** describes validation of the modeling approach. Within the chapter, representative results and observations from the computational model of composite steel-framed building subjected to the test fire are compared against corresponding ones from the experiment.
- **Chapter 5** discusses simulation results beyond observations from the NIST NFRL CF 2 Test. Specifically presented are stresses in bolts and axial forces in secondary beams predicted from the validated model.
- **Chapter 6** provides a summary of major observations, limitations of the study, and conclusions and recommendations based on the work presented throughout the report.

2. NIST Composite Floor System Tests

Three compartment fire tests were conducted at the NIST NFRL to develop an improved understanding of the response of full-scale composite concrete pan joist slab-steel deck floor systems that are part of a steel-framed building to the standard fire exposure. These tests were different in terms of the reinforcement details for the composite concrete slab, and whether the secondary beams were protected with SFRM. The shear tab beam- and girder-end connections were not test variables in these three tests.

This section provides a brief overview of the Composite Floor Test #2 (CF2 Test). Results and observations from this test were used to validate the modeling approach described in this report. Details of the design and construction of the two-story steel frame and its composite floor assembly in the CF2 Test along with information on the full-scale fire testing can be found in two NIST reports; NIST TN 2165 [Choe et al. 2021] and NIST TN 2203 [Choe et al. 2022].

2.1. NIST NFRL CF2 Test: Overview

A composite steel-framed floor system with plan dimensions of 9.1 m × 6.1 m (30 ft × 20 ft) was tested at the NIST NFRL. The composite floor, subjected to a compartment fire during the test, was a middle bay of a two-story steel gravity frame (two by three bays in plan). A photo of this composite floor following the fire test is shown in Fig. 1. The composite floor assembly was designed to meet the 2-hour fire-resistance rating requirement for steel-framed structures in the U.S. building code [International Code Council 2021] and consisted of a lightweight concrete floor slab on steel deck, W16×31 beams, W18×35 girders, and W12×106 columns. All the beam-to-column, beam-to-girder, and girder-to-column connections in the test bay were shear tab connections.

Fig. 1. The composite-steel-framed floor system tested in the NIST NFRL CF2 Test [Choe et al. 2022]

2.2. Composite Floor System

A 20 gage, 76 mm (3 in) deep profiled steel deck topped with 83 mm (3 1/4 in) of lightweight concrete and reinforced with No. 3 deformed bars spaced at 305 mm (12 in) on center (230 mm^2/m or 0.1 in^2/ft) in orthogonal directions formed the composite floor system. The 83 mm (3 1/4 in.) thickness for the topping concrete was selected to achieve the 2-hour fire resistance rating requirement in the US practice [International Code Council 2021, ANSI/AISC 360 2016]. Details of the composite floor beams are shown in Fig. 2. As seen in Fig. 2, the ribs of the steel deck were oriented perpendicular to the W16×31 beams. As further seen in Fig. 2, composite beam action was achieved using steel headed shear studs, welded to the top flanges of the W16×31 beams, and W18×35 girders. The diameter of the shear studs was 19 mm (3/4 in).

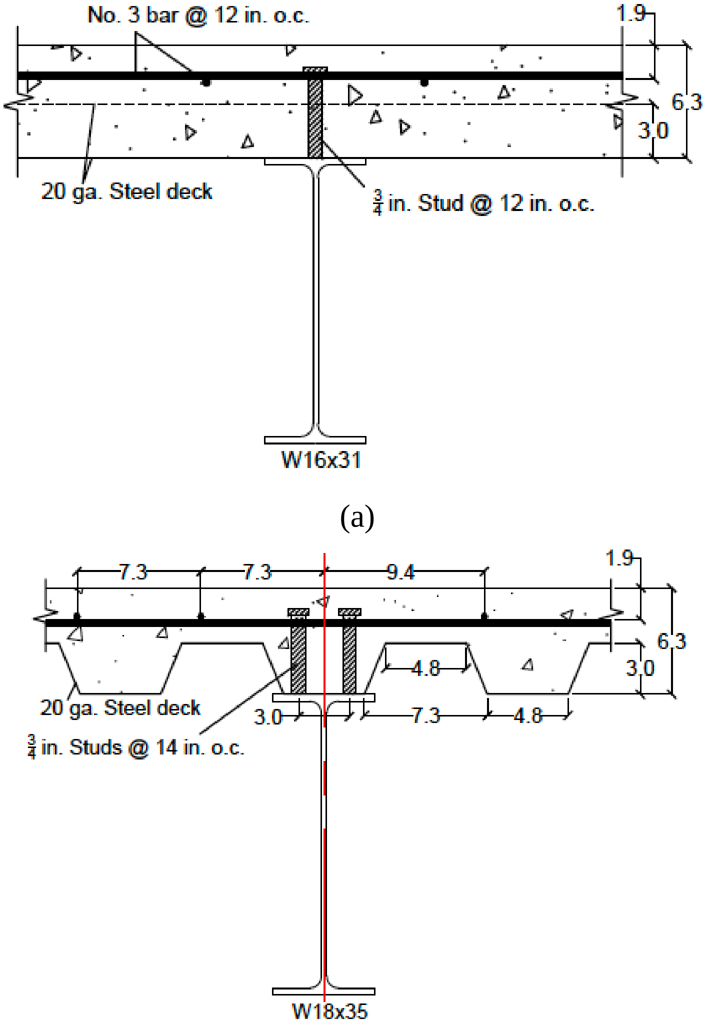

(a)

(b)

Fig. 2. Details of composite floor beams in the test bay of the CF2 Test: (a) composite W16×31 beams; (b) composite W18×35 girders (dimensions are in inches and rounded to the nearest tenth) [Choe et al. 2022].

Three 9.1 m (30 ft) long W16×31 beams and two 6.1 m (20 ft) long W18×35 girders supported the composite floor system in the test bay. The W16×31 beams supporting the composite floor were connected to the columns and girders using standard shear tab connections consisting of a plate, PL 216.0 mm×152.0 mm×9.5 mm (PL 8 1/2 in×6 in×3/8 in), with three 19 mm (3/4 in) diameter structural bolts. W18×35 girders were connected to the webs of W12×106 columns using extended shear tab connections consisting of a plate, PL 229.0 mm×368.0 mm×9.5 mm (PL 9 7/8 in×14 1/2 in×3/8 in), with five 19 mm (3/4 in) diameter structural bolts. Details of the beam-end connections are shown in Fig. 3. Photographs of these connections prior to the application of fireproofing materials can be further seen in Fig. 4.

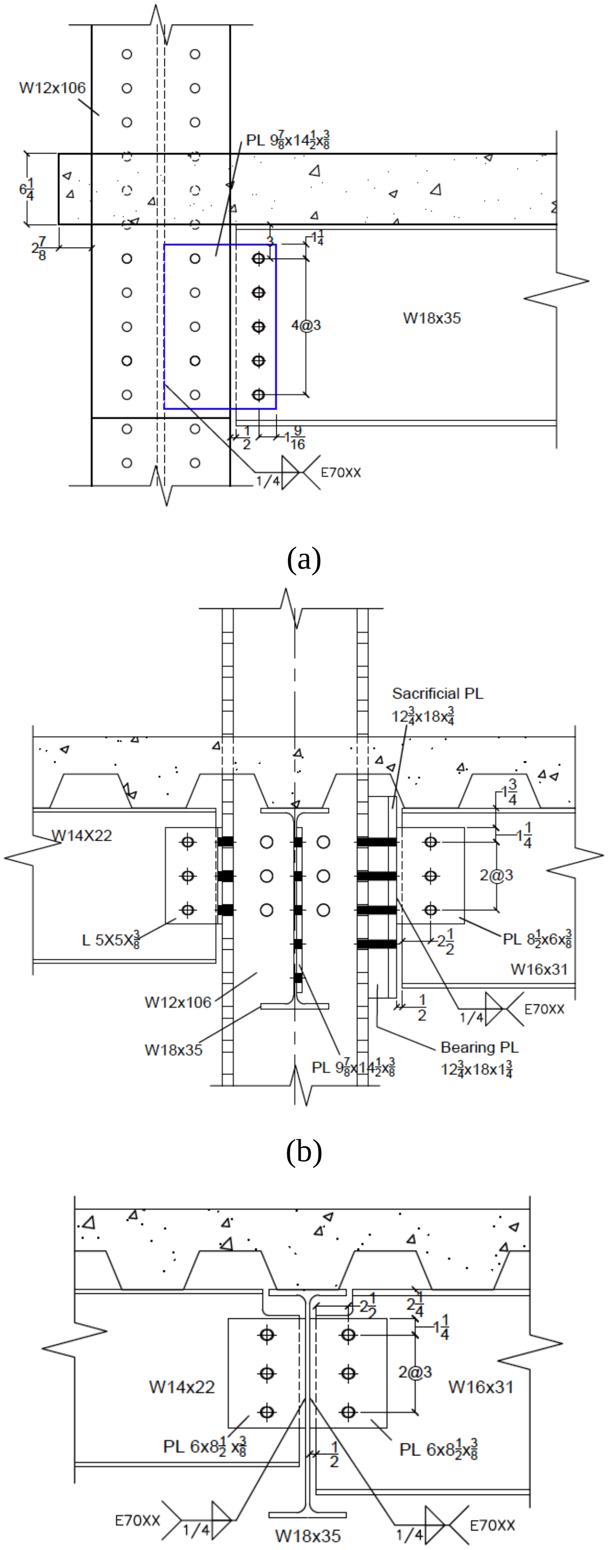

(a)

(b)

(c)

Fig. 3. Connection details in the test bay of the CF2 Test: (a) girder-to-column connection; (b) beam-to-column and girder-to-column connections; (c) beam-to-girder connections (dimensions are in inches) [Choe et al. 2022].

(a) (b)

Fig. 4. Photographs of connections: (a) beam-to-column connections; (b) beam-to-girder connections [Choe et al. 2022].

Details of the composite floor reinforcement, consisting of orthogonal No. 3 rebars, are shown in Fig. 5. In addition to No. 3 rebars, No. 4 rebars were used at the perimeters of the test bay slab (shown as pink dots in Fig. 5(b) and Fig. 5(c)). These No. 4 deformed rebars were 635 mm (25 in.) long and were extended from the perimeter slab splice plates on the three faces of the composite floor slab that were in contact with the surrounding floor of the test frame.

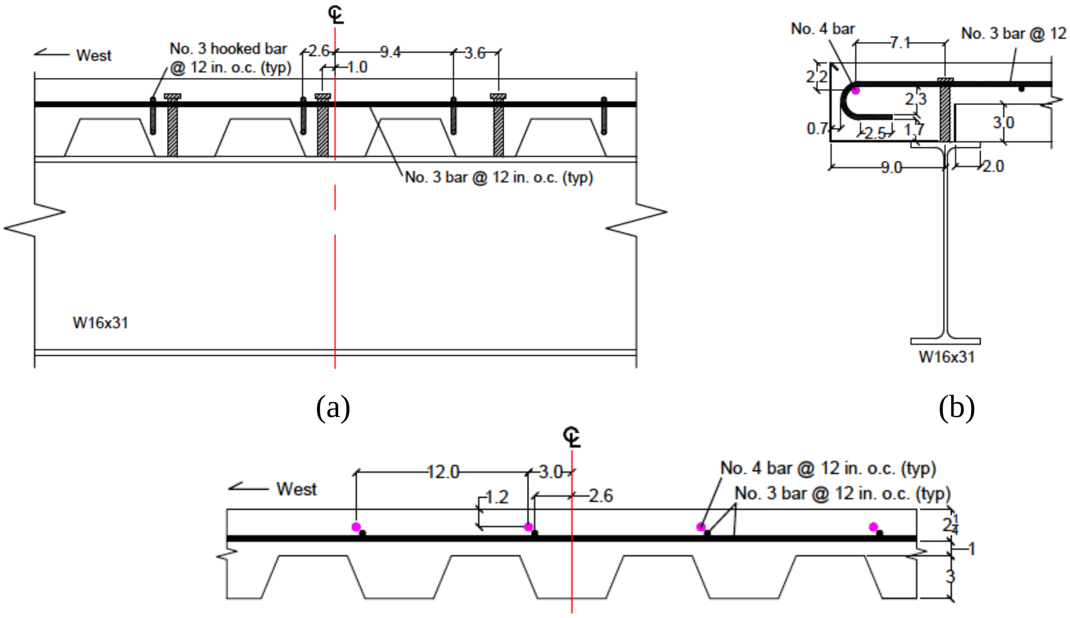

(a) (b)

(c)

Fig. 5. Slab reinforcement in the test bay of the CF2 Test: (a) front view at south end; (b) side view at south end; (c) front view at north end (dimensions are in inches) [Choe et al. 2022].

2.3. Mechanical Properties of Steel Components

The ambient-temperature mechanical properties of steel components of the composite floor system were measured and documented in the test report [Choe et al. 2022]. The fabrication of steel coupons and testing procedures conformed to the ASTM E8/E8M [ASTM International 2022b] standard. Table 1. summarizes the average values of the 0.2 % offset yield strength (F_y), the ultimate tensile strength (F_u), and the percent elongation at fracture (δ_u) for different steel components of the steel frame in CF2 Test. The values after ± symbols indicate the standard deviation calculated from two measured values.

Table 1. Measured mechanical properties of steel components [adapted from Choe et al. 2022].

Steel components	ASTM Designation	F_y [MPa (ksi)]	F_u [MPa (ksi)]	δ_u (%)
W16×31	A992	382 ± 48 (55 ± 7)	502 ± 27 (73 ± 4)	33 ± 5
W18×35	A992	360 ± 20 (52 ± 3)	503 ± 6 (73 ± 1)	33 ± 1
Shear tab plate	A36	290 ± 1 (42 ± 0)	440 ± 30 (64 ± 4)	37 ± 1
Headed stud anchor	A29	408 ± 2 (59 ± 0)	505 ± 3 (73 ± 0)	—
Structural bolt	A325 (F3125)	890 ± 10 (129 ± 1)	965 ± 8 (140 ± 1)	19 ± 1
Steel deck	A653	403 ± 4 (58 ± 0)	473 ± 2 (69 ± 0)	26 ± 1
No. 3 deformed bar	A615	478 ± 1 (69 ± 0)	769 ± 2 (111 ± 0)	22 ± 1

2.4. Mechanical and Thermal Properties of Concrete

The ambient-temperature mechanical and thermal properties of concrete in both the test bay (composite fire test floor) and surrounding bays (concrete slabs adjacent to the composite fire test floor) were also measured and documented in the test report [Choe et al. 2022]. Average values of these concrete properties are provided in Table 2. The values after ± symbols indicate the standard deviation calculated from two measured values.

Table 2. Average properties for hardened concrete [adapted from Choe et al. 2022].

Category	Description	Test bay	Surrounding bays
Structural	Compressive strength, MPa (ksi)	78.0 ± 1.0 (11.3 ± 0.1)	63.0 ± 1.1 (9.1 ± 0.2)
	Splitting tensile strength, MPa (ksi)	6.1 ± 0.2 (0.9 ± 0.0)	3.0 ± 0.3 (0.4 ± 0.0)
	Static modulus, GPa (1000 ksi)	25.3 ± 0.9 (3.7 ± 0.1)	24.9 ± 0.2 (3.6 ± 0.0)
Thermal	Bulk density, kg/m^3 (lb/ft^3)	1948 ± 22 (124 ± 1)	1911 ± 10 (119 ± 1)
	Moisture content, % mass	5.7 ± 0.3	7.7 ± 0.2
	Thermal conductivity, W/m·°K (BTU(IT)/h ft·°F)	2.15 ± 0.31 (1.24 ± 0.18)	2.18 ± 0.14 (1.26 ± 0.08)
	Specific heat, J/kg·°K (BTU(IT)/lb·°F)	797 ± 65 (0.19 ± 0.02)	887 ± 47 (0.21 ± 0.01)

3. Computational Model: Development

The computational model utilized in this study was developed using the general-purpose finite-element software LS-DYNA [LSTC 2016]. The following sections describe the computational modeling approach in detail, including descriptions of the materials characterization, composite shell representation of the floor slab, connections, shear studs, and loading and boundary conditions.

3.1. Material Modeling

Successful modeling of the behavior of composite steel-framed structures in fire depends on material models that accurately capture their behaviors when subjected to elevated-temperatures of fire. This section describes the material models used in the finite element simulation of the composite steel-framed structure subjected to the fire in the CF2 Test.

3.1.1. Structural Steel

The influence of elevated temperatures on the mechanical behavior of structural steel, including its stress-strain behavior, elastic modulus, and yield strength, was considered in the computational model of the composite floor system. The elevated-temperature mechanical models were specifically defined for different structural steels used in wide-flange elements, plate elements, bolts, and shear studs.

The following sections provide details on the material characterization of different structural steels at elevated temperatures and their implementation in LS-DYNA [LSTC 2016]. Within LS-DYNA, material model MAT_106 (MAT_ELASTIC_VISCOPLASTIC_THERMAL) was adopted to describe the families of curves governing the elastic-viscoplastic behavior of structural steels over a large range of temperatures from 20 °C (ambient temperature) to 1200 °C (beyond the maximum temperature expected in the test).

Temperature-dependent mechanical properties (for example, temperature-dependent curves for the yield strength, modulus of elasticity, ultimate tensile strength, and uniform strain) of structural steels (used in wide-flange and plate elements and adopted in MAT_106) were based on previous studies conducted by NIST and followed the approach described by Seif et al. [Seif et al. 2016a and 2016b]. However, the stress-strain relationship for the structural steels proposed by Seif et al. [Seif et al. 2016a and 2016b] was constrained only by the measured ambient-temperature yield strength of the material, with the inelastic behavior defined by an exponential curve with constant coefficients, regardless of whether modeling low- or high-strength steels. The stress-strain curves proposed by Seif et al. [Seif et al. 2016a and 2016b] work well for the low-strength steels, from which the coefficients of the exponential curve were conditioned, but tend to overestimate the uniform strain and ultimate strength of high-strength steels.

The true stress-strain curves used in this study incorporate a significant improvement in the formulation, which allows for user-specified ambient-temperature values of the yield strength, ultimate tensile strength, and uniform strain. Letting σ and ε denote true stress and true strain, respectively, the proposed stress-strain relationship can be expressed as follows.

$$\sigma = \begin{cases} E(T)\varepsilon & \varepsilon < \varepsilon_\mathrm{y}(T) \\ \sigma_\mathrm{y}(T) + \left[(\sigma_\mathrm{u}(T) - \sigma_\mathrm{y}(T)\right]\left[\dfrac{\left[\varepsilon - \varepsilon^*(T)\right]^{n(T)} - \left[\varepsilon_\mathrm{y}(T) - \varepsilon^*(T)\right]^{n(T)}}{\left[\varepsilon_\mathrm{u}(T) - \varepsilon^*(T)\right]^{n(T)} - \left[\varepsilon_\mathrm{y}(T) - \varepsilon^*(T)\right]^{n(T)}}\right] & \varepsilon \geq \varepsilon_\mathrm{y}(T) \end{cases} \tag{1}$$

In Eq. (1), T is the temperature in degree Celsius (°C), $\sigma_\mathrm{y}(T)$ is the true yield stress of steel at temperature T, $\sigma_\mathrm{u}(T)$ is the true ultimate stress of steel at temperature T, $E(T)$ is the elastic modulus of steel at temperature T, $\varepsilon_\mathrm{y}(T)$ is the true yield strain of steel at temperature T, $\varepsilon_\mathrm{u}(T)$ is the true uniform strain of steel at temperature T, $n(T)$ is the shape parameter at temperature T, and $\varepsilon^*(T)$ is the strain offset at temperature T. Letting s and e denote engineering stress and engineering strain, respectively, the true stress values corresponding to the measured yield strength and ultimate strength can be calculated as $\sigma_\mathrm{y} = s_\mathrm{y}(e_\mathrm{y} + 1)$ and $\sigma_\mathrm{u} = s_\mathrm{u}(e_\mathrm{u} + 1)$, respectively, while the true strain values corresponding to the measured yield strain and uniform strain can be calculated as $\varepsilon_\mathrm{y} = \ln(e_\mathrm{y} + 1)$ and $\varepsilon_\mathrm{u} = \ln(e_\mathrm{u} + 1)$, respectively. The shape parameter $n(T)$ and the offset strain $\varepsilon^*(T)$ are determined by imposing the following two conditions on the slope of the stress-strain curve:

$$\left.\frac{\mathrm{d}\sigma}{\mathrm{d}\varepsilon}\right|_{\varepsilon = \varepsilon_\mathrm{y}} = E \quad \text{, and} \quad \left.\frac{\mathrm{d}\sigma}{\mathrm{d}\varepsilon}\right|_{\varepsilon = \varepsilon_\mathrm{u}} = \sigma_\mathrm{u} \tag{2a, b}$$

The first condition, in Eq. (2a), requires the slope of the stress-strain curve to equal the elastic modulus at the yield point, thus ensuring continuity in the slope at the onset of yielding. The second condition, in Eq. (2b), requires the slope of the true stress-strain curve to equal the true stress at the uniform strain, corresponding to the Considère criterion at the onset of necking [Dieter 1976]. Imposing these two conditions for the power-law model in Eq. (1) yields the following relationship between the model parameters:

$$\frac{\sigma_{\mathrm{u}}(T)}{E(T)} = \left(\frac{\varepsilon_{\mathrm{u}}(T) - \varepsilon^{*}(T)}{\varepsilon_{\mathrm{y}}(T) - \varepsilon^{*}(T)}\right)^{n(T)-1} \tag{3}$$

Solving Eq. (3) for the shape parameter $n(T)$ yields the following equation:

$$n(T) = 1 - \frac{\ln E(T) - \ln \sigma_{\mathrm{u}}(T)}{\ln[\varepsilon_{\mathrm{u}}(T) - \varepsilon^{*}(T)] - \ln[\varepsilon_{\mathrm{y}}(T) - \varepsilon^{*}(T)]} \tag{4}$$

Evaluating Eq. (2a) for the power-law model in Eq. (1) and solving for the strain offset $\varepsilon^{*}(T)$ gives the following equation:

$$\varepsilon^{*}(T) = \varepsilon_{\mathrm{y}}(T) - \frac{n(T)[(\sigma_{\mathrm{u}}(T) - \sigma_{\mathrm{y}}(T)]}{E(T)\left[\left(\frac{\varepsilon_{\mathrm{u}}(T) - \varepsilon^{*}(T)}{\varepsilon_{\mathrm{y}}(T) - \varepsilon^{*}(T)}\right)^{n(T)} - 1\right]} \tag{5}$$

Equation (5) is recursive, containing the variable $\varepsilon^{*}(T)$ on both the left and right sides. Thus, in practice, Eqs. (4) and (5) are iterated until the values of $n(T)$ and $\varepsilon^{*}(T)$ stabilize (do not appreciably change between iterations). An initial guess of $\varepsilon^{*}(T) = 0.999\varepsilon_{\mathrm{y}}$ is suggested to start the iteration. In our programmatic implementation of these equations in MATLAB [MathWorks, Inc. 2023], within about 5 to 100 iterations the value of $n(T)$ generally stabilizes to a precision of 1.0×10^{-12} or less.

The elastic modulus $E(T)$ is expressed as a function of temperature as follows [Seif et al. 2016a]:

$$E(T) = E_0 \left[\exp\left(-\frac{1}{2}\left(\frac{\Delta T}{e_3}\right)^{e_1} - \frac{1}{2}\left(\frac{\Delta T}{e_4}\right)^{e_2}\right)\right] \tag{6}$$

where E_0 = 200 GPa (29,000 ksi) is the elastic modulus of structural steel at ambient temperature, ΔT (measured in °C) is the increase in temperature above ambient temperature, and e_1 through e_4 are coefficients that depend on the type of steel. For rolled structural steel, $e_1 = 3.768$, $e_2 = 1.000$, $e_3 = 639$ °C, and $e_4 = 1650$ °C [Seif et al. 2016a]. Fig. 6 shows the degradation of the normalized elastic modulus with increasing temperature using Eq. (6) with the listed coefficients. The temperature-dependence of the yield strength $\sigma_{\mathrm{y}}(T)$ is expressed as [Seif et al. 2016a]:

$$\sigma_{\mathrm{y}}(T) = \sigma_{\mathrm{y0}} \left[r_5 + (1 - r_5) \times \exp\left(-\frac{1}{2}\left(\frac{\Delta T}{r_3}\right)^{r_1} - \frac{1}{2}\left(\frac{\Delta T}{r_4}\right)^{r_2} \right) \right] \tag{7}$$

where σ_{y0} is the yield strength of steel at ambient temperature and r_1 through r_5 are coefficients that depend on the type of steel. For rolled structural steel, $r_1 = 7.514$, $r_2 = 1.000$, $r_3 = 588$ °C, $r_4 = 676$ °C, and $r_5 = 0.090$ [Seif et al. 2016a]. The degradation of the yield strength with increasing temperature is also shown in Fig. 6 using Eq. (7) with the listed coefficients. The dependence of the modulus of elasticity and yield strength on temperature are assumed to be the same whether the material is undergoing heating or cooling.

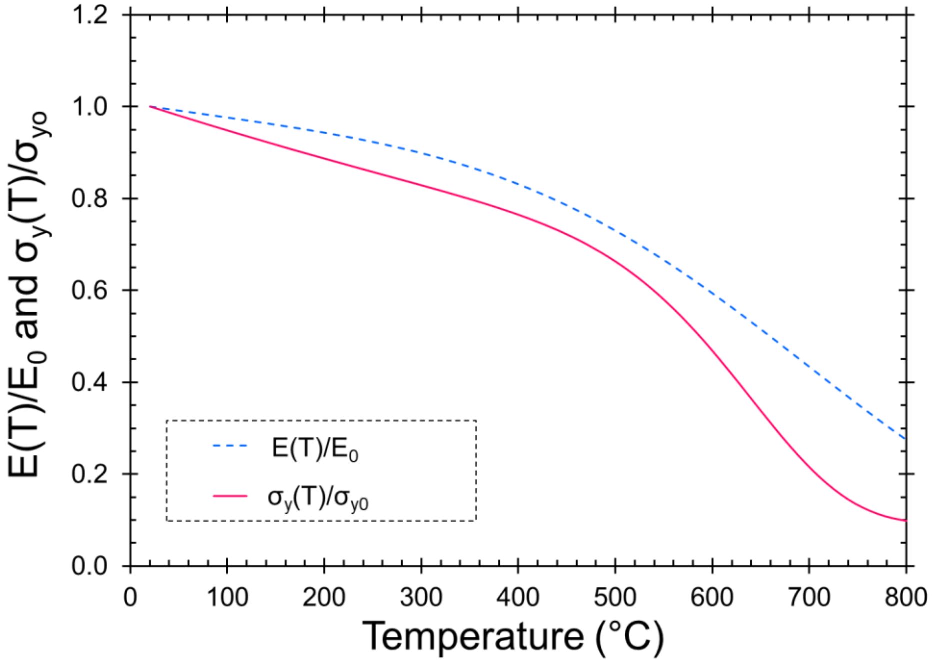

Fig. 6. Degradation of yield strength and elastic modulus with temperature for structural steel [Seif et al. 2016a].

3.1.1.1. ASTM A992 Steel

The wide-flange elements of the composite steel frame were made of ASTM A992 structural steel. Using the material model shown in Eq. (1) and following the procedure outlined in the previous section, the elevated-temperature material behavior of ASTM A992 steel was defined and implemented in the analysis. Stress-strain curves for ASTM A992 steel at temperatures ranging from 20 °C to 1000 °C are shown in Fig. 7. Figures 8, and 9 further depict the temperature-dependent yield strength and modulus of elasticity of ASTM A992 steel, respectively.

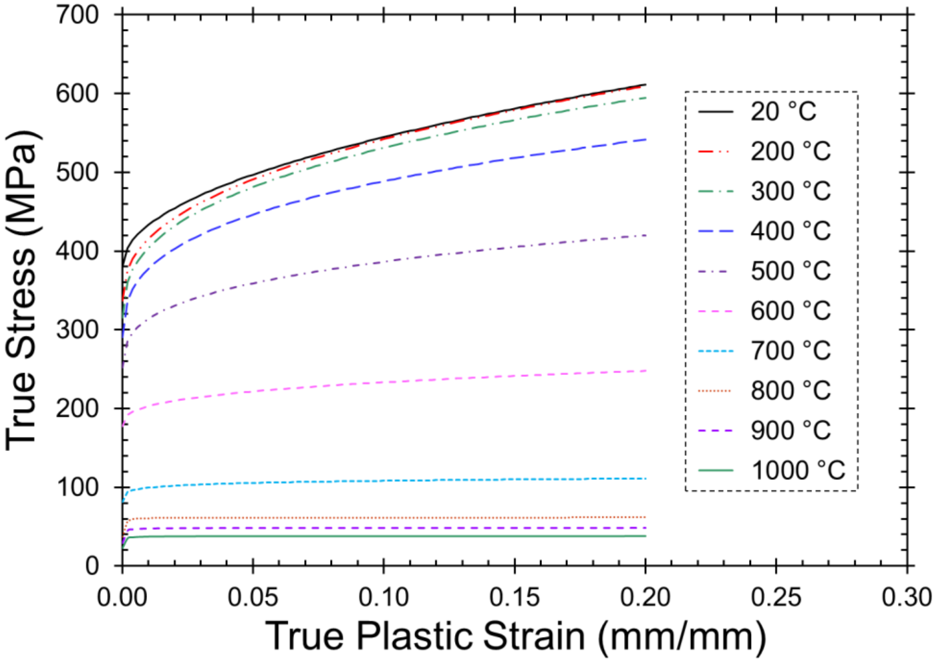

Fig. 7. Stress-strain models for ASTM A992 steel at elevated temperatures.

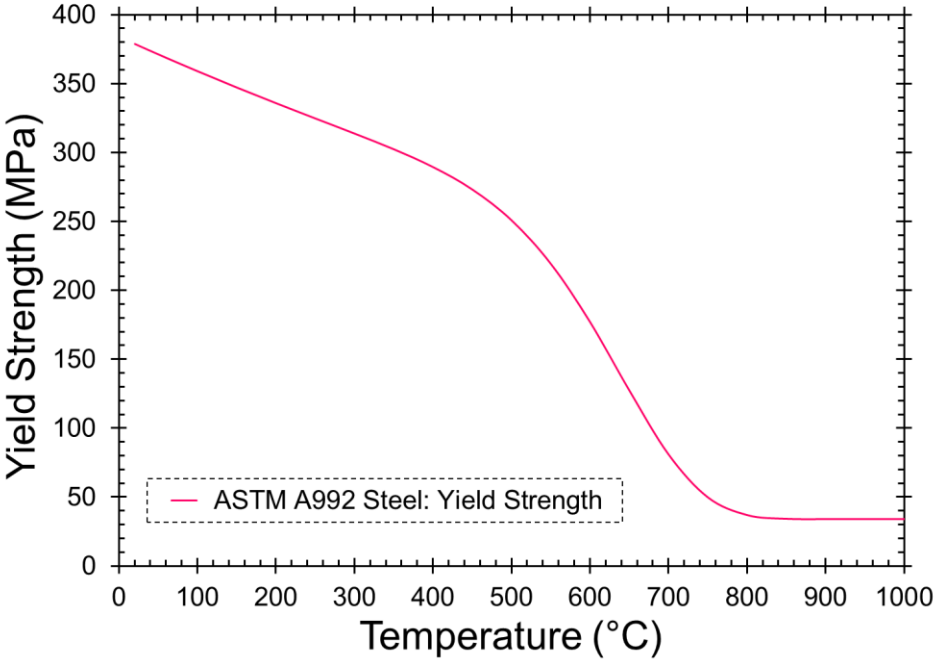

Fig. 8. Yield strength of ASTM A992 steel as a function of temperature.

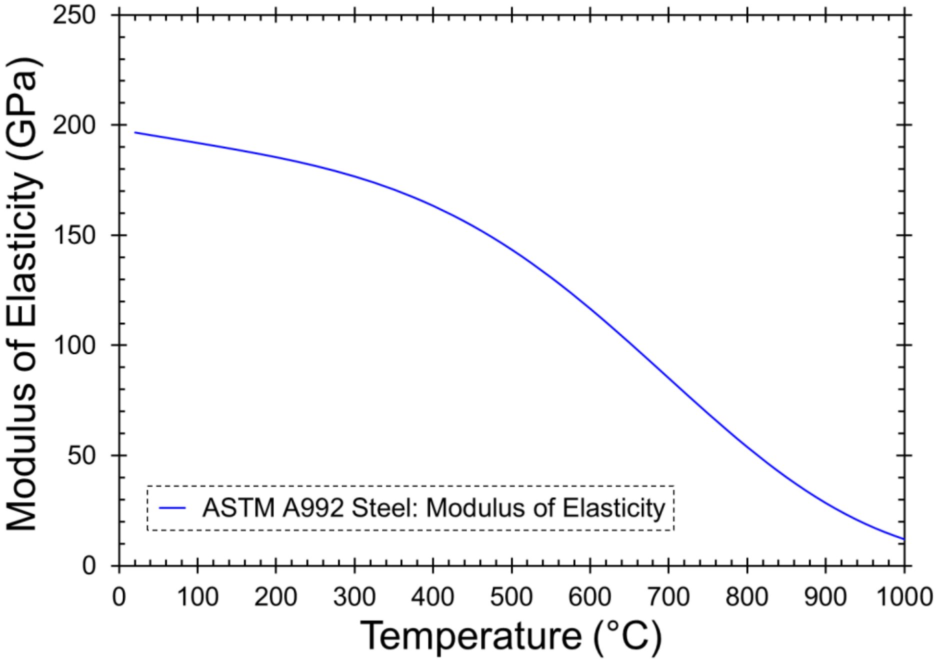

Fig. 9. Elastic modulus of ASTM A992 steel as a function of temperature.

As shown in Figs. 7, 8, and 9, the elevated temperatures lead to nonlinear stress-strain behavior typified by nonlinear (with increasing temperature) reductions in both stiffness and strength. As further seen in Fig. 7, no plastic failure strain was considered in the stress-strain curves for ASTM A992 steel at elevated temperatures, because fracture of the bolted connections was deemed to be the governing failure mode.

3.1.1.2. ASTM A36 Steel

Plate elements for connections including the shear tab plates, column base plates, and rolled angles were made of ASTM A36 steel. The elevated-temperature mechanical behavior of ASTM A36 steel, including stress-strain curves, yield strength and elastic modulus was developed based on the material model shown in Eq. (1) and was included in the computational model using the MAT_106. The material characterization for ASTM A36 steel at elevated temperatures is shown in Figs. 10, 11, and 12.

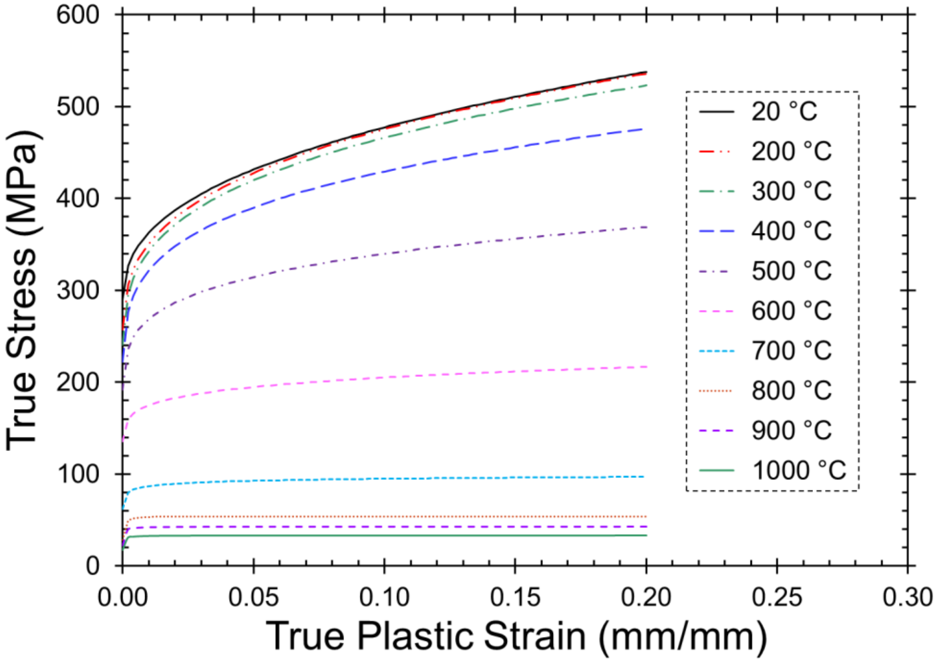

Fig. 10. Stress-strain models for ASTM A36 steel at elevated temperatures.

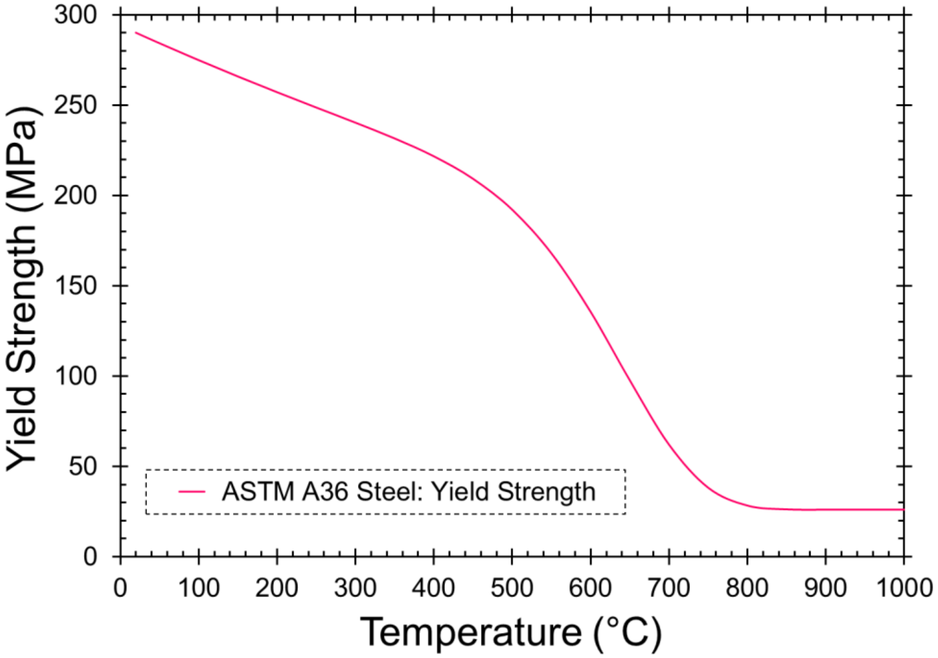

Fig. 11. Yield strength of ASTM A36 steel as a function of temperature.

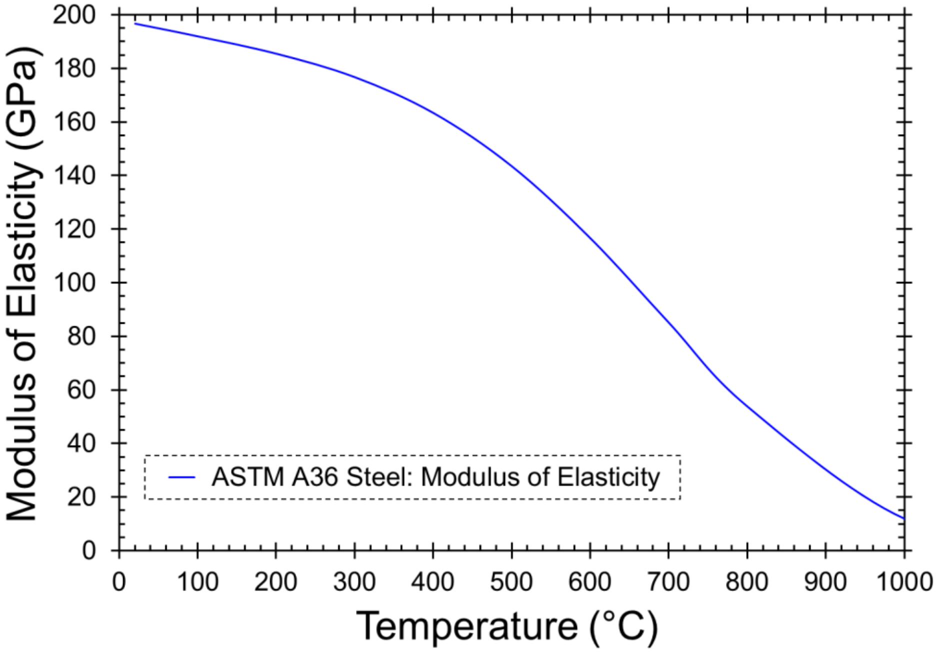

Fig. 12. Elastic modulus of ASTM A36 steel as a function of temperature.

As can be seen in Figs. 10, 11, and 12, similar to ASTM A992 steel, the influence of elevated temperatures on the nonlinear stress-strain behavior, and reductions in both strength and stiffness of ASTM A36 were considered in the computational model of the composite floor system. As further seen in Fig. 10, no plastic failure strain was considered in the stress-strain curves for A36 steel at elevated temperatures.

3.1.1.3. Temperature-Dependent Connection Model

A macro-modeling approach was used for the bolted connections, in which a temperature-dependent load-displacement relationship was defined for each bolt row of the connection, based on a component-based connection model for single plate shear connections at ambient temperatures developed previously by Weigand 2017. By capturing the behaviors of the individual components of the bolted connection, such as the bolt, shear plate, and beam web, and the interactions between those components (e.g., bearing of the bolt on the plate holes), component-based connection models can provide an effective means for modeling the behavior of steel bolted connections under fire loads. In component-based connection models, the connection is notionally discretized into characteristic-width segments with aggregate force-displacement behaviors represented by discrete connection springs (Fig. 13 (a)). For single plate shear connections, each characteristic-width segment contains contributions from a shear-plate segment, bolt shaft, and beam-web segment which are modeled as individual component springs in series, as shown in Figs. 13 (b) and 13 (c).

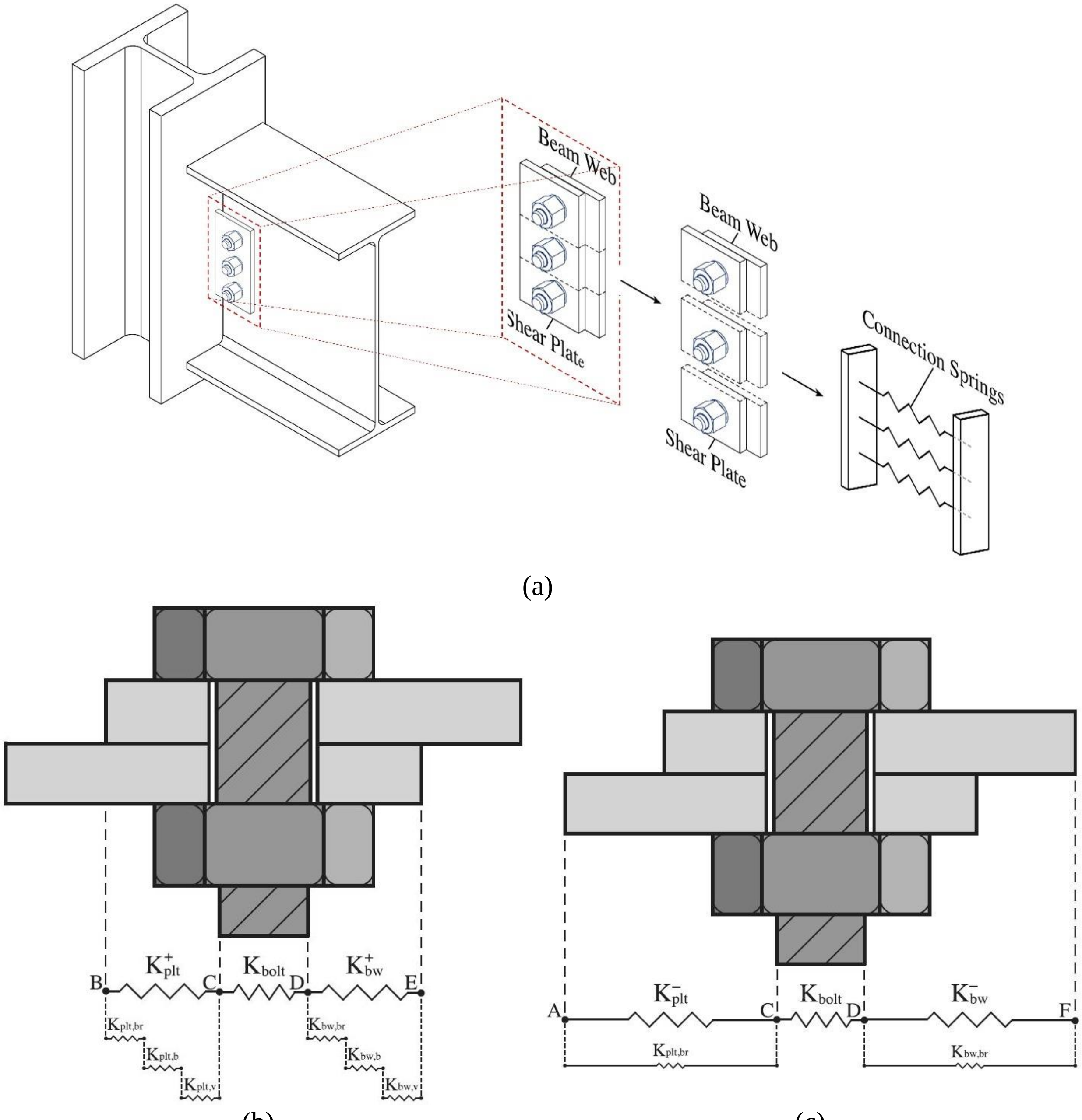

(a)

(b)

(c)

Fig. 13. (a) Discretization of single-plate shear connection into connection springs, (b) connection spring stiffness contributions in tension, and (c) connection spring stiffness contributions in compression [Weigand 2017]

The component-based model, developed by Weigand 2017 and shown in Fig. 13, was extended to include the effects of elevated temperatures on the connection response. The temperature-dependence was included by incorporating temperature-dependent mechanical properties for plate and bolt steels directly into the equations describing the connection response. In this section, the model formulation is outlined and the responses and interactions between connection components are presented. Note that the component-based model presented in this report for single-plate shear connections at elevated temperatures was validated in previous work [Seif et al. 2018] against experimental and numerical studies by Yu 2009 and by Weigand et al. 2018.

The formulation of the component-based model for the connection behavior in this report makes use of temperature-dependent equations for the mechanical properties of both structural steel and structural bolts developed by Luecke et al., and presented in Seif et al. [Seif et al. 2016a, Seif et al. 2016b]. Specifically, the elastic modulus E, which is the same for bolts as for structural steel, is calculated from Eq. (5). For A325 and A490 high-strength bolts (now governed by a new combined ASTM F3125 Standard [ASTM International 2022d]), the temperature-dependence of the yield strength σ_y is calculated from Eq. (6), with $r_1 = 4.967$, $r_2 = 1.000$, $r_3 = 456$ °C, $r_4 = 2040$ °C, and $r_5 = 0.000$ [Seif et al. 2016a]. Compared to structural steel, bolts retain a high percentage of their σ_y value with the increase of temperature until about 400 °C, after which the yield strength of bolts reduces dramatically relative to that of structural steel. Fig. 14 shows the degradation of the yield strength with increasing temperature for structural steel (like ASTM A36 and ASTM A992), and ASTM A325 and A490 bolts. Note that at 400 °C, both rolled steel and bolts retain about 75 % of their yield capacity. At 600 °C, structural steel retains slightly less than 50 % of its yield capacity, while bolts retain less than 20 % of their yield capacity.

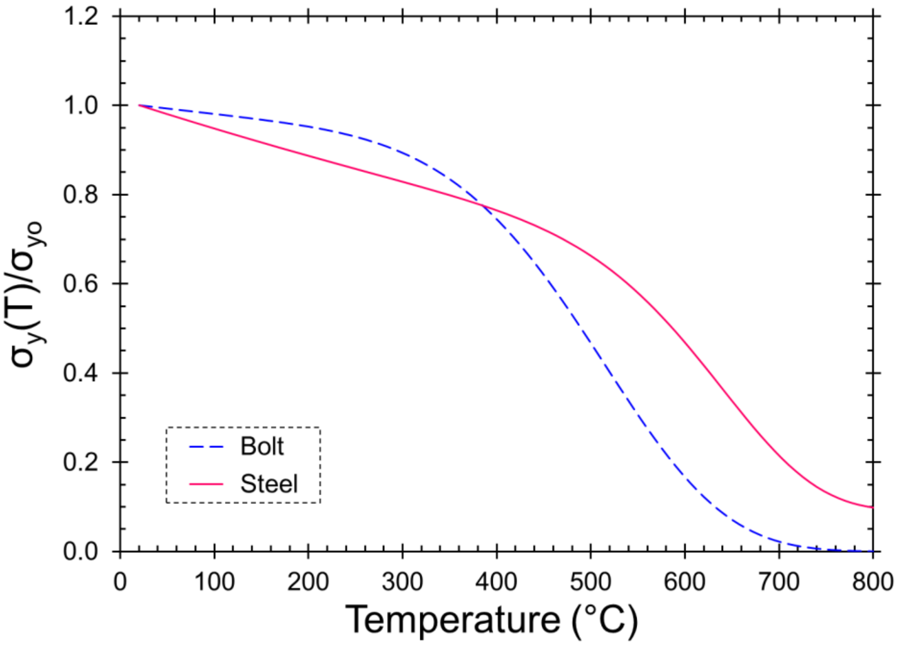

Fig. 14. Degradation of yield strength versus the increase in temperature for rolled structural steel and high-strength bolt [Seif et al. 2016a].

The shear force-deformation behavior of the bolt, including shear and flexural effects, is modeled using:

$$R_{\mathrm{bolt}} = R_{\mathrm{unl}} + \frac{(K_{\mathrm{i,bolt}}(T) - K_{\mathrm{p,bolt}}(T))(\Delta_{\mathrm{bolt}} - \Delta_{\mathrm{unl}})}{\left(1 + \left|\frac{(K_{\mathrm{i,bolt}}(T) - K_{\mathrm{p,bolt}}(T))(\Delta_{\mathrm{bolt}} - \Delta_{\mathrm{unl}})}{R_{\mathrm{cyc,bolt}}(T)}\right|^{n_{\mathrm{bolt}}}\right)^{(1/n_{\mathrm{bolt}})}} + K_{\mathrm{p,bolt}}(T)(\Delta_{\mathrm{bolt}} - \Delta_{\mathrm{unl}}) \qquad (8)$$

Where Δ_{bolt} is the bolt shear deformation, R_{bolt} is the bolt shear force, T denotes the dependence of the stiffness or capacity parameter on temperature, (Δ_{unl}, R_{unl}) are the coordinates of the last unload point, $n_{\mathrm{bolt}} = 2$ is the shape parameter defining sharpness of the transition between the elastic and plastic behaviors, and $R_{\mathrm{cyc,bolt}} = sign\,(\Delta - \Delta_{\mathrm{unl}})R_{\mathrm{v,bolt}}(T) - R_{\mathrm{unl}} + K_{\mathrm{p,bolt}}(T)\Delta_{\mathrm{unl}}$ is the cyclic reference load for the bolt shear force-deformation behavior where $R_{\mathrm{v,bolt}}(T) = 0.62A_{\mathrm{bolt}}F_{\mathrm{u,bolt}}(T)$ is the shear capacity of the bolt at elevated temperatures. Figure 15 plots a representative backbone force-displacement response of the bolt component spring at elevated temperatures using Eq. (8). Load-displacement curves shown in Fig. 15 were constructed for ASTM A325 bolts with 19 mm (3/4 in) diameter and for the geometry of shear tab connections in the NIST NFRL CF2 Test (as described in Section 2.2).

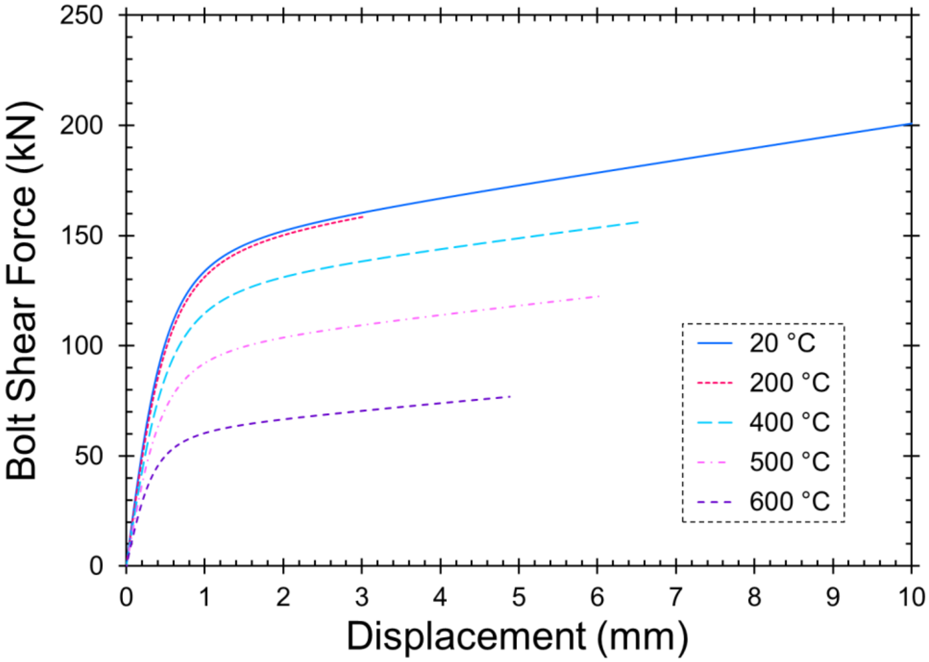

Fig. 15. Backbone shear force-displacement curves for the bolt component spring at elevated temperatures – ASTM A325 bolt [ASTM International 2022d] with 19 mm (3/4 in) diameter.

The shear-plate and beam-web component springs (i.e., plate springs) are modeled using a piecewise version of the Richard Equation (see Richard and Abbott 1975) such that,

$$
\mathrm{R}(\Delta)=\begin{cases}
\dfrac{\left(K_{\mathrm{b}}^{-}(T)-K_{\mathrm{p}}^{-}(T)\right)(\Delta-\Delta_{\mathrm{br}}^{-})}{\left(1+\left|\dfrac{\left(K_{\mathrm{b}}^{-}(T)-K_{\mathrm{p}}^{-}(T)\right)(\Delta-\Delta_{\mathrm{br}}^{-})}{R_{\mathrm{b}}^{-}(T)}\right|^{n_{\mathrm{b}}^{-}}\right)^{\left(1/\mathrm{n}_{\mathrm{b}}^{-}\right)}}+K_{\mathrm{p}}^{-}(T)(\Delta-\Delta_{\mathrm{br}}^{-}), & \Delta\le\Delta_{\mathrm{slipctr}}-\frac{1}{2}\Delta_{\mathrm{slip}}\\[2ex]
\dfrac{\left(K_{\mathrm{i}}(T)-K_{\mathrm{y}}(T)\right)\Delta}{\left(1+\left|\dfrac{\left(K_{\mathrm{i}}(T)-K_{\mathrm{y}}(T)\right)\Delta}{R_{\mathrm{y}}(T)}\right|^{n}\right)^{\left(1/\mathrm{n}\right)}}+K_{\mathrm{y}}(T)\Delta, & \Delta_{\mathrm{slipctr}}-\frac{1}{2}\Delta_{\mathrm{slip}}\le\Delta\le\Delta_{\mathrm{slipctr}}+\frac{1}{2}\Delta_{\mathrm{slip}}\\[2ex]
\dfrac{(K_{\mathrm{b}}^{+}-K_{\mathrm{p}}^{+})(\Delta-\Delta_{\mathrm{br}}^{+})}{\left(1+\left|\dfrac{\left(K_{\mathrm{b}}^{+}(T)-K_{\mathrm{p}}^{+}(T)\right)\left(\Delta-\Delta_{\mathrm{br}}^{+}\right)}{R_{\mathrm{b}}^{+}(T)}\right|^{n_{\mathrm{b}}^{+}}\right)^{\left(1/\mathrm{n}_{\mathrm{b}}^{+}\right)}}+K_{\mathrm{p}}^{+}(T)\left(\Delta-\Delta_{\mathrm{br}}^{+}\right), & \Delta\ge\Delta_{\mathrm{slipctr}}+\frac{1}{2}\Delta_{\mathrm{slip}}
\end{cases}
\qquad (9)
$$

the superscripts, $(\cdot)^{+}$·and $(\cdot)^{-}$, denote tensile and compressive deformations of the component spring, respectively. The remaining parameters in Eq. (9) are defined in Fig. 16, in which a schematic of the ambient-temperature backbone response for the shear-plate and beam-web component springs is depicted. The equations for parameters in Eq. (9) are further developed and described in detail below to define the behavior of the backbone response curve at elevated temperatures.

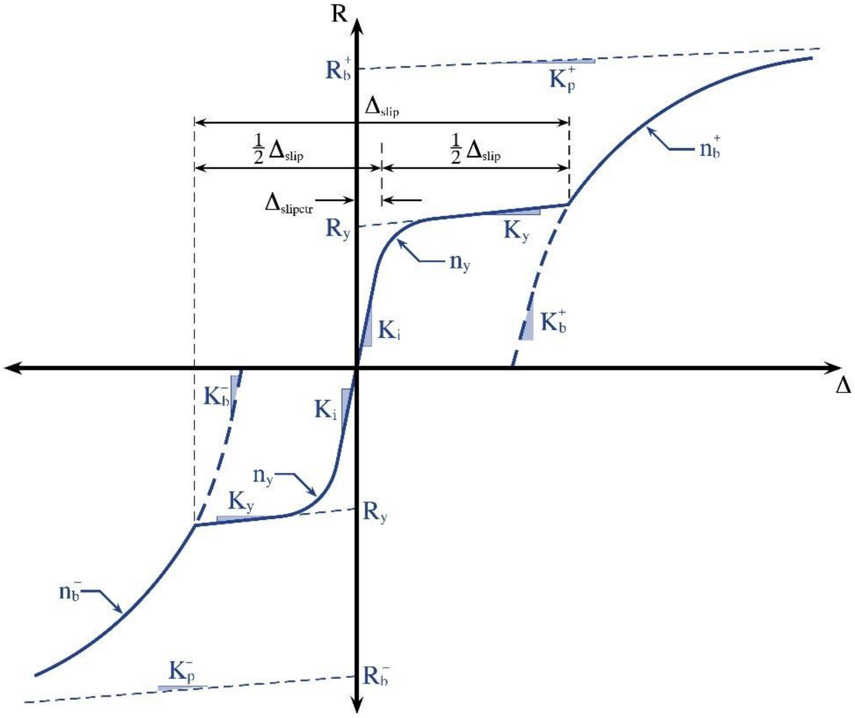

Fig. 16. Backbone force-displacement curve for the shear-plate and beam-web component spring behavior [Weigand 2017].

The capacity and stiffness parameters of bearing behavior of the bolt on the plate and beam web edge distances (i.e., the plate component spring bearing response in tension) at ambient temperature were adapted from the work of [Rex and Easterling 2003], who performed tests of a single bolt bearing against a single-plate with edge distances, plate thicknesses, bolt diameters, plate widths, and edge conditions that were varied between the tests. The elastic and plastic stiffnesses of the bearing force-deformation response can be determined from $K_b^+ = \beta_s \overline{K}_b \alpha_{K_b}$ and $K_p^+ = \beta_s \overline{K}_b \alpha_{K_p}$, where $\beta_s = 1$ for structural steel, $\alpha_{K_b} = 1.731$, and $\alpha_{K_p} = -0.009$ (see Rex and Easterling 2003), and

$$\overline{K}_{\mathrm{b}}(T) = \frac{1}{\frac{1}{\overline{K}_{\mathrm{b}}^{\mathrm{br}}(T)}+\frac{1}{\overline{K}_{\mathrm{b}}^{\mathrm{b}}(T)}+\frac{1}{\overline{K}_{\mathrm{b}}^{\mathrm{v}}(T)}} \tag{10}$$

with elastic stiffness contributions resulting from direct bearing $\overline{K}_{\mathrm{b}}^{\mathrm{br}}(T) = 120 t_{\mathrm{p}} F_{\mathrm{y}}(T) d_{\mathrm{b}}^{(4/5)}$, bending $\overline{K}_{\mathrm{b}}^{\mathrm{b}}(\mathrm{T}) = 32E(T) t_{\mathrm{p}}\left(L_{\mathrm{ehp}} - d_{\mathrm{b}}/2\right)^{3}$, and shearing $\overline{K}_{\mathrm{b}}^{\mathrm{v}}(T) = (20/3)G(T) t_{\mathrm{p}}\left(L_{\mathrm{ehp}} - d_{\mathrm{b}}/2\right)$. In the equations for the stiffness contributions, t_{p} is the plate thickness, $d_{\mathrm{b}}$is the bolt diameter, $F_{\mathrm{y}}(T)$is the temperature-dependent yield strength of the plate material defined in Eq. (7), $E(T)$ is he temperature-dependent modulus of elasticity of the plate material defined in Eq. (6), $G(T) = E(T)/\left(2(1+\nu)\right)$ is the temperature-dependent shear modulus of the plate material, and ν is the Poisson's ratio.

The bearing response of the plates in compression is more constrained than that in tension, due to the additional restraint against bending provided by the plate welds. This additional constraint leads to a marginally stiffer force-deformation response in compression, relative to that in tension, an effect has been noted experimentally for single-plate shear connections at ambient temperatures under increasing magnitude reversed cyclic loading [Crocker and Chambers 2004]. The component spring bearing force-deformation response in compression mirrors the response in tension, but with initial elastic and plastic bearing stiffnesses based only on the direct bearing stiffness such that $K_{\mathrm{b}}^{-}(T) = \beta_{\mathrm{s}} \overline{K}_{\mathrm{b}}^{\mathrm{br}}(T) \alpha_{\mathrm{K_b}}$ and $K_{\mathrm{p}}^{-}(T) = \beta_{\mathrm{s}} \overline{K}_{\mathrm{b}}^{\mathrm{br}}(T) \alpha_{\mathrm{K_p}}$. In compression, $\alpha_{\mathrm{K_p}} = 0.001$ was taken as a small positive value to avoid the potential for a negative tangent stiffness.

Using Eq. (9) and following the above discussions, representative force-displacement curves for the shear-plate and beam-web component springs at elevated temperatures are plotted in Figs. 17 and 18, respectively. The force-displacement curves shown in Figs. 17 and 18 were constructed for the ASTM A36 [ASTM International 2019] shear-plate and the ASTM A992 [ASTM International 2022a] beam-web based on the geometry of shear tab connections in the NIST NFRL CF2 Test (as described in Section 2.2).

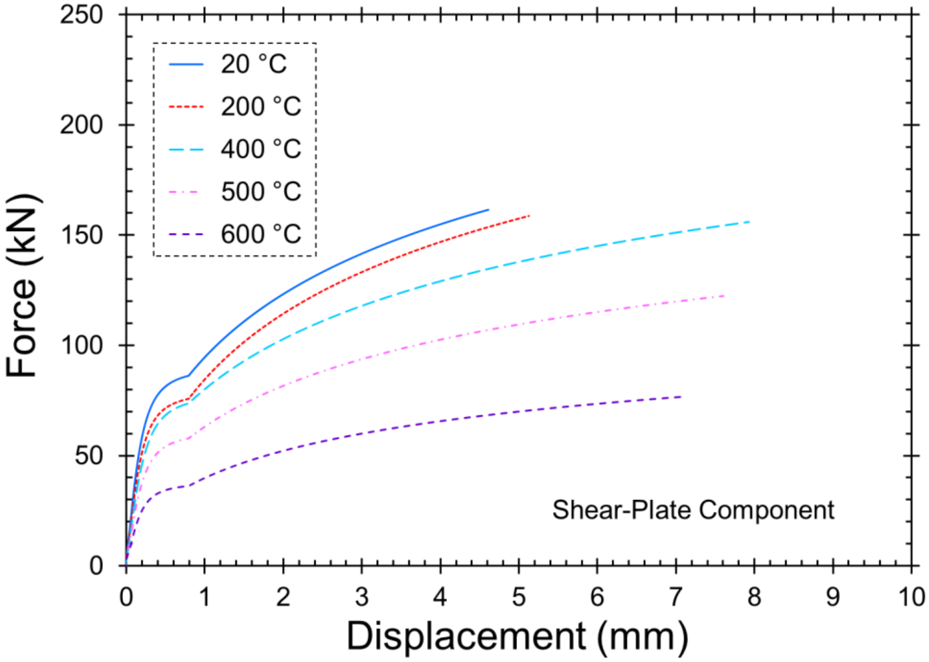

Fig. 17. Force-displacement curves for the shear-plate component spring at elevated temperatures – ASTM A36 [ASTM International 2019] plate.

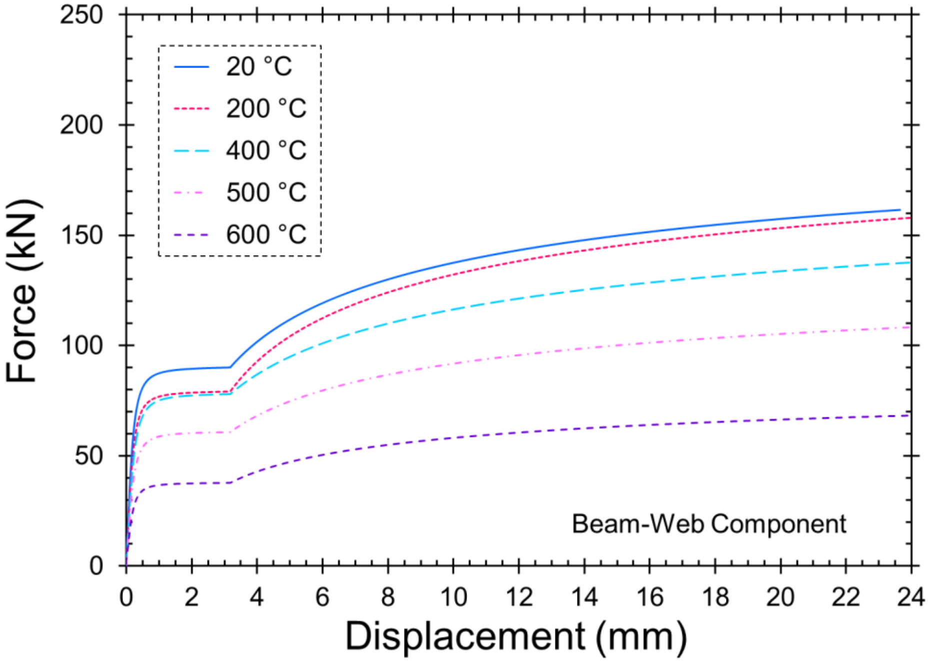

Fig. 18. Force-displacement curves for the beam-web component spring at elevated temperatures – ASTM A992 [ASTM International 2022a] steel.

Figure 19 shows the resultant load-displacement relationships for the connection component spring at various temperatures obtained by integrating the force-deformation relationships for the various connection components using the preceding methodology. As described in Section 3.2.2, these load-displacement relationships were implemented in the model of the composite floor system by representing each bolt row in a connection using a single solid element, with stress-strain relationships obtained by scaling the target load-displacement relationship based on the element dimensions. The resulting stress-strain curves, along with temperature-dependent retention factors for strength and stiffness, were implemented using MAT_106 (*MAT_ELASTIC_VISCOPLASTIC_THERMAL) in LS-DYNA. Connection failure was modeled using element erosion, in which the solid elements representing each bolt row of the connection were deleted from the model at a specified plastic strain, corresponding to a resultant displacement of approximately 24 mm (0.95 in), based on measured failure displacements from ambient-temperature connection testing by Weigand 2014.

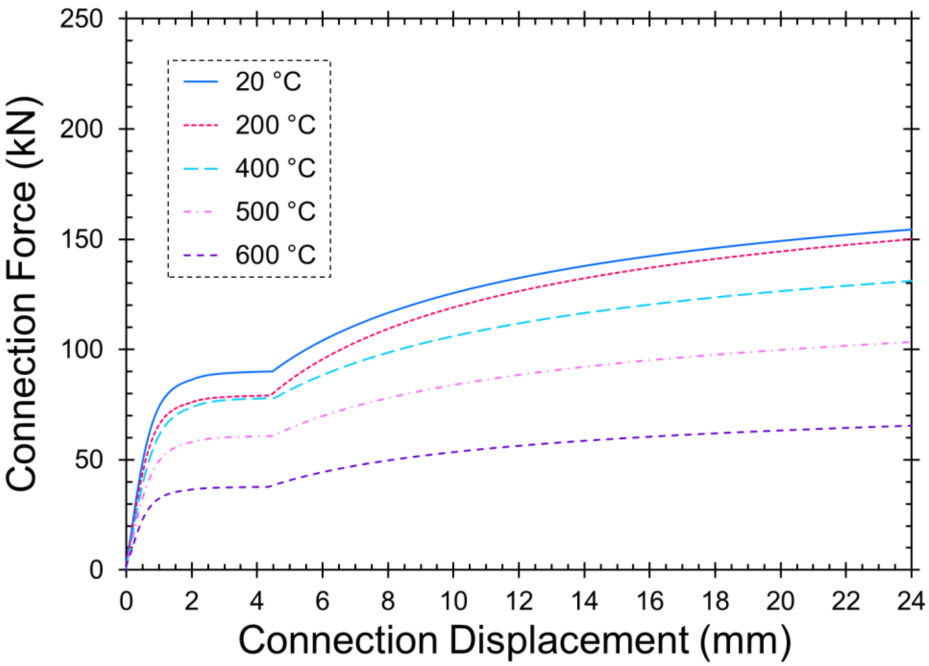

Fig. 19. Force-displacement curves for the connection component spring at elevated temperatures.

3.1.1.4. Shear Studs

Similar to the bolted single-plate shear connections, a reduced-order modeling approach was used for the shear studs, in which each shear stud was represented using a temperature-dependent load-displacement relationship intended to capture the resultant shear force versus slip behavior of a shear stud embedded in a composite concrete floor slab. A load-slip relationship for shear studs at ambient temperature was modified for elevated-temperature conditions based on reported tests in the literature [Ollgaard et al. 1971]. The ambient-temperature load-slip relationship was based partly on an empirical model proposed by Ollgaard et al. 1971 based on results from pushout testing of shear studs without steel deck. This empirical model is presented in Eq. (6), in which the relationship between load (Q) and slip (Δ) is established.

$$\frac{Q}{Q_\mathrm{u}} = \left(1 - e^{-0.71\Delta}\right)^{0.4} \tag{11}$$

In Eq. (11), Q_u represents the ultimate shear strength of the shear stud calculated based on the AISC Specification [ANSI/AISC 360 2016]. Actual rather than nominal strength of shear stud material was used in the model based on results from Dara [Dara 2015]. The relationship corresponding to Eq. (11) is shown as a dashed line in Fig. 20. Based on comparisons of experimental measurements from ambient-temperature testing of a composite beam [Ramesh et al. 2019] with model calculations using various load-slip relationships for the shear studs, the load-slip relationship shown as a solid line in Fig. 20 was found to provide reasonably good agreement with the experimental results (as depicted in Fig. 21). This ambient-temperature relationship, which was adopted in this study, follows Eq. (11) up to a maximum shear strength of $Q_\mathrm{max} = 0.85Q_\mathrm{u}$ with the shear force remaining constant at this maximum value until a slip of 3 mm is reached, at which point the shear force drops linearly to zero at a slip of 5 mm.

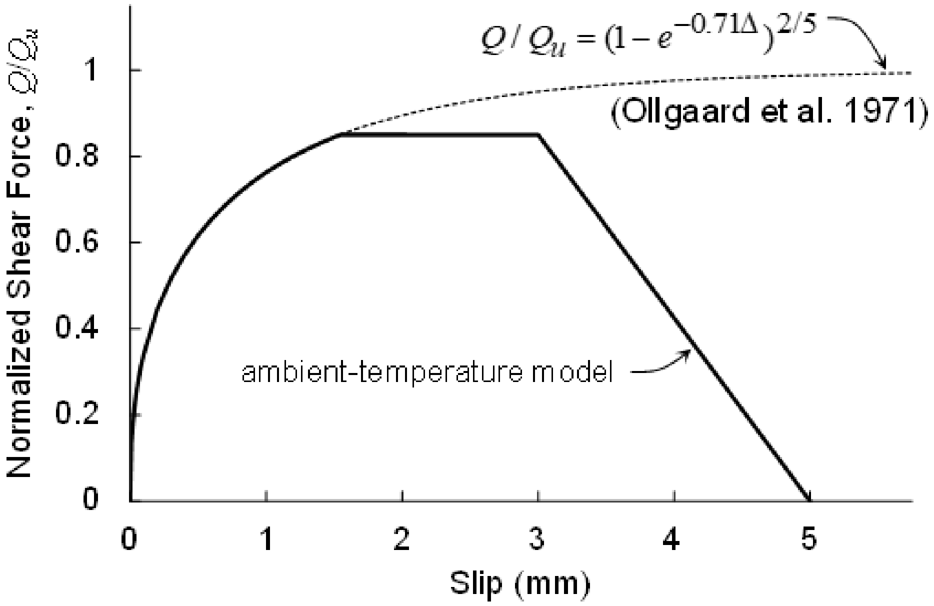

Fig. 20. Load-slip model for shear studs at ambient temperature.

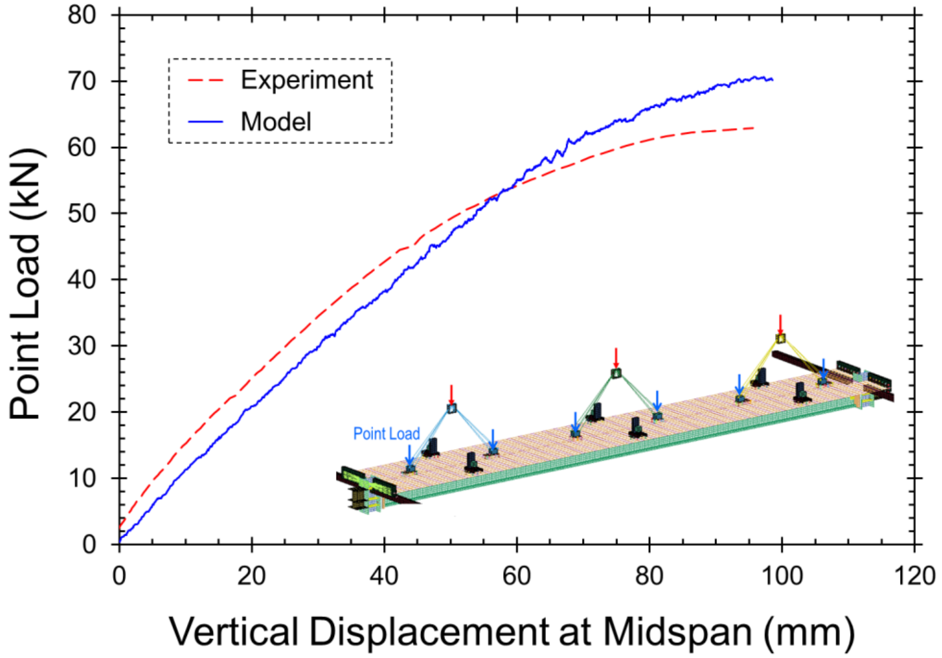

Fig. 21. Predictions of load-deflection curves for a composite beam tested at ambient temperature [Ramesh et al. 2019] using the load-slip relationship for shear studs shown as a solid line in Fig. 20.

The temperature-dependent load-slip curves for the shear studs were then developed by scaling the ambient-temperature load values at each temperature level using the reduction factors for yield strength of structural bolts from Weigand et al. 2018. Reduction factors for yield strength of bolts were used to reduce Q_u at high temperatures based on observations from experiments that shear stud failures under elevated temperatures occurred at the steel shank of the stud [Zhao and Kruppa 1997, Dara 2015]. The slip levels at peak load and at failure were modeled as temperature-independent based on evidence from experiments where no significant dependence of slip at failure on temperature was observed [Dara 2015]. The resulting load-slip curves for shear studs at elevated temperatures are presented in Fig. 22.

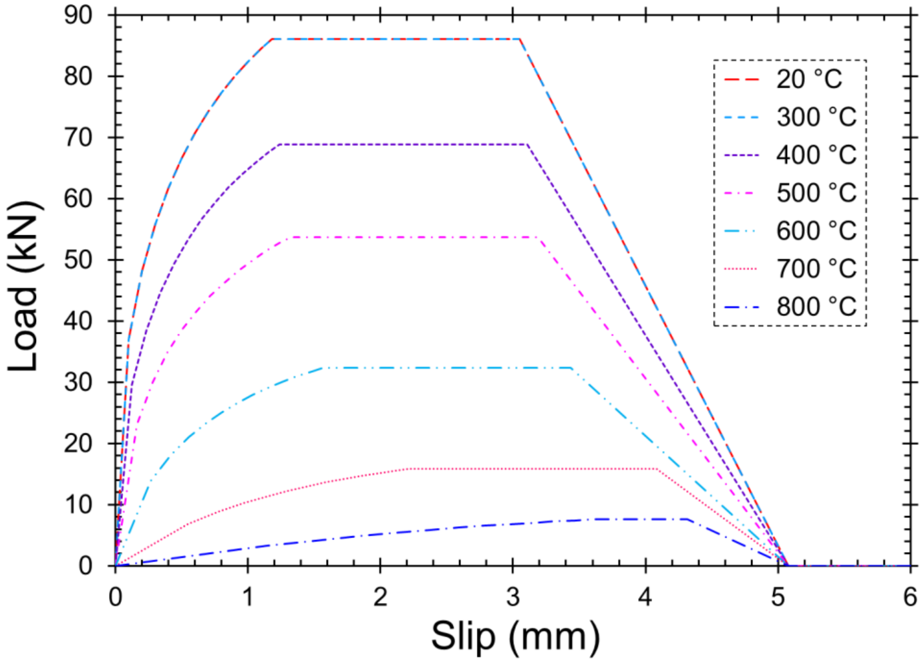

Fig. 22. Load-slip models for shear stud at elevated temperatures.

As described in Section 3.2.3, the load-displacement relationships in Fig. 22 were implemented in the model of the composite floor system by representing each shear stud using a single solid element, with stress-strain relationships obtained by scaling the target load-displacement relationships based on the element dimensions. The resulting stress-strain curves, along with temperature-dependent retention factors for strength and stiffness were implemented using MAT_106 in LS-DYNA (*MAT_ELASTIC_VISCOPLASTIC_THERMAL). Shear stud failure was modeled using element erosion, in which the solid elements representing each shear stud were deleted from the model at a specified plastic strain, corresponding to a resultant displacement of approximately 5 mm, at which the shear resistance reaches zero.

3.1.2. Composite Slab

The *MAT_CONCRETE_EC2 (MAT_172) feature in LS-DYNA was adopted to capture the material behavior of concrete in the composite slab at elevated temperatures. The stress-strain curves in this material model for concrete and reinforcing bars at ambient and elevated temperatures are based on the Eurocode 2 (EC2) [CEN EN 1992-1-2 2004]. These curves for concrete and steel reinforcement at ambient temperature are shown in Fig. 23. They are scaled to the user-defined compressive strength and tensile strength of concrete, and elastic modulus and yield strength of reinforcement. The temperature dependence of the stress-strain relation is by default taken from EC2 [CEN EN 1992-1-2 2004]. A constant value of 8 millionths per degree Celsius (8×10^{-6}/ °C) was used for the coefficient of thermal expansion of concrete at ambient and elevated temperatures.

The material model MAT_172 was specifically used to model concrete, steel decking, and embedded steel reinforcement. Using the MAT_172 model, the crushing of concrete in compression and cracking of concrete in tension were specifically considered. Spalling of concrete at elevated temperatures was not considered in this model. For modeling plain concrete only, a reinforcement ratio of zero was used (Fraction of reinforcement, FRACR = 0), while for metal decking only, a reinforcement ratio of unity was implemented (FRACR = 1). A reinforcement ratio between zero and unity was used for modeling reinforced concrete with evenly distributed reinforcement (0 < FRACR < 1).

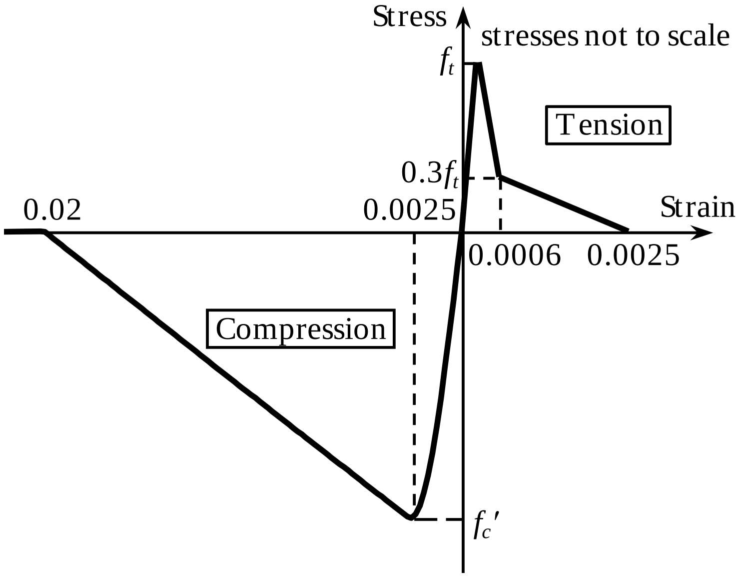

(a) Concrete

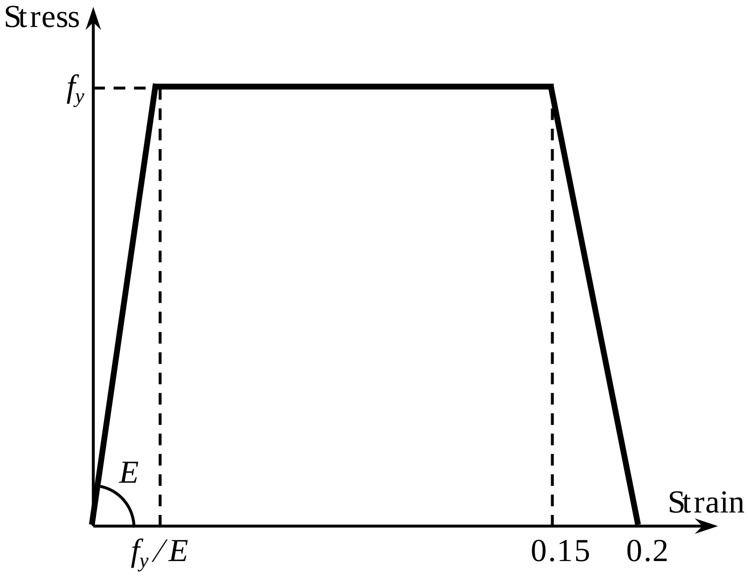

(b) Steel

Fig. 23. Stress-strain representation of the composite slab at ambient temperature: (a) concrete; (b) steel [Jiang et al. 2020b].

3.2. Geometry Modeling

Elements of the composite steel-framed floor system in the NIST NFRL Test #2 were explicitly modeled in LS-DYNA. Figure 24 shows an image capture of the overall view of the model developed in LS-DYNA. Figures 25 to 28 further depict an overview of different connections modeled in the finite element model. This section provides details for modeling the geometry of the composite floor system.

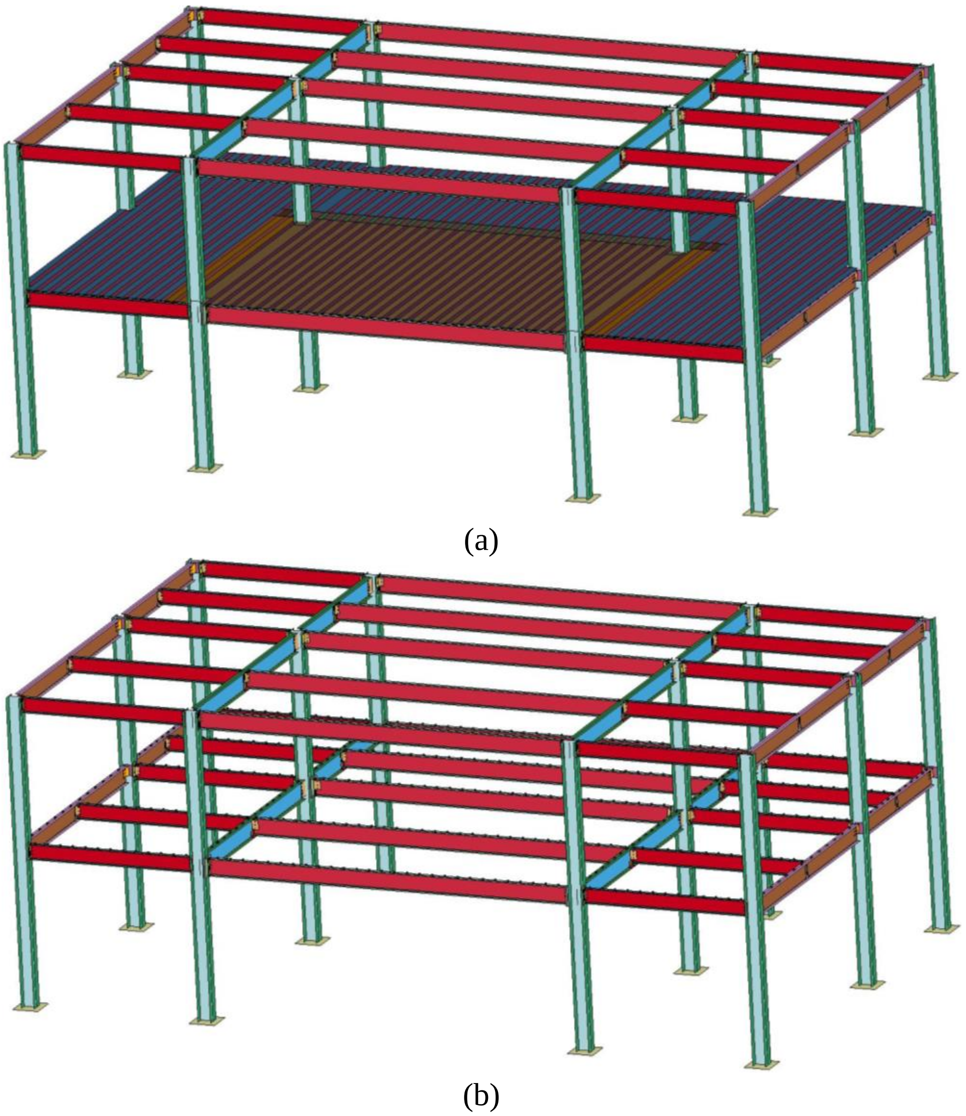

Fig. 24. Finite element model of the composite steel-framed floor system tested in the NIST NFRL CF2 Test: (a) steel frame and composite slab; (b) steel frame.

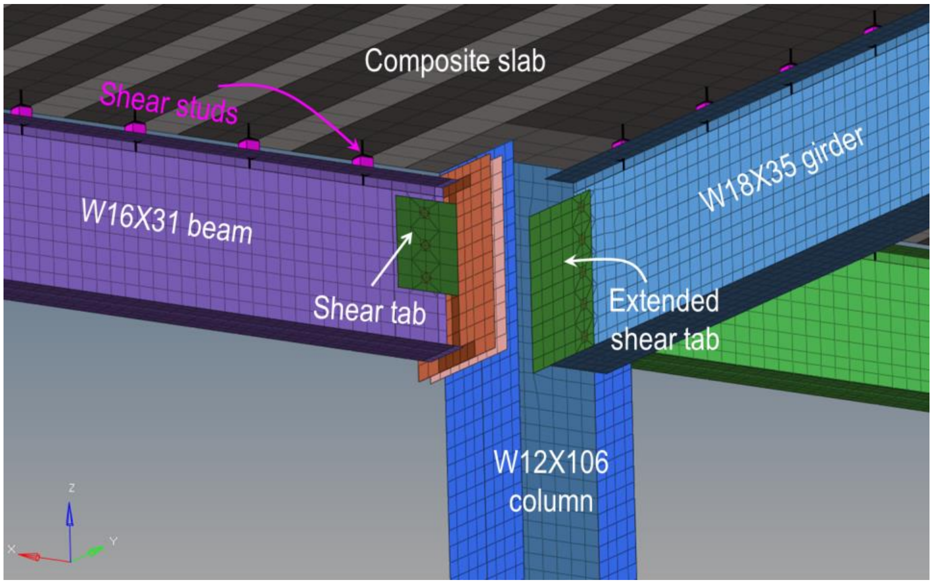

Fig. 25. Finite element model of beam-to-column and girder-to-column connections for the structural members in the test bay.

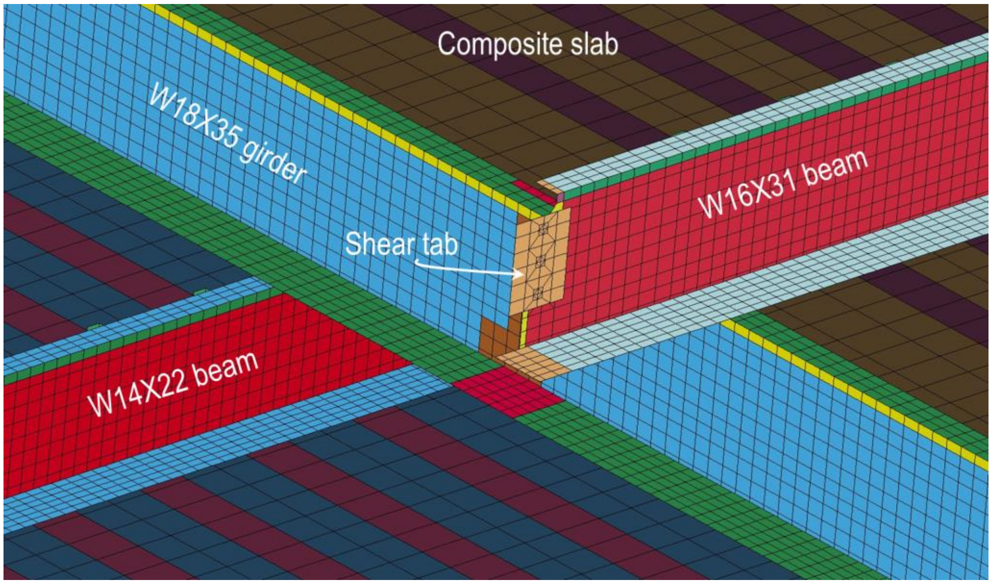

Fig. 26. Finite element model of beam-to-girder connections in the test bay.

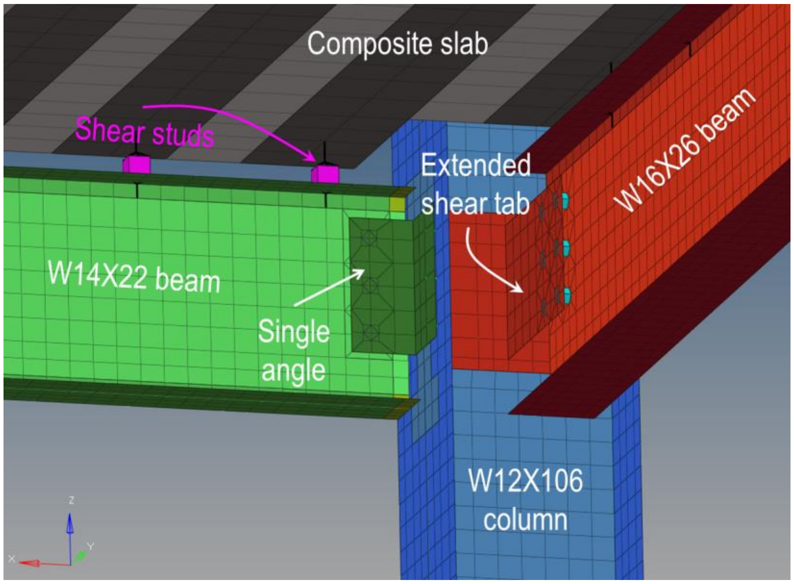

Fig. 27. Finite element model of beam-to-column and girder-to-column connections for the structural members outside the test bay.

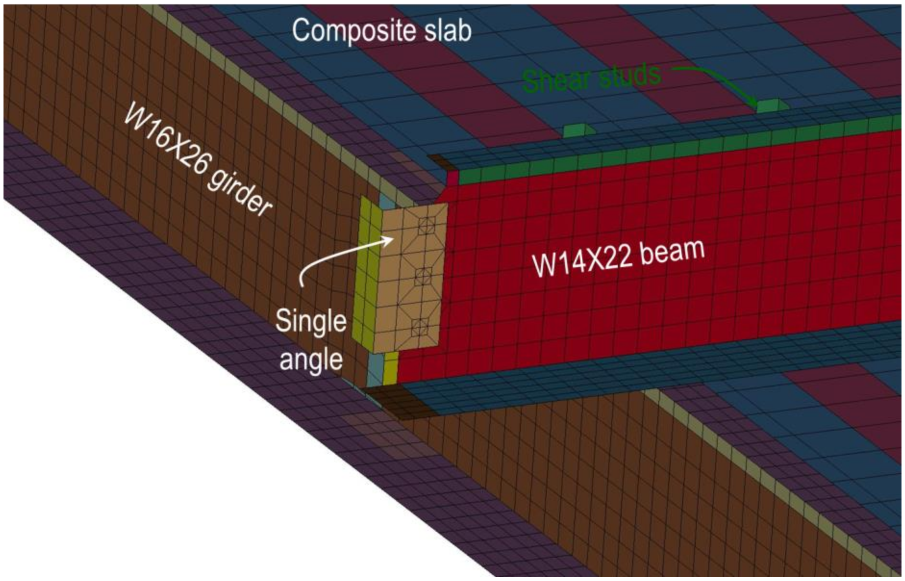

Fig. 28. Finite element model of beam-to-girder connections outside the test bay.

3.2.1. Steel Components

Belytschko-Tsay four-node shell elements [LSTC 2016] were utilized to discretize the steel plates, angles, beams, girders, and columns. These shell elements were defined using the

*ELEMENT_SHELL feature in LS-DYNA. The *SECTION_SHELL feature was further used to define section properties for the shell elements including shell element formulation, integration rule, cross-sectional properties, and shell thickness. The thickness-enhanced shell formulation, based on the Reissner-Mindlin kinematic assumption with a 2 × 2 integration in the shell element plane [LSTC 2016], was utilized in defining section properties. This shell element formulation was defined using EQ. 26 (Fully integrated shell with thickness stretch) of the variable ELFORM [LSTC 2016]. Additionally, using variable NIP (Number of Integration Points), shell elements with five through thickness integration points were assumed. Gaussian integration was adopted as a through thickness numerical integration rule for shell elements. Further, variables T1, T2, T3, and T4 were used to assign nodal thicknesses for the shell element. Moreover, parts were defined using the *PART feature to combine material, section, and thermal properties of steel members. A unique part was assigned to each steel plated element. Therefore, wide-flange sections of beams, girders, and columns were defined with three parts representing flanges, web, and k-areas.

3.2.2. Bolted Connections

A macro-modeling approach was used for the bolted connections, in which a single solid element was used to represent the axial load-displacement behavior of each bolt row in a connection (see Fig. 29). The target load-displacement relationship for each bolt row, presented previously in Section 3.1.1.3, was converted to a stress-strain relationship based on the dimensions of the solid elements used for the macro-modeling. Specifically, the engineering stress of the solid elements was calculated as the load multiplied by √3 and divided by the element cross sectional area. The engineering strain was calculated as the slip divided by the element width (in the direction normal to the beam web) multiplied by √3. The √3 multiplier accounts for the conversion from axial to shear stresses based on the von Mises criterion. Each solid element shared nodes with the shell elements representing the beam web on one side and the shear plate on the other side so that the shear deformations of the solid element correspond to the relative displacement of those components. This modeling approach provided the same load-deformation behavior for displacements in any direction in the plane of the beam web, thus accommodating a combination of shear, axial, and flexural deformations.

Eight-node hexahedral solid elements were defined using the *ELEMENT_SOLID feature in LS-DYNA. The *SECTION_SOLID feature was further used to define section properties for the solid elements including solid element formulation. The solid element formulation was defined using EQ. -2 of the variable ELFORM [LSTC 2016]. More specifically, fully integrated solid elements with accurate formulation and suitable for elements with poor aspect ratio were adopted. Further, parts were defined using the *PART feature to combine material, section, and thermal properties for bolts.

Bolts in shear tab connections (beam-to-column, beam-to-girder, and girder-to-column connections) were represented by a single solid element (eight-node hexahedral solid element) with an in-plane dimension of 18 mm and out-of-plane dimension of 14 mm. Figure 29 shows an example of modeling bolts in a single plate shear connection between W16×31 beams and W12×106 columns.

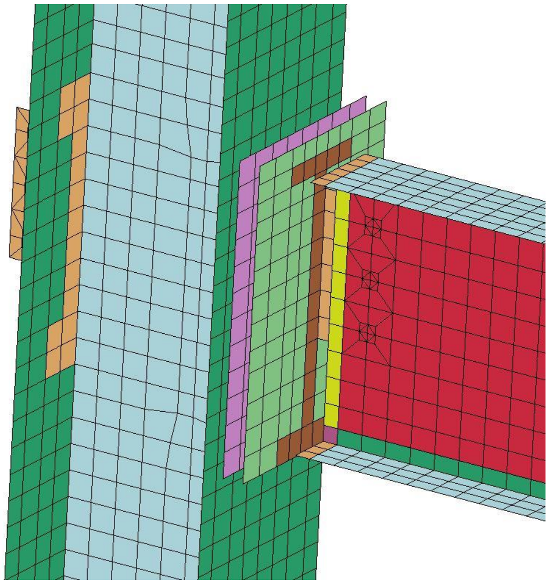

(a) W16×31 beam-to-column connections

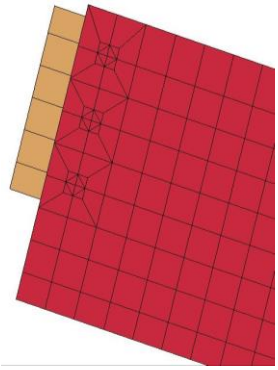

(b) Bolts between web and shear plates

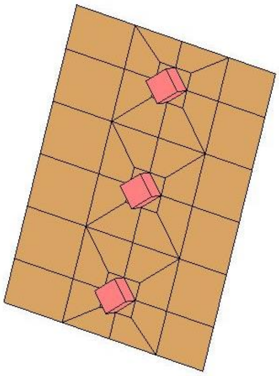

(c) Bolts and shear plate

Fig. 29. Modeling bolt geometry in shear tab connections in the simulation of composite floor test.

Bolts in connections between end plates and the column flanges were not explicitly modeled; they were specified by rigid-body constraints defined using the *CONSTRAINED_NODAL_RIGID_BODY feature in LS-DYNA. Figure 30 shows a representative of modeling column bolts as rigid elements in the simulation of the composite floor test. The connection detail from the test is also added in Fig. 30 for reference.

(a) (b)

Fig. 30. Modeling column bolts as rigid-body constraints in the simulation of composite floor test.

3.2.3. Shear Studs

Similar to the bolted connections, a macro-modeling approach was used for the shear studs, in which a single solid element (eight-node hexahedral solid element) was used to represent the resultant shear load-displacement behavior of each shear stud. The target shear load-displacement relationship, presented previously in Section 3.1.1.4, was converted to a stress-strain relationship based on the dimensions of the solid elements used to represent the shear studs. Specifically, the engineering stress of the solid elements was calculated as the load multiplied by √3 and divided by the element cross sectional area. The engineering strain was calculated as the slip divided by the element height multiplied by √3. The √3 multiplier accounts for the conversion from axial to shear stresses based on the von Mises criterion. This modeling approach provided the same load-slip behavior for shear displacements in any direction in the plane of the slab. Shear stud failure was modeled using element erosion, in which the solid elements representing shear studs were deleted from the model at a strain corresponding to the failure displacement, where the target load-displacement curve reaches zero load (see Fig. 22). Eight-node hexahedral solid elements were defined using the *ELEMENT_SOLID feature in LS-DYNA. The *SECTION_SOLID feature was further used to define section properties for the solid elements including solid element formulation. The solid element formulation was defined using EQ. -2 of the variable ELFORM [LSTC 2016]. More specifically, fully integrated S/R solid elements with accurate formulation and suitable for elements with poor aspect ratio were adopted. Further, parts were defined using the *PART feature to combine material, section, and thermal properties for shear studs.

Each shear stud was represented as a cube with a length of 34.5 mm (1.36 in) located on the top of the top flange of the primary and secondary beams as shown in Fig. 31. Rigid-body constraints were used to tie the top and bottom nodes of the solid elements representing the shear studs to the respective nodes on the composite slab and the beam’s top flange, respectively. Figure 32 depicts the assignment of rigid body constraints to the top and bottom of shear studs. Rigid-body constraints were defined using the *CONSTRAINED_NODAL_RIGID_BODY feature in LS-DYNA.

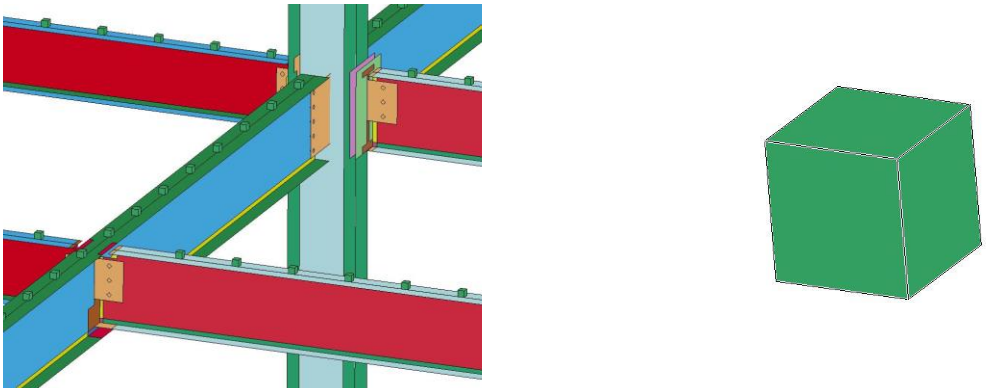
(a) Overall view (b) Close view

Fig. 31. Modeling the geometry of shear studs in the analysis of composite floor test.

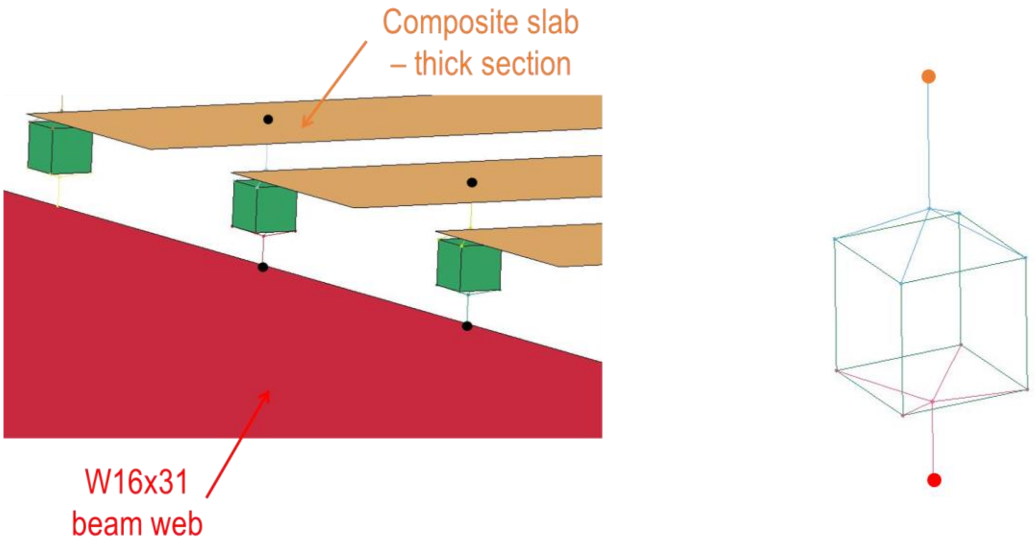

(a) Overall view (b) Close view

Fig. 32. Modeling rigid body constraints for shear studs in the analysis of composite floor test.

3.2.4. Composite Slab

The composite slab was modeled in LS-DYNA adopting the reduced-order approach previously developed and validated by NIST researchers [Jiang et al. 2017]. In this approach, the composite slab (the concrete slab, steel reinforcement, and profiled steel decking) was modeled using alternating strips of shell elements representing the thick and thin portions of the composite slab. Using the *PART_COMPOSITE feature in LS-DYNA, a four-node layered composite shell formulation with distinct structural material, thermal material, and thickness was specified for each layer. Distinct layers were specified for the steel decking and the welded wire mesh reinforcement, with multiple layers representing concrete specified through the thickness of the slab.

For the simple half-slab configuration in Fig. 33, two shell elements were required: Shell A for the thick part of the slab and Shell B for the thin part. The layers have a constant width, and each layer represents an integration point.

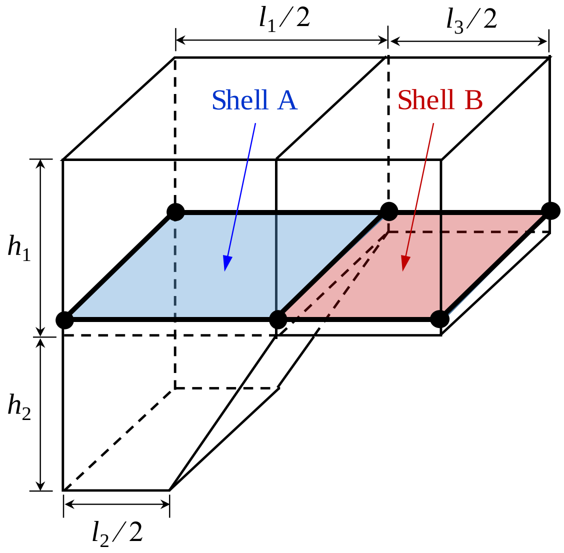

Fig. 33. Schematic representation of the reduced-order model of composite slabs [Jiang et al. 2017].

Due to the inherent characteristics of shell elements, the reduced-order model of the composite slab mandated several modifications to allow it to accurately simulate the thermal and structural behavior of composite slabs. The first limitation was related to the inability of the reduced-order model (shown in Fig. 33) to explicitly account for the web of the steel decking: For structural modeling, the contribution of the web to the bending capacity of the slab could not be directly considered in the shell element. As a result, the thickness of the lower flange (bottom steel layer in shell A) and upper flange (bottom steel layer in shell B) was increased, as shown in Fig. 34. Thus, the lower half of the web was transferred to the lower flange (total thickness is t_1) and the upper half to the upper flange (total thickness is t_2). The initial thickness of the decking layer is t_0. Note also that the original thickness of the lower flange needs to be reduced by the ratio l_2/l_1 to account for the fact that the width of the element l_1 is larger than the width of the lower flange l_2.

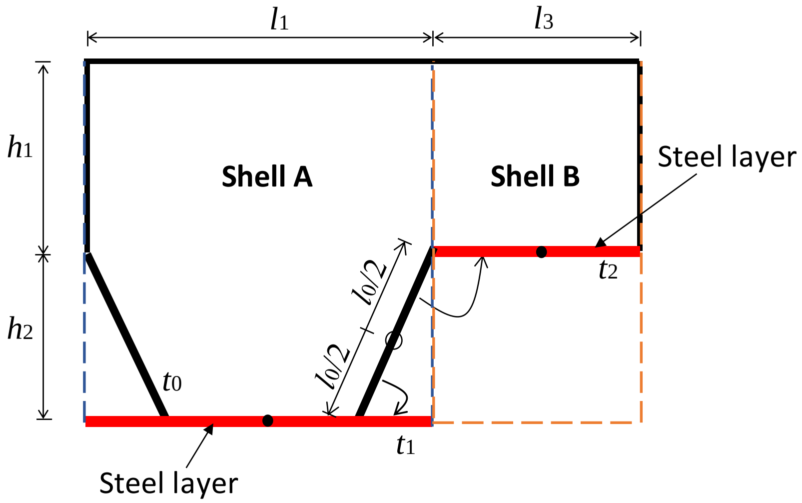

$$t_1 = t_0 \cdot \frac{l_0/2}{l_1} + t_0 \qquad t_2 = t_0 \cdot \frac{l_0/2}{l_3} + t_0$$

Fig. 34. Consideration of the contribution of web in the reduced-order model [Jiang et al. 2017].

The second limitation was related to the inability of the reduced-order model (shown in Fig. 33) to explicitly account for the tapered profile of the steel decking. Shell element A has constant width, l_1, which does not capture the tapered profile of the rib. For structural modeling, this limitation was addressed by considering the concrete area outside the tapered boundaries as having negligible mechanical strength. Thus, for a given thickness, t_i, and width of the concrete layer, l_1, the tapered rib can be considered by changing the ratio of reinforcement (FRACR) in the material model used to model the composite slab (MAT_172, discussed in Section 3.1.2), as shown in Fig. 35. The area of reinforcement with negligible strength is calculated by subtracting the concrete area, A_i, from the total area of the layer ($l_1 \times t_i$). Thus, the area of concrete in the layer can be changed by changing the reinforcement ratio.

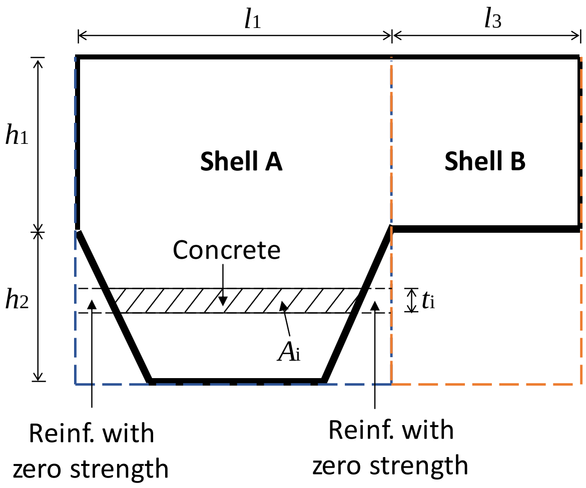

$$reinf\ ratio\ (FRACR) = \frac{(l_1 \cdot t_\mathrm{i} - A_\mathrm{i})}{l_1 \cdot t_\mathrm{i}}$$

Fig. 35. Consideration of the tapered profile of rib in the reduced-order model [Jiang et al. 2017].

It should be noted that the reduced-order model does not account for the possibility of debonding between the concrete slab and steel deck, which may occur at elevated temperatures. This debonding renders the steel deck ineffective and diminishes its contribution to the load bearing capacity of the slab. Special care must be exercised in this case to ensure that the material model for the steel deck has lost all its strength at elevated temperatures.

Following the reduced-order approach described above, the composite slab in the NIST NFRL CF2 Test, a plan view of which shown in Fig. 36, was divided into alternating strips of shell elements representing the thick and thin portions of the composite slab. The overall layout of the composite slab with alternating strips of shell elements in the computational model is shown in Fig. 37. In Fig. 37, alternating strips of shell elements are distinguished by different colors for the composite slab both in the test bay and surrounding bay areas.

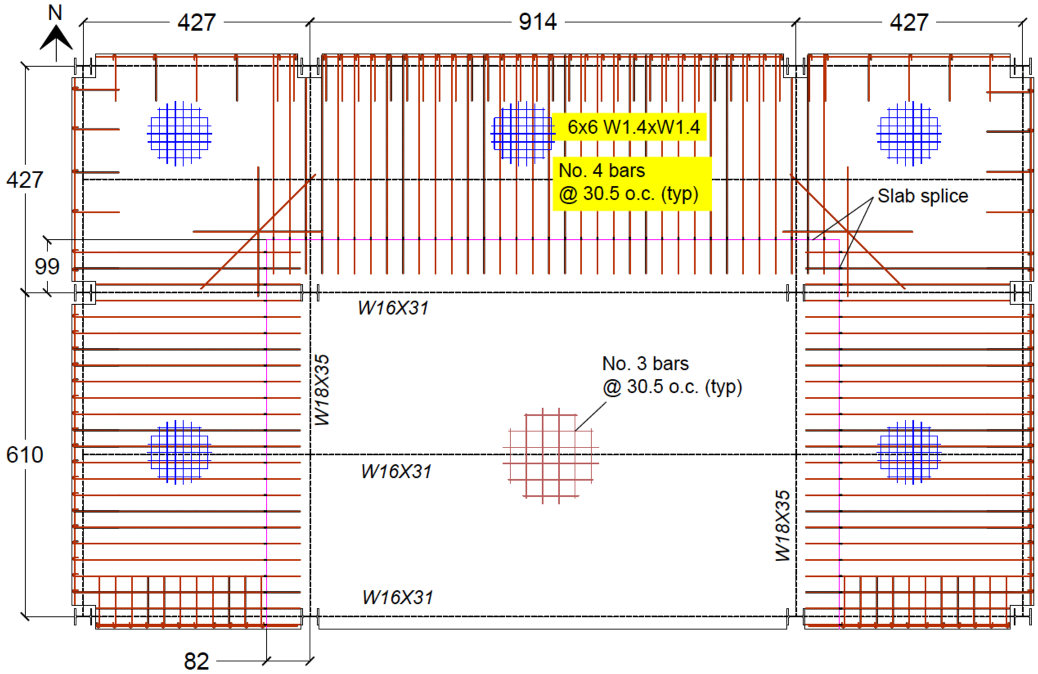

Fig. 36. The composite slab reinforcement details in the test bay and surrounding bay areas in the NIST NFRL CF2 Test: plan view (dimensions are in centimeters) [Choe et al. 2022].

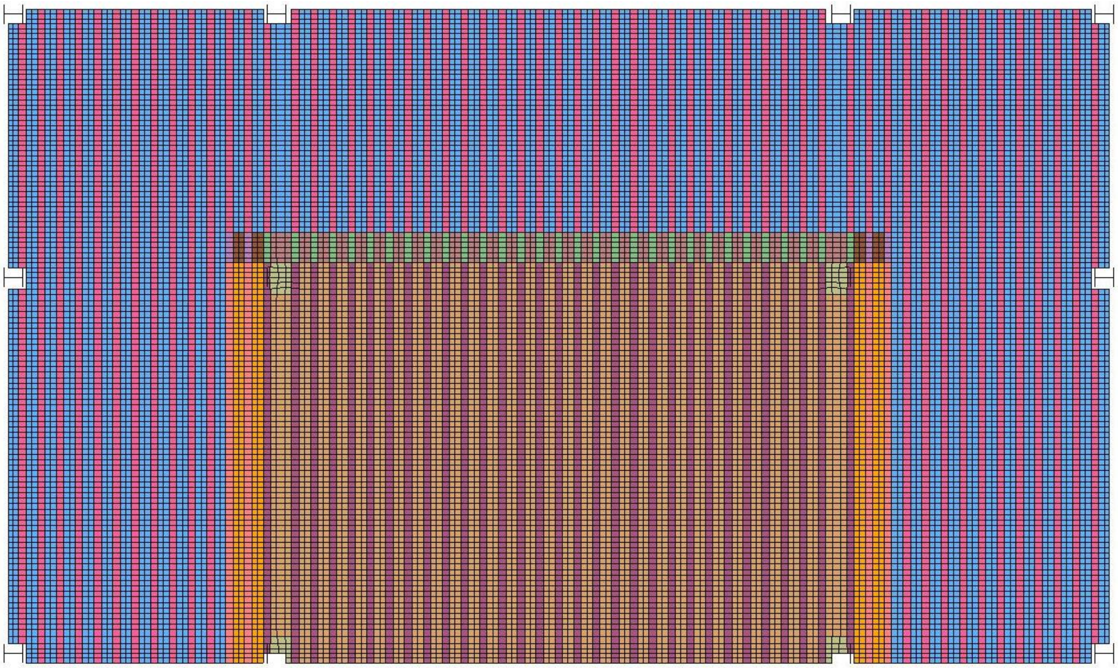

Fig. 37. Finite element formulation of composite slab in the test bay and surrounding bay areas: plan view.

The alternating strips of shell elements were each modeled by 25-layers representing the concrete slab, reinforcement, and steel deck composite shell sections. Figure 38 shows a section view of the composite slab modeled using the layered composite shell formulation. Note that, as further seen in Fig. 38, the rebars running in the north-south direction (Mat ID 1004) and the rebars running in the east-west direction (Mat ID 1003) were considered at two different depths.

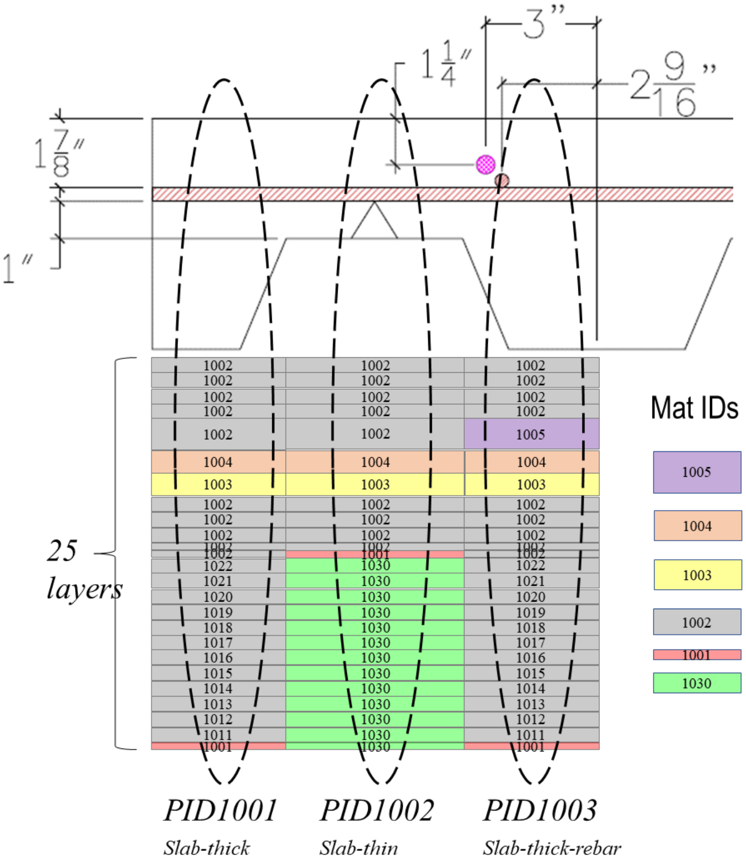

Fig. 38. Finite element formulation of composite slab in the test bay and surrounding bay areas: section view.

3.2.5. Contact Interfaces and Boundary Conditions

This section provides a brief overview of the method used to connect different elements of the composite steel frame in the computational model. It also provides information on the boundary conditions at column bases.

3.2.5.1. Contact Interfaces

Two distinct types of contact interfaces were used to prevent the interpenetration of different parts in the model and to permit transfer of bearing forces. A segment-based surface-to-surface contact interface (*CONTACT_AUTOMATIC_SURFACE_TO_SURFACE in LS-DYNA with SOFT = 2) was used in cases where contact was anticipated between the surfaces of different shell elements (e.g., contact between a shear connection plate and the web of a connected beam or between the floor slab and the top flange of a beam). A penalty-based single-surface contact interface (*CONTACT_AUTOMATIC_SINGLE_SURFACE in LS-DYNA with SOFT = 0) was used in cases where contact was anticipated between the edge of one shell element and the surface of another shell element (e.g., where the web and flanges of a beam could bind against a connection plate or the flange of a column, as illustrated in Fig. 39). Thickness offsets for shell elements were considered in all contact interfaces, and contact was assumed to be frictionless. Distinct part sets were used to identify which elements to include in each contact interface.

39

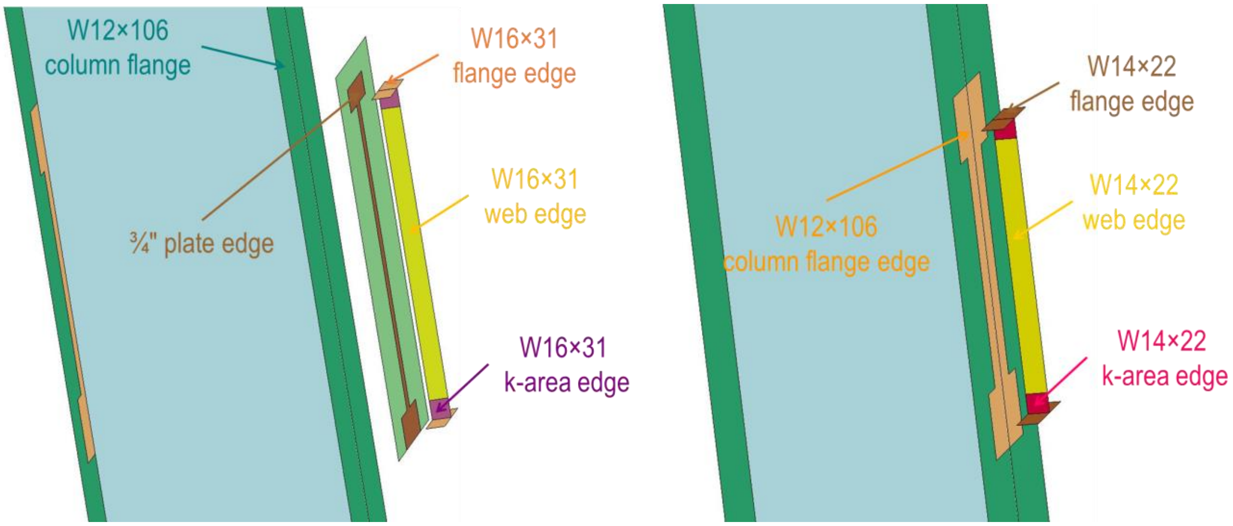

(a) W16×31 beam-to-endplate contact (b) W14×22 beam-to-column contact

Fig. 39. Modeling part-based contacts at the beam ends in the analysis of composite floor test.

3.2.5.2. Boundary Conditions

The degree of fixity at column bases was shown to be important in modeling the system response of the composite floor system. Through calibrations with a simple stiffness experiment (depicted in Fig. 40), the proper fixity was obtained and applied at column base plates to model the boundary conditions. Figure 41 depicts how these boundary conditions were defined at column base plates in finite element analysis. As shown in Fig. 42, the model matched the experiments quite well in predictions of stiffness. Specifically, the percent deviation between the predicted and measured loads corresponding to the maximum displacement of 15 mm (0.6 in) was about 4.8 %.

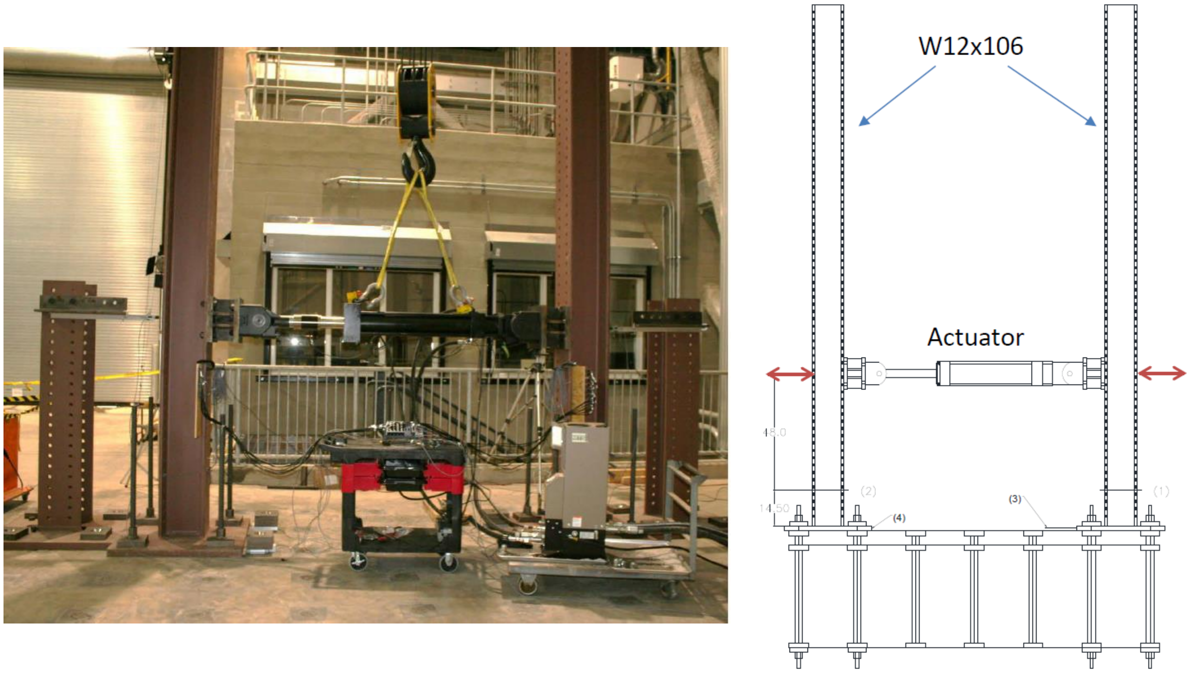

Fig. 40. Stiffness test to calibrate boundary conditions at the column base plates.

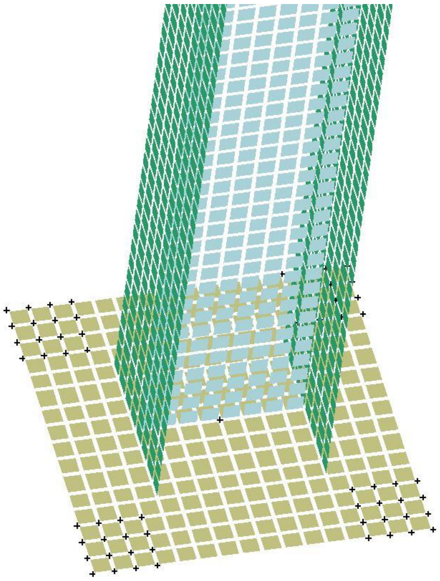

(a) Fixity at column base plates

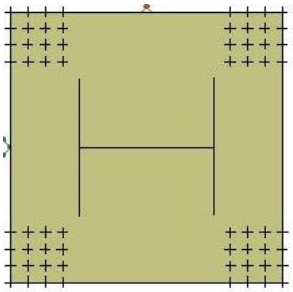

(b) Constrained DOF: X, Y, Z

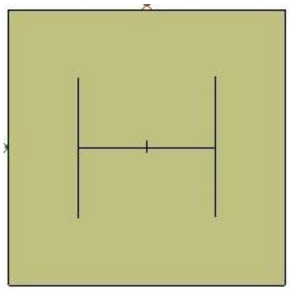

(c) Constrained DOF: X, Y, Z, RX, RY, RZ

Fig. 41. Modeling boundary conditions at the column base plate (constrained nodes are indicated by +).

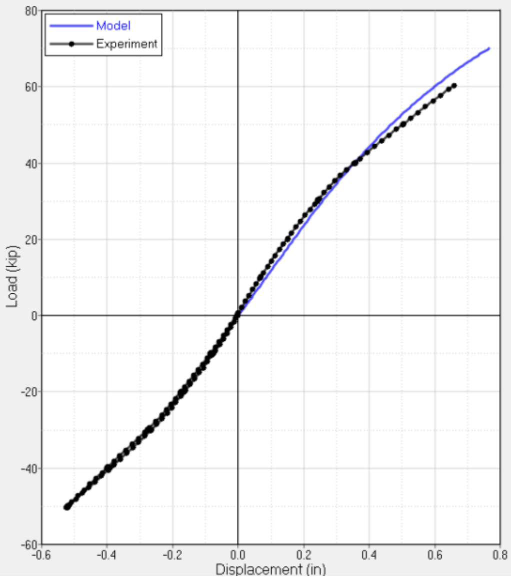

Fig. 42. Stiffness predictions from the model with calibrated boundary conditions at the column base plate.

3.3. Modeling Mechanical and Thermal Loads

The applied loads and temperatures in the computational model of the composite floor test followed the mechanical and thermal loads used in the NIST NFRL CF2 Test. This section provides details on the approaches adopted in the computational model of composite steel-framed structure to simulate the impact of the applied mechanical and thermal loads.

3.3.1. Applied Loads

In the NIST NFRL CF2 Test, a total gravity load of 5.2 kPa (0.75 psi) was applied to the test-bay floor slab. This total gravity load included the floor self-weight and the 2.5 kPa (0.36 psi) external load applied using hydraulic jacks (24 point loads of 6.2 kN (1.39 kips) as shown in Fig. 43). The total gravity load of 5.2 kPa (0.75 psi) was conformed to the gravity load demand determined from the ASCE 7 [American Society of Civil Engineers 2017] load combination for extraordinary events (1.2 times dead load plus 0.5 times live load). In addition, the surrounding floors were loaded by water-filled drums, providing an imposed gravity load of 1.2 kPa (0.17 psi), equivalent to 50 % of an office live load as specified in the ASCE 7 standard [American Society of Civil Engineers 2017]. Figure 43 shows the mechanical loading arrangement.

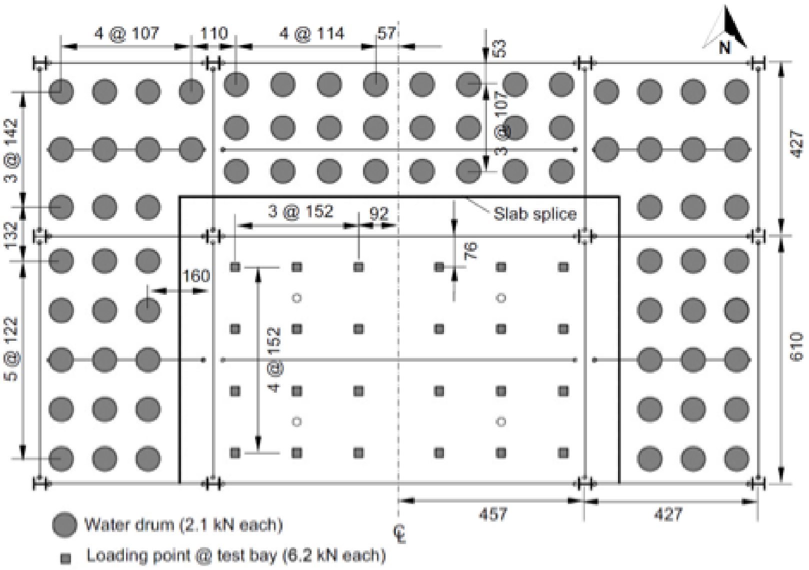

Fig. 43. Load application scheme in the NIST NFRL CF2 Test [Choe et al. 2022].

Mechanical loads (both external and gravity loads) were applied as point loads distributed on the composite slab in both the test bay and surrounding areas. The *LOAD_NODE_SET feature in LS-DYNA was used to define mechanical loads. The application of mechanical loads in the simulation of the composite steel frame is shown in Figs. 44, 45, and 46. For the exposed slab in Fig. 44, the point loads with the magnitude of 12 kN (2.70 kips) represented the external loads from hydraulic jacks and the self-weight of the exposed slab. For the unexposed slab in Fig. 45, the point loads with the magnitude of 5.4 kN (1.21 kips) represented the water drum weights and self-weight of the unexposed slab. Note that the locations of load application in Figs. 44, and 45 were the same as those shown in Fig. 43 for the experiment. For the part of floor slab referred to as the boundaries of the exposed slab in Fig. 46, the point loads with the magnitude of 3.3 kN (0.74 kips) represented the self-weight of the boundaries of the exposed slab.

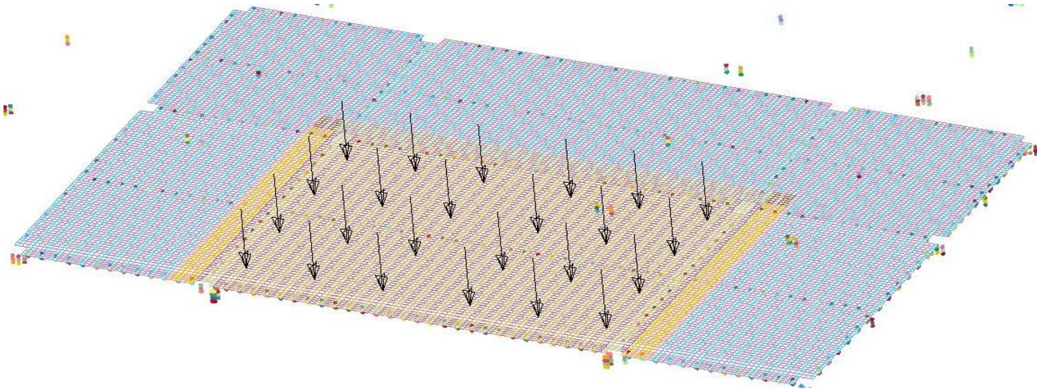

Fig. 44. Load application in the computational model of NIST NFRL CF2 Test: 12 kN (2.70 kips) point loads representing the external loads and self-weight of the exposed slab.

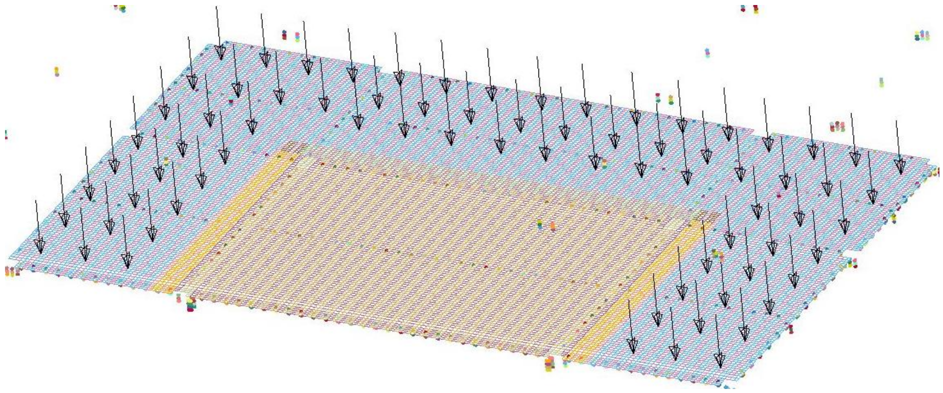

Fig. 45. Load application in the computational model of NIST NFRL CF2 Test: 5.4 kN (1.21 kips) point loads representing the water drum weights and the self-weight of the unexposed slab.

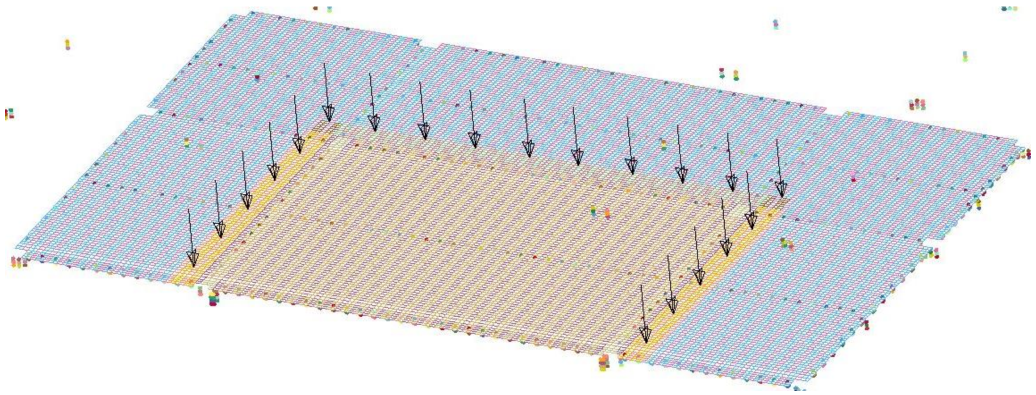

Fig. 46. Load application in the computational model of NIST NFRL CF2 Test: 3.3 kN (0.74 kips) point loads representing the self-weight of the boundaries of exposed slab.

3.3.2. Applied Temperatures

The enclosure fire in the NIST NFRL CF2 Test closely followed the standard fire exposure defined in ASTM E119 [ASTM International 2022c]. This can be seen in Fig. 47, in which the average upper gas layer (UGL) temperatures measured during the first 120 minutes of the CF2 Test are plotted against the ASTM E119 standard temperature-time curve [ASTM International 2022c].

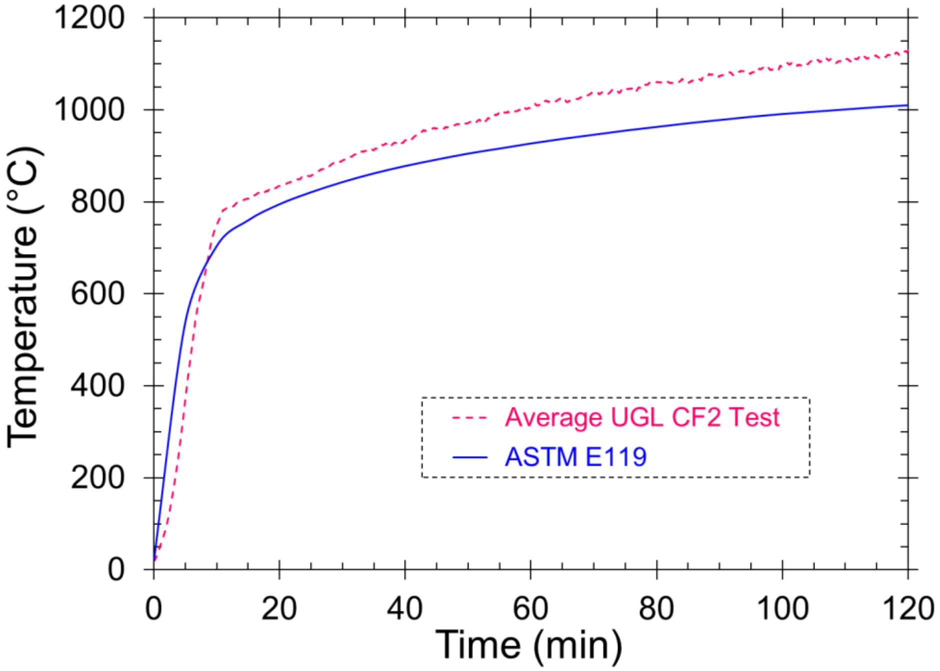

Fig. 47. The average upper gas layer (UGL) temperature in the NIST NFRL CF2 Test and the temperature-time curve defined in the ASTM E119 standard [ASTM International 2022c].

Measured temperature rise in different components of the composite floor system due to exposure to the compartment fire during the CF2 Test (shown in Fig. 47) was used as input temperature in lieu of a thermal analysis. This approach eliminated the uncertainties resulting from the heat transfer analysis on the overall capability of the model in capturing the structural response to the fire environment and allowed for a simplified validation of the modeling approach by conducting structural analysis only.

This section provides details of the time-temperature curves, applied to different components of the composite steel frame in the test bay. The section further describes the implementation of the thermal loading in the computational model of the composite steel frame.

3.3.2.1. Steel Beam and Girder Temperatures

During the NIST NFRL CF2 Test, temperatures of secondary W16×31 beams and W18×35 girders were measured at different locations both along their lengths and across their cross sections. These temperature probe locations are shown in Figs. 48 and 49, respectively.

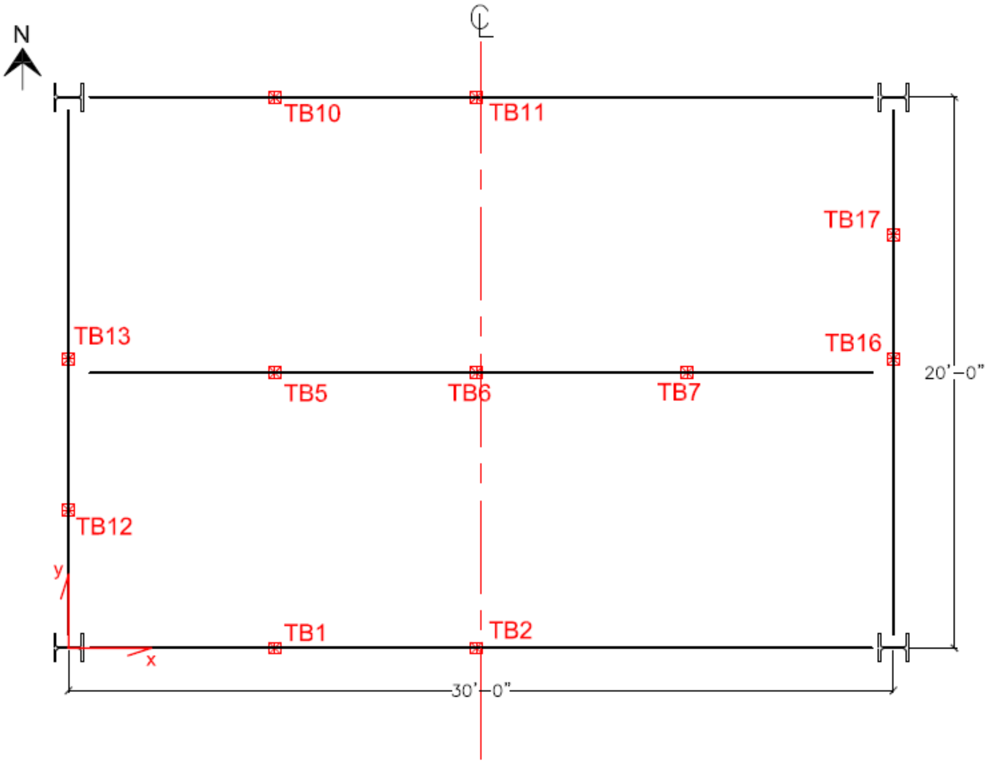

Fig. 48. Location of temperature measurement along the length of steel beams and girders of the test bay in the NIST NFRL CF2 Test [Choe et al. 2022].

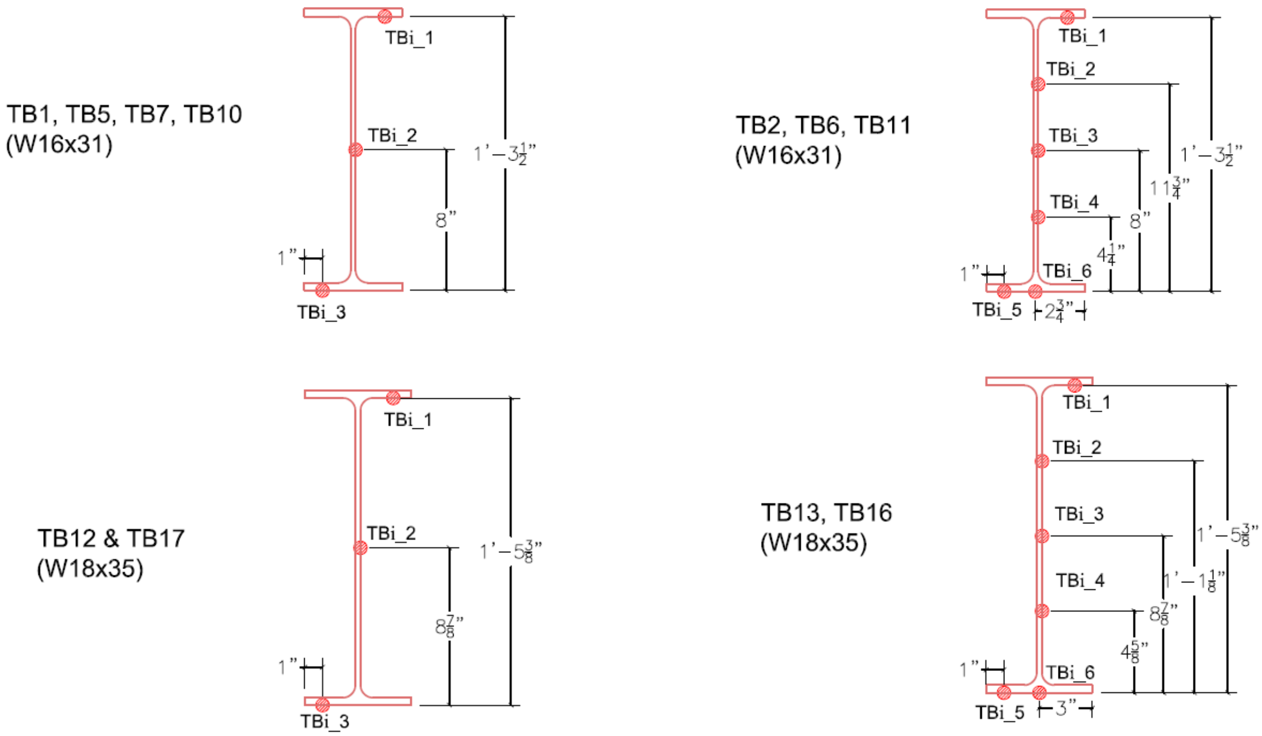

Fig. 49. Location of temperature measurement over the cross-section of steel beams and girders in the NIST NFRL CF2 Test [Choe et al. 2022].

In the computational model of the composite floor system, temperatures of steel beams and girders were defined using the measured temperature histories at discreet locations indicated in Figs. 48 and 49. Specifically, the temperatures measured at the midspan of steel beams and girders (locations TB2/TB6/TB11 for W16×31 beams, and TB13/TB16 for W18×35 girders in Fig. 48.) were applied uniformly across the entire length of steel beams and girders. To define the temperature gradient over the cross-section of steel beams and girders, temperatures measured at locations TBi_6, TBi_3, and TBi_1 in Fig. 49. were used as bottom flange, web, and top flange temperatures, respectively.

Representatives for temperature assignments are shown in Figs. 50, 51, and 52 where measured and applied temperatures at location TB6 on the middle W16×31 beam were compared. Specifically, Fig. 50. shows the temperature histories for the bottom flange of the middle W16×31 beam. The measured temperatures for the bottom flange of the middle W16×31 beam at locations TB6_5 and TB6_6 were essentially the same. The temperature history at TB6_6 was selected to apply in the model since a complete temperature-time history was available at TB6_6 for the duration of the test. Further, Fig. 51. shows the temperature histories for the web of the middle W16×31 beam. The measured temperatures at the mid-height of the web (location TB6_3) were selected as applied temperatures to the web of the middle W16×31 beam. Similarly, the applied temperatures to the top flange of the middle W16×31 are presented in Fig. 52.

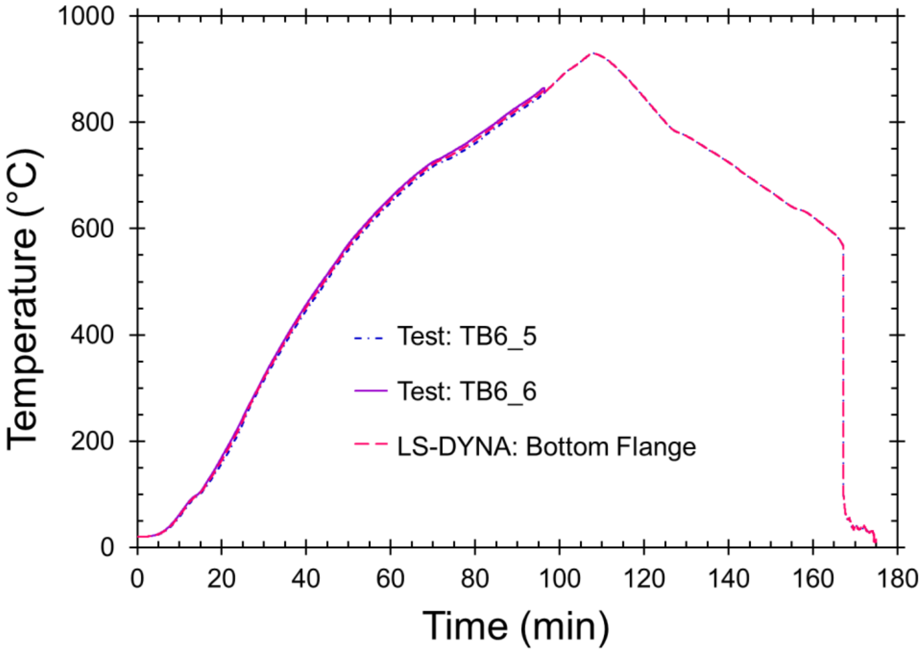

Fig. 50. Measured and applied temperature histories at the bottom flange of the middle W16×31 beam (location TB6).

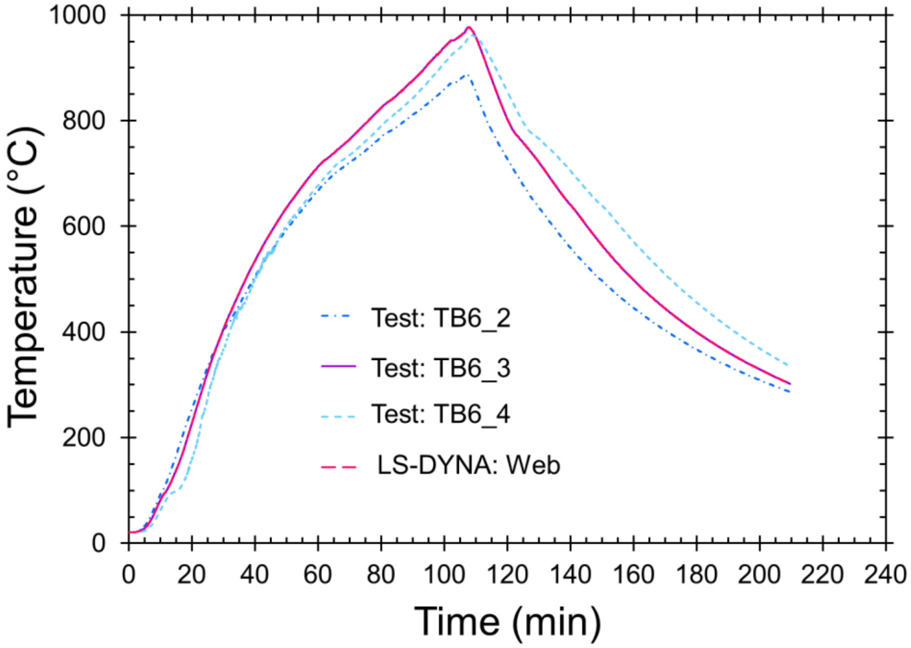

Fig. 51. Measured and applied temperature histories at the web of the middle W16×31 beam (location TB6).

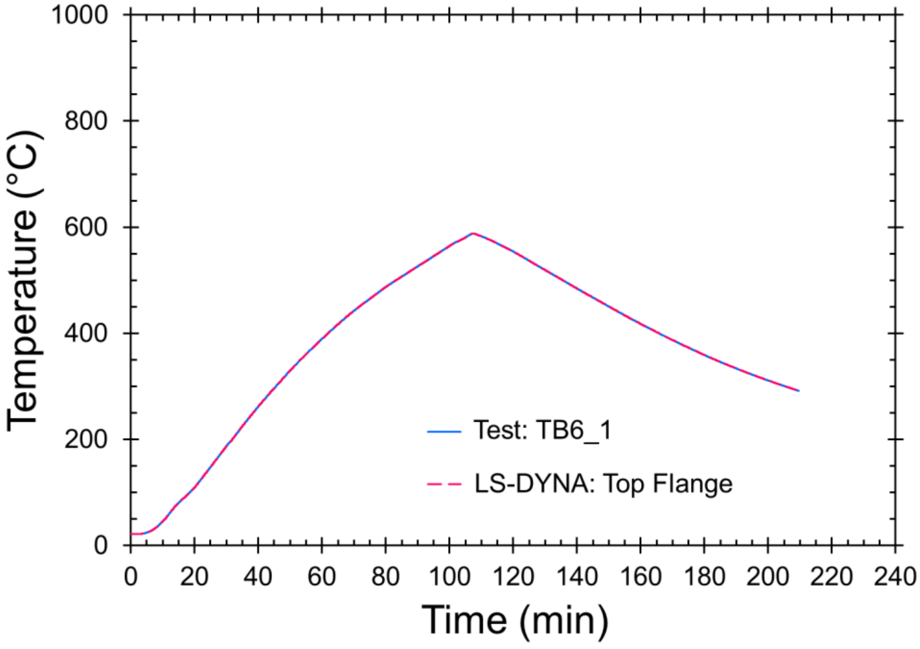

Fig. 52. Measured and applied temperature histories at the top flange of the middle W16×31 beam (location TB6).

The applied temperature-time curves for steel beams and girders, representative of which shown in Figs. 50, 51, and 52, were implemented in LS-DYNA using the feature *LOAD_THERMAL_VARIABLE. Specifically, temperature-time curves were defined in LS-DYNA using the *DEFINE_CURVE feature and were called out in the feature *LOAD_THERMAL_VARIABLE using the parameter LCID (load curve ID). The temperature-time curves were then assigned to specific parts of the beams and girders cross sections using the parameter NSID (node set ID). As an example, the temperature assignments using node-set approach are shown in Figs. 53, 54, and 55, where node sets were defined for the bottom flange, the web, and the top flange of the middle W16×31 beam, respectively. Note that the temperature-time curves selected based on the measurements at the mid-length of beams and girders (e.g., at location TB6 for the middle W16×31 beam) were assigned to the entire beams and girders length. In other words, no temperature variations were considered along the length of beams and girders.

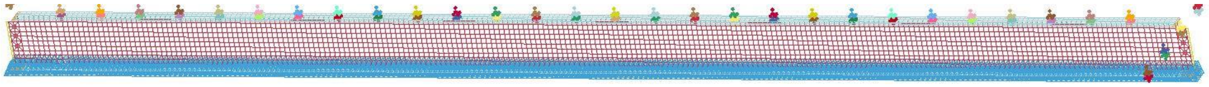

(a) Entire beam view

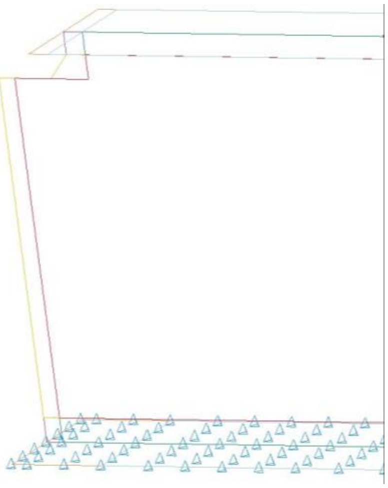

(b) Close-up view

Fig. 53. Node set definition to assign temperatures to the bottom flange of the middle W16×31 beam: (a) entire beam view; (b) close-up view.

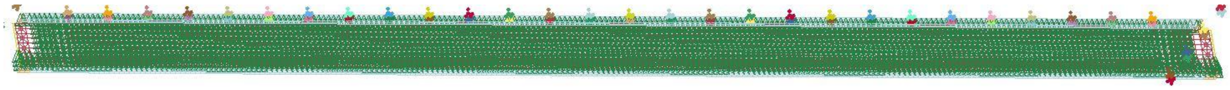

(a) Entire beam view

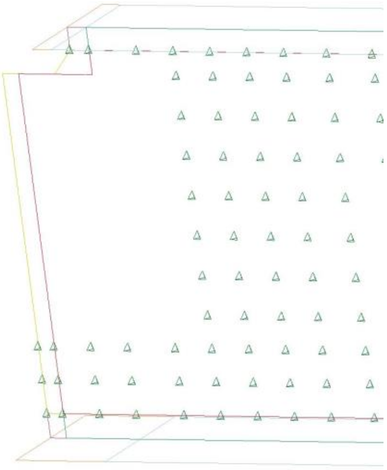

(b) Close-up view

Fig. 54. Node set definition to assign temperatures to the web of the middle W16×31 beam: (a) entire beam view; (b) close-up view.

(a) Entire beam view

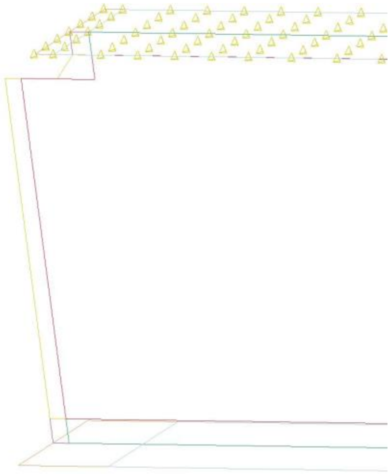

(b) Close-up view

Fig. 55. Node set definition to assign temperatures to the top flange of the middle W16×31 beam: (a) entire beam view; (b) close-up view.

3.3.2.2. Shear Stud Temperatures

During the NIST NFRL CF2 Test, temperatures of shear studs connected to the top flanges of the secondary W16×31 beams and the W18×35 girders were measured at the mid-length of beams and girders. These temperature probe locations are shown in Fig. 56. The S2, S6, and S11 were located at the mid-length of beams, and S13, and S16 were at the mid-length of girders. Figure 57 further shows the locations of temperature measurement for shear studs over the cross-section of composite steel beams and girders.

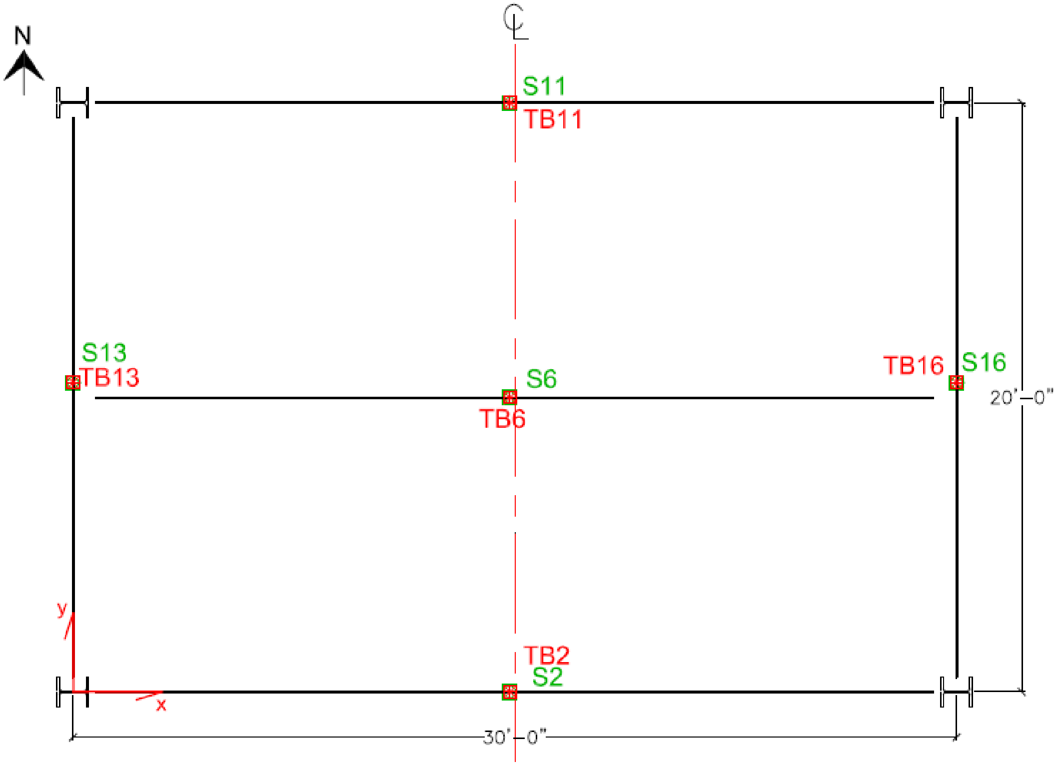

Fig. 56. Location of temperature measurement for shear studs at midspan of steel beams and girders of the test bay in the NIST NFRL CF2 Test [Choe et al. 2022].

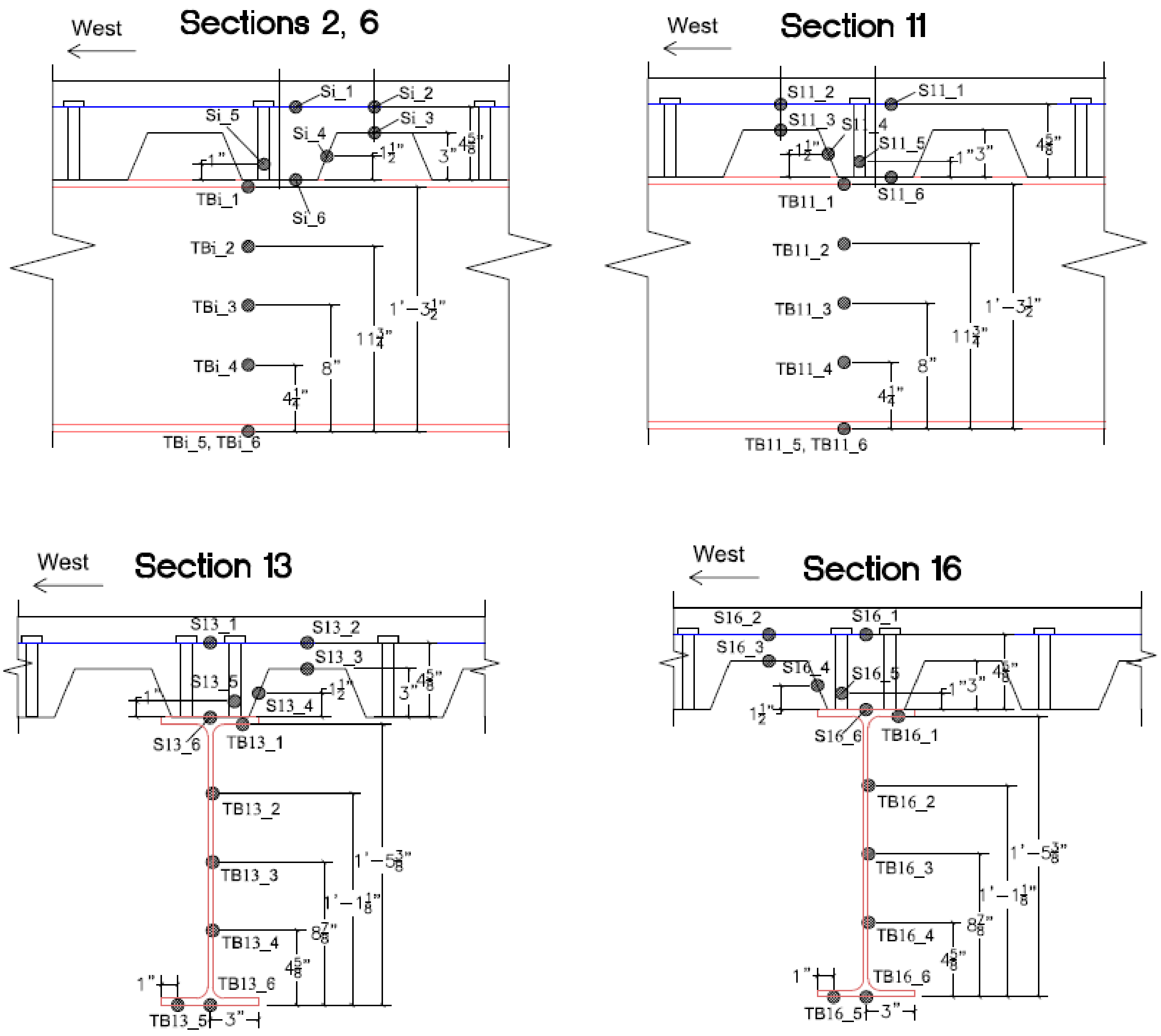

Fig. 57. Location of temperature measurement for shear studs over the cross-section of composite steel beams and girders in the NIST NFRL CF2 Test [Choe et al. 2022].

In the computational model of the composite floor system, shear stud temperatures were defined using the measured temperature histories at discreet locations indicated in Figs. 56 and 57. A representative for this definition is shown in Fig. 58 where measured and applied temperatures at location S6 at the midspan of the middle W16×31 beam were compared.

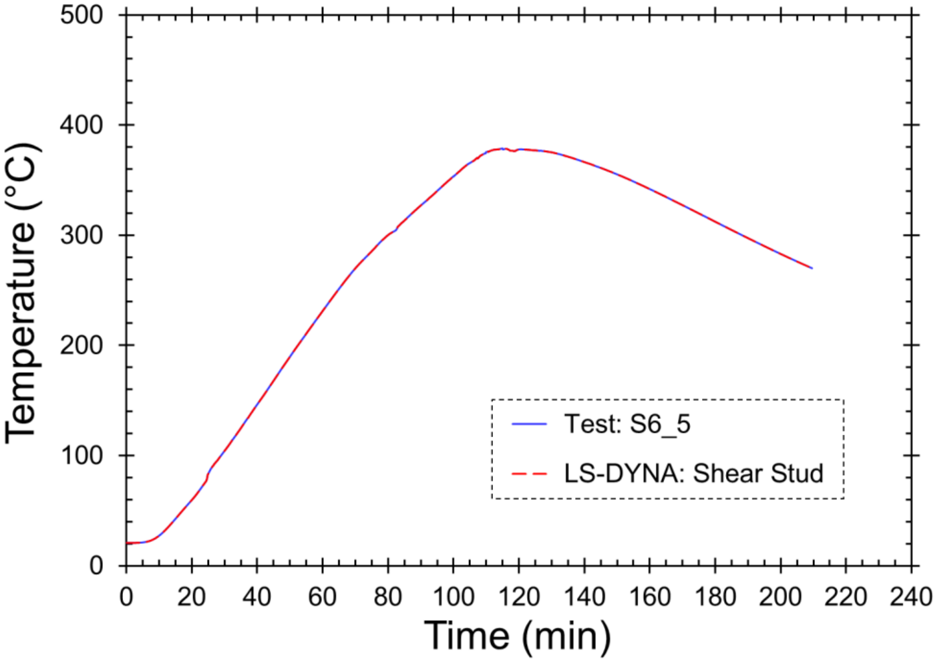

Fig. 58. Measured and applied temperature histories for the shear stud at midspan of the middle W16×31 beam (location S6).

The applied temperature-time curves for shear studs, representative of which shown in Fig. 58, were implemented in LS-DYNA using the feature *LOAD_THERMAL_VARIABLE. Specifically, temperature-time curves were defined in LS-DYNA using the *DEFINE_CURVE feature and were called out in the keyword *LOAD_THERMAL_VARIABLE using the parameter LCID (load curve ID). The temperature-time curves were then assigned to shear studs using the parameter NSID (node set ID). As an example, the temperature assignment using node-set approach is shown in Fig. 59, where node sets were defined for all shear studs connected to the top flange of the middle W16×31 beam. Note that the temperature-time curve selected based on the measurement at the mid-length of the middle W16×31 beam (e.g., at location S6 for the middle W16×31 beam) was assigned to all shear studs connected to the top flange of the middle W16×31 beam. In other words, no temperature variations for shear studs were considered along the length of beams and girders.

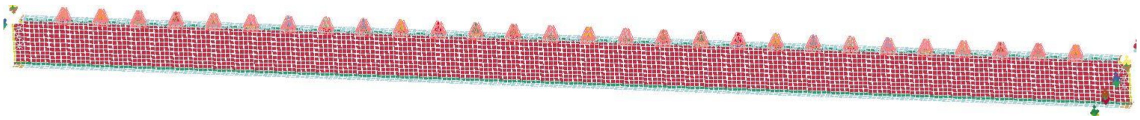

(a) Entire beam view

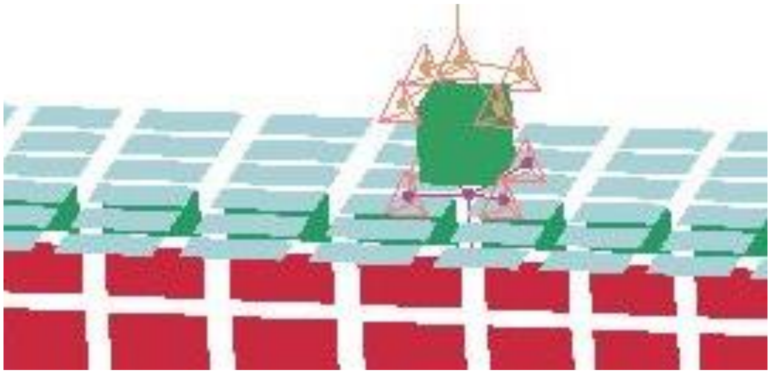

(b) Close-up view

Fig. 59. Node set definition to assign temperatures to the shear studs connected to the middle W16×31 beam: (a) entire beam view; (b) close-up view.

3.3.2.3. Connection Temperatures

During the NIST NFRL CF2 Test, temperatures in the connection regions were measured at different locations. These temperature probe locations, both at the ends and over the cross sections of secondary W16×31 beams and W18×35 girders, are shown in Fig. 60, and Figs. 61 to 65, respectively.

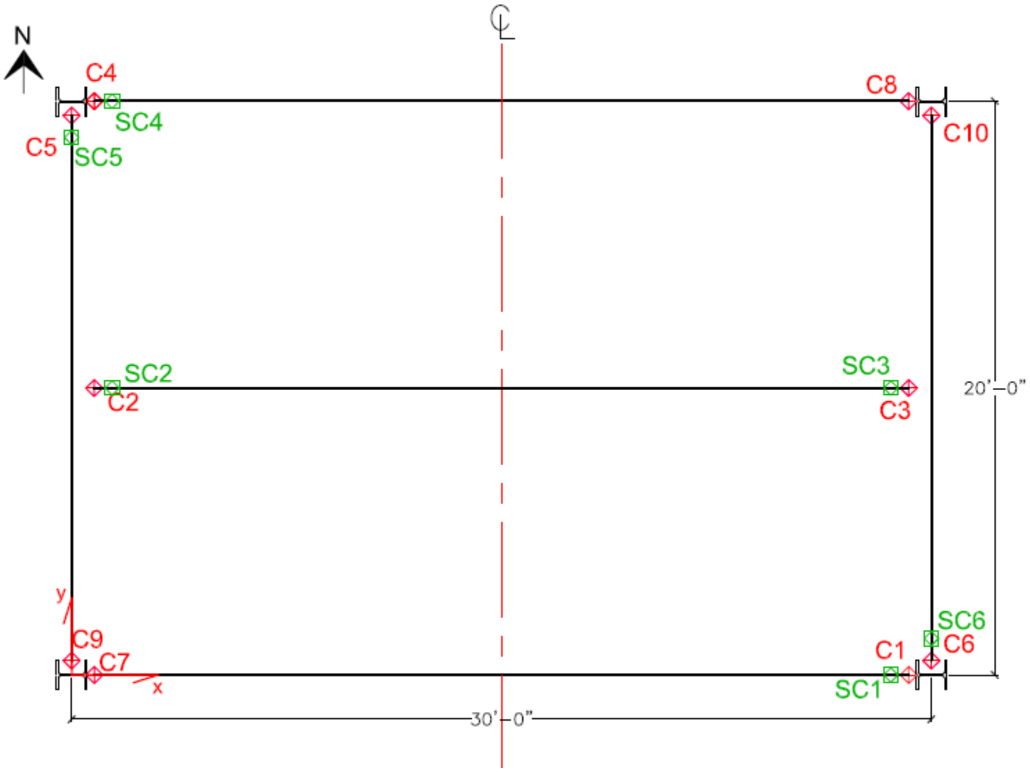

Fig. 60. Locations of temperature measurement at the connection regions of the test bay in the NIST NFRL CF2 Test [Choe et al. 2022].

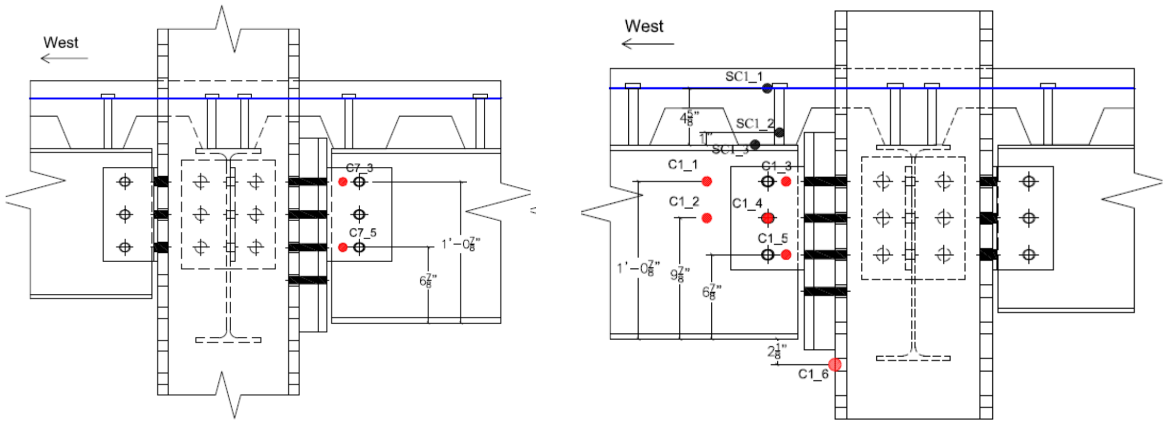

(a) Section 7 (C7)

(b) Section 1 (C1)

Fig. 61. Locations of temperature measurement at the end connections of the south W16×31 beam in the NIST NFRL CF2 Test [Choe et al. 2022].

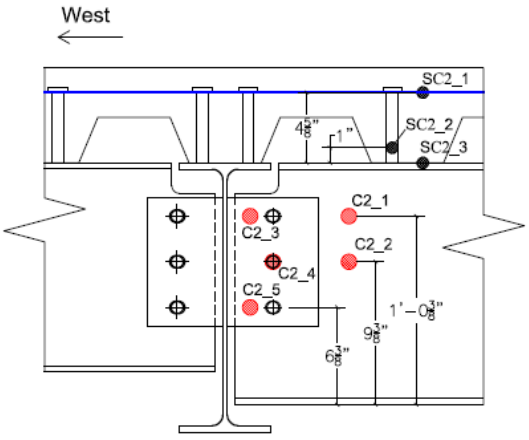

(a) Section 2 (C2)

(b) Section 3 (C3)

Fig. 62. Locations of temperature measurement at the end connections of the middle W16×31 beam in the NIST NFRL CF2 Test [Choe et al. 2022].

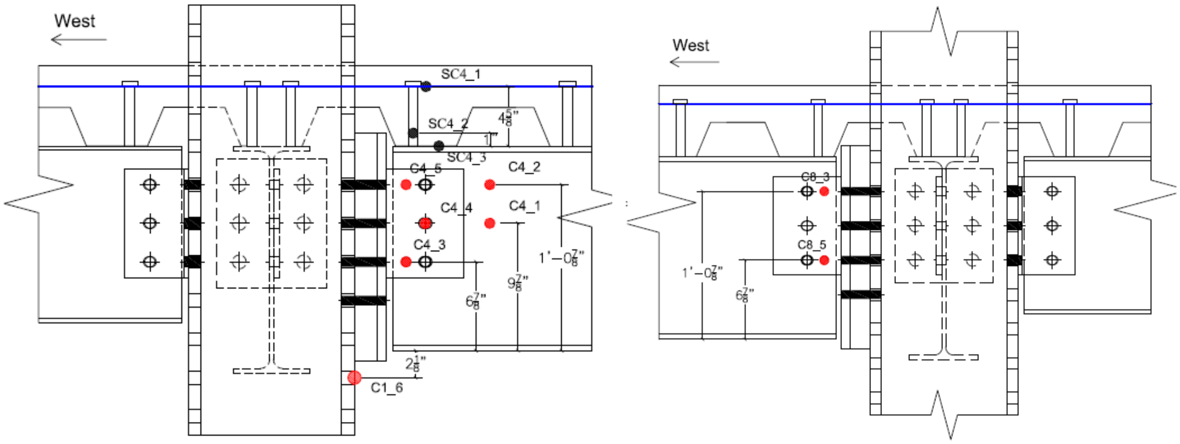

(a) Section 4 (C4)

(b) Section 8 (C8)

Fig. 63. Locations of temperature measurement at the end connections of the north W16×31 beam in the NIST NFRL CF2 Test [Choe et al. 2022].

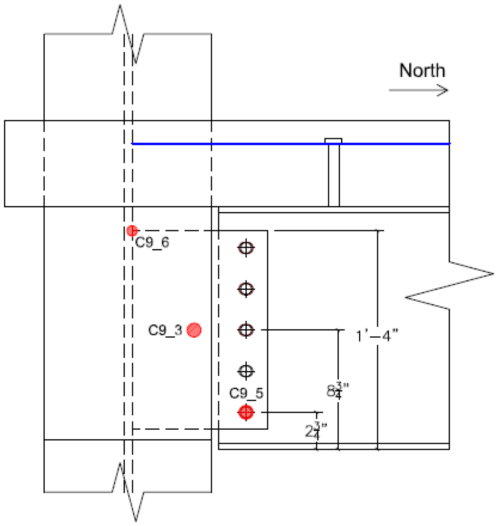

(a) Section 9 (C9)

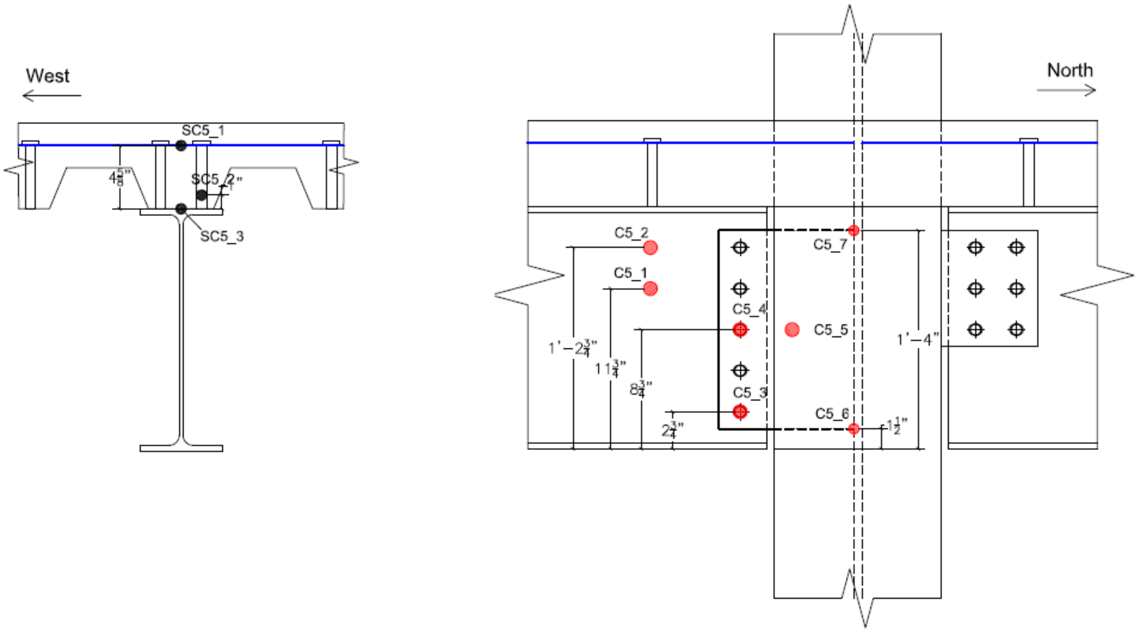

(b) Section 5 (C5)

Fig. 64. Locations of temperature measurement at the end connections of the west W18×35 girder in the NIST NFRL CF2 Test [Choe et al. 2022].

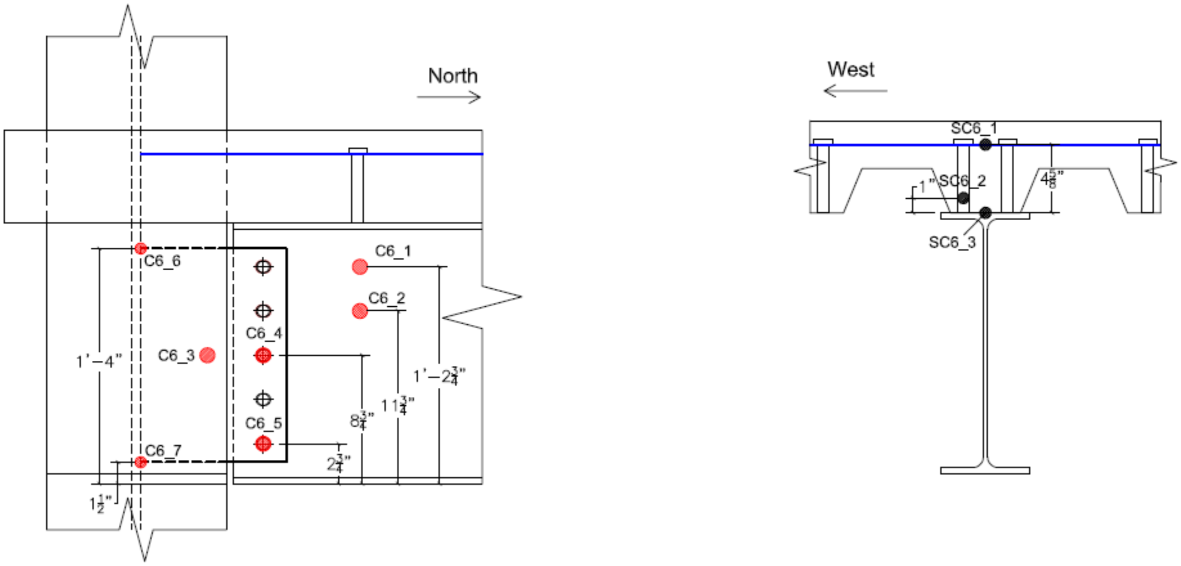

(a) Section 6 (C6)

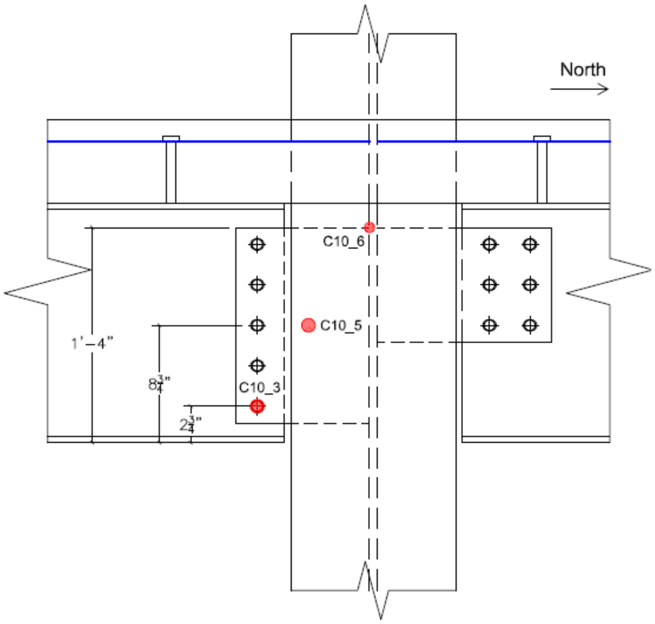

(b) Section 10 (C10)

Fig. 65. Locations of temperature measurement at the end connections of the east W18×35 girder in the NIST NFRL CF2 Test [Choe et al. 2022].

In the computational model of the composite floor system, temperatures in the connection regions were defined using the measured temperature histories at discreet locations indicated in

Figs. 60 to 65. Representatives for this definition are shown in Figs. 66 and 67 where measured and applied temperatures were compared at southeast connections C1 and C6, respectively (refer to Fig. 60 for the locations of connections C1 and C6). The measured temperature histories were averaged to model connection temperatures. For example, the temperature-time curve for the connection C1 ("LS-DYNA: Southeast Connection" curve in Fig. 66) is the average of measured temperature curves at locations C1_1, C1_2, C1_3, C1_4, and C1_5.

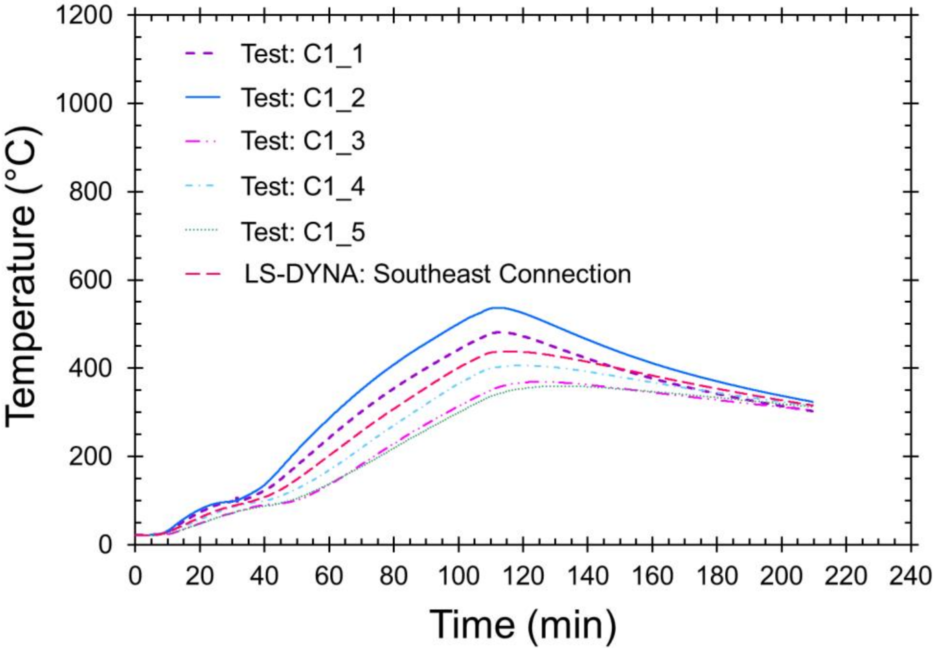

Fig. 66. Measured and applied temperature histories at the southeast connection C1 (see Fig. 60 for the location of connection C1).

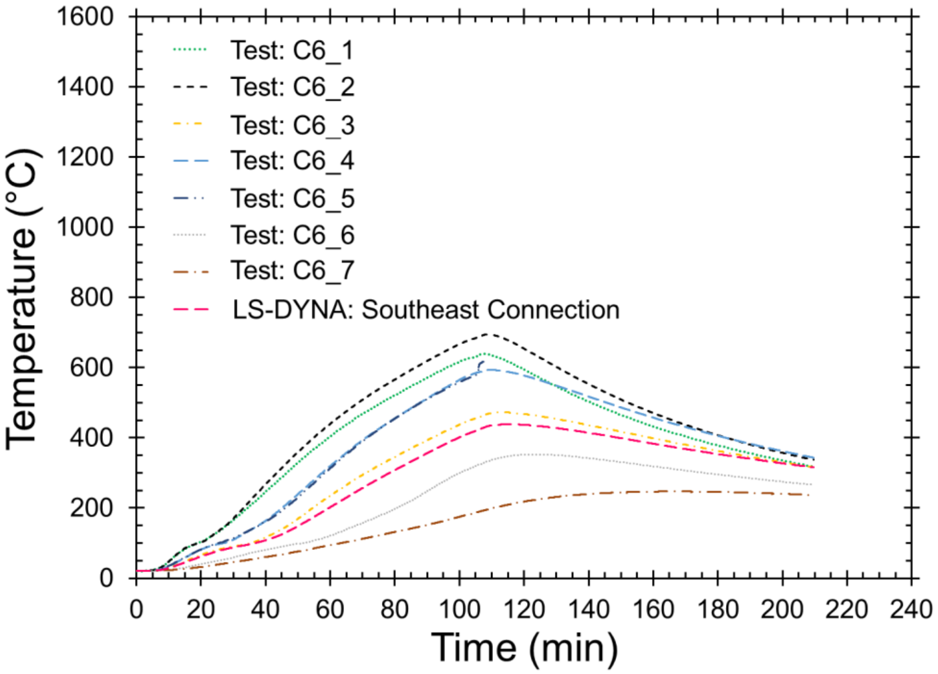

Fig. 67. Measured and applied temperature histories at the southeast connection C6 (see Fig. 60 for the location of connection C6).

The applied temperature-time curves for connections, representatives of which shown in Figs. 66 and 67, were implemented in LS-DYNA using the feature *LOAD_THERMAL_VARIABLE. Specifically, temperature-time curves were defined in LS-DYNA using the *DEFINE_CURVE feature and were called out in the keyword *LOAD_THERMAL_VARIABLE using the parameter LCID (load curve ID). The temperature-time curves were then assigned to connections using the parameter NSID (node set ID). As an example, the temperature assignment using node-set approach is shown in Fig. 68, where a node set was defined for the south connection of the east W18×35 girder (connection C6). Note that the connection temperatures were uniformly assigned to the shear tab plates.

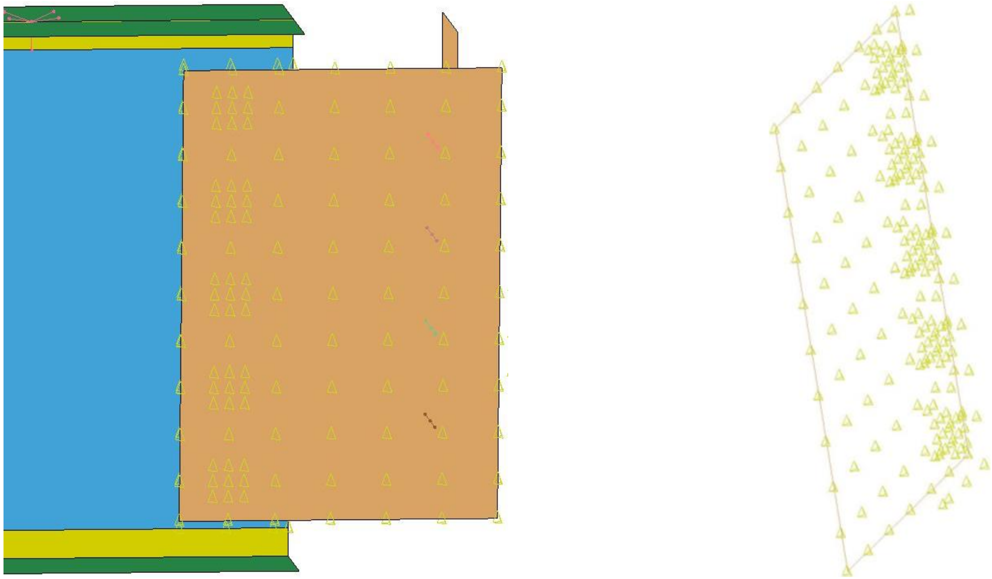

(a) Extended shear tab connection (b) Shear tab plate

Fig. 68. Node set definition to assign temperatures to the south connection of the east W18×35 girder (connection C6): (a) extended shear tab connection; (b) shear tab plate.

3.3.2.4. Slab Temperatures

During the NIST NFRL CF2 Test, temperatures of the composite slab of the test bay were measured at different slab locations both on its surface and throughout its cross section. These temperature probe locations are shown in Figs. 69 and 70, respectively.

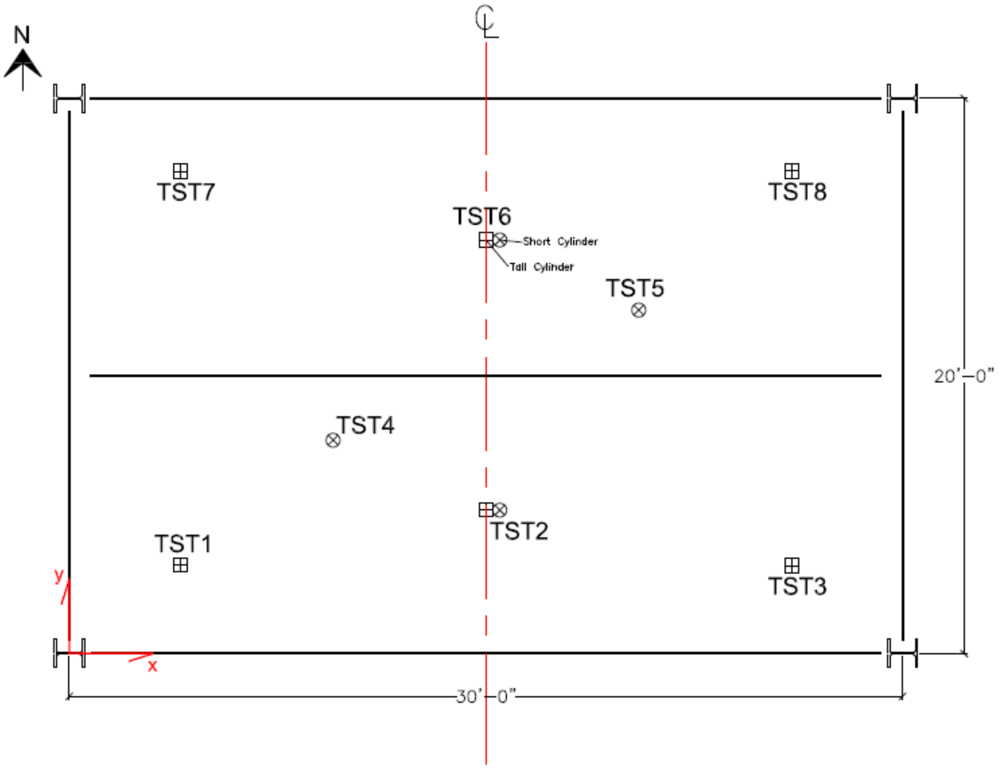

Fig. 69. Locations of temperature measurement for the composite slab of the test bay in the NIST NFRL CF2 Test [Choe et al. 2022].

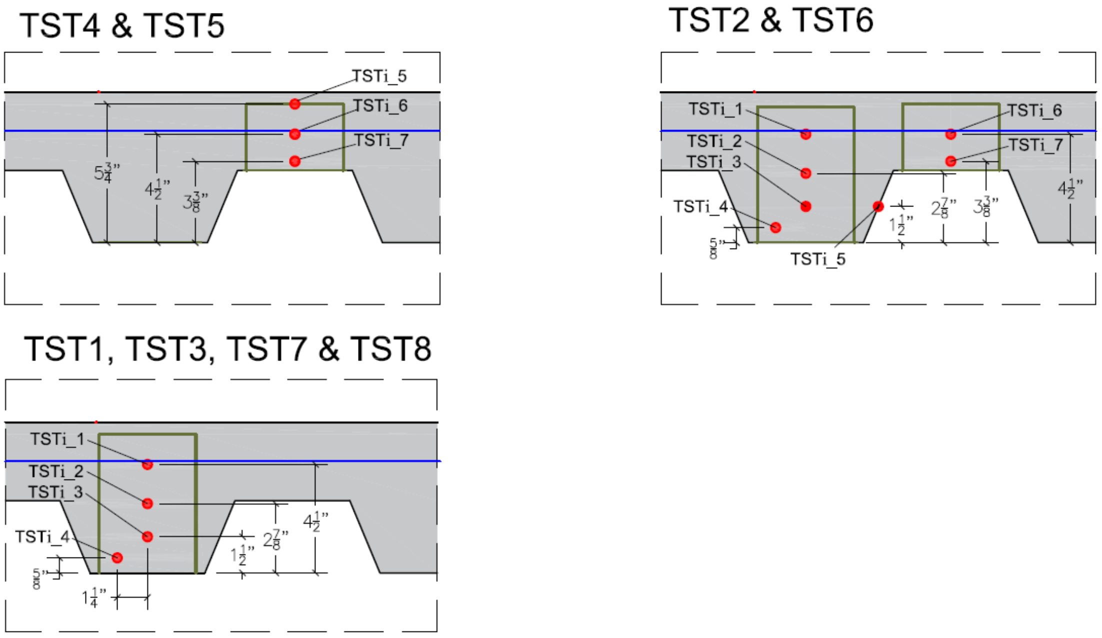
TST4 & TST5

TST2 & TST6

TST1, TST3, TST7 & TST8

Fig. 70 Locations of temperature measurement over the cross-section of composite slab of the test bay in the NIST NFRL CF2 Test [Choe et al. 2022].

In the computational model of the composite floor system, slab temperatures were defined using the measured temperature histories at locations TST2 and TST6, indicated in Figs. 69 and 70. The measured temperatures at locations TST2 and TST6 were used to define applied temperatures for the south and north composite slabs, respectively. Specifically, the measured temperatures at the lowest point in the thick part of the slab were used as the base temperature to generate temperature distributions through the slab thickness. In other words, the applied temperatures were matched with the temperature-time curves measured at locations TST2_4 and TST6_4 to define temperatures for the south and north composite slabs, respectively. These temperature-time curves are shown in Figs. 71 and 72. As observed in Figs. 71 and 72, compared to the south composite slab, the north composite slab was subjected to higher temperatures in an exposure to the test fire.

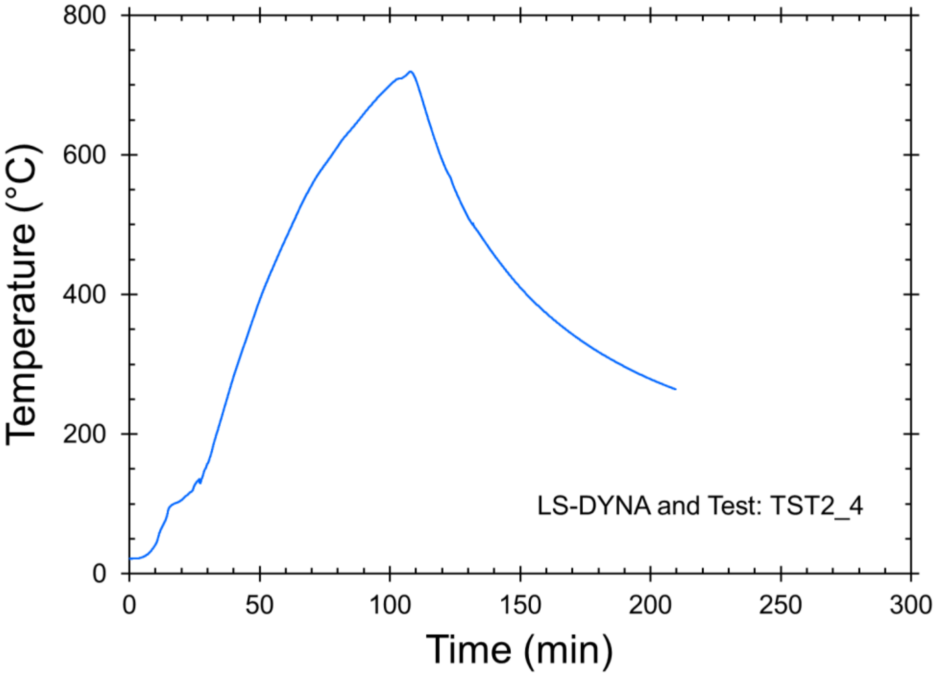

Fig. 71. The temperature-time curve at location TST2_4 used to model through-thickness temperatures for the south composite slab in the simulation.

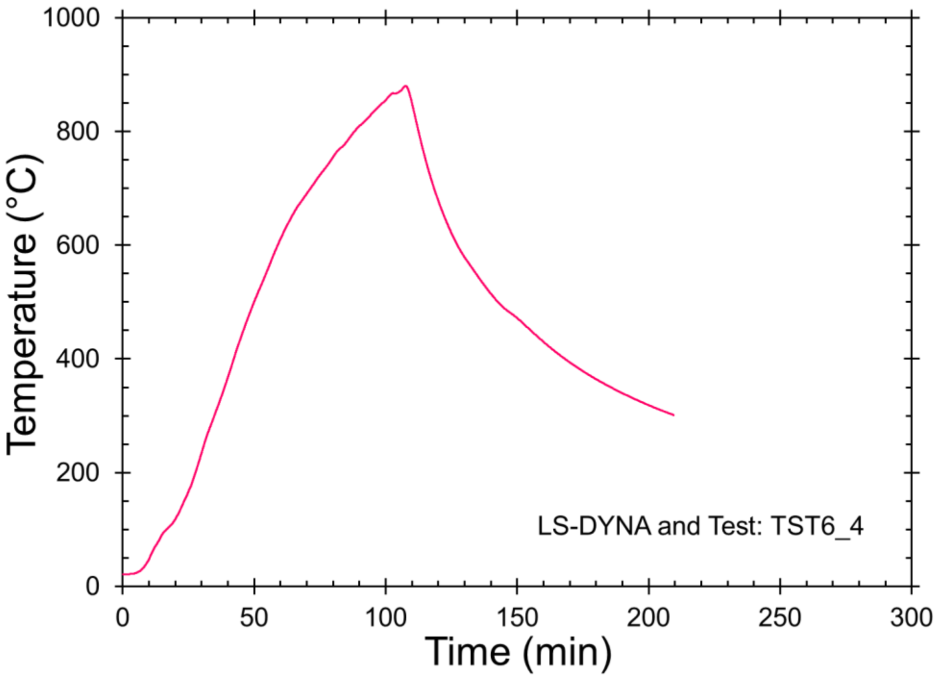

Fig. 72. The temperature-time curve at location TST6_4 used to model through-thickness temperatures for the north composite slab in the simulation.

Using a heat transfer analysis (conducted in a previous study by the authors [Jiang et al. 2017]) calibrated with actual temperatures measured at different points through the thickness of the slab, a temperature distribution along the depth of the composite slab was established. A representative of the modeled temperature distribution is shown in Fig. 73 for the thick portion of the south slab. As seen in Fig. 73, this calibration procedure resulted in a parabolic distribution of temperatures through the thickness of the slab. Further, the modeled temperature distributions through the thickness of the slab were defined using two coordinate parameters: ZCO and TSCALE. ZCO is a normalized through-thickness coordinate with values between –1.0 at the bottom of the slab (exposed surface) and +1 at the top of the slab (unexposed surface). TSCALE is a constant scale factor applied to temperature curves of TST2_4 for the south slab and TST6_4 for the north slab. Therefore, TSCALE is equal to unity at the locations of TST2_4 and TST6_4. The coordinate parameters ZCO and TSCALE were used as variables in the *LOAD_THERMAL_VARIABLE_SHELL_SET feature in LS-DYNA to implement the slab temperatures in the simulation of the composite floor system.

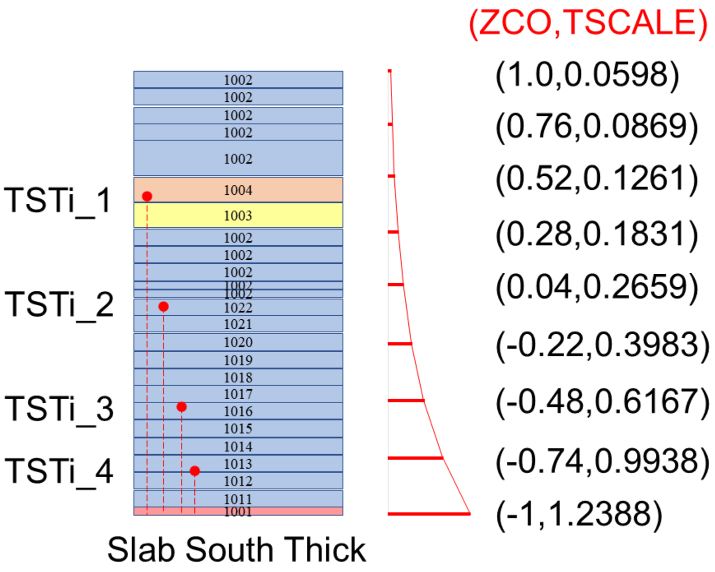

Fig. 73. Distribution of applied temperatures over the cross-section of the composite slab in the simulation.

The predicted temperature-time curves at different locations through the depth of the composite slab, compared with corresponding curves from the experiment, are presented in Figs. 74 and 75 for locations TST2 and TST6, in the middle of south and north slabs, respectively. As observed in Figs. 74 and 75, the temperature-time curves used in the simulation agree reasonably well with the corresponding curves measured in the experiment during the heating phase of the fire and up to the maximum exposure temperatures. Specifically, for locations TSTi_5, TSTi_4, and TSTi_3, the maximum percent deviation between the experimental and computational temperature curves corresponding to the maximum exposure temperature was about 5.3 %. For locations TSTi_1, and TSTi_2, the maximum percent deviation between the experimental and computational temperature curves corresponding to the maximum exposure temperature was about 33.3 %. This difference is reflective of the approximate nature of the temperature distribution assumed in the model.

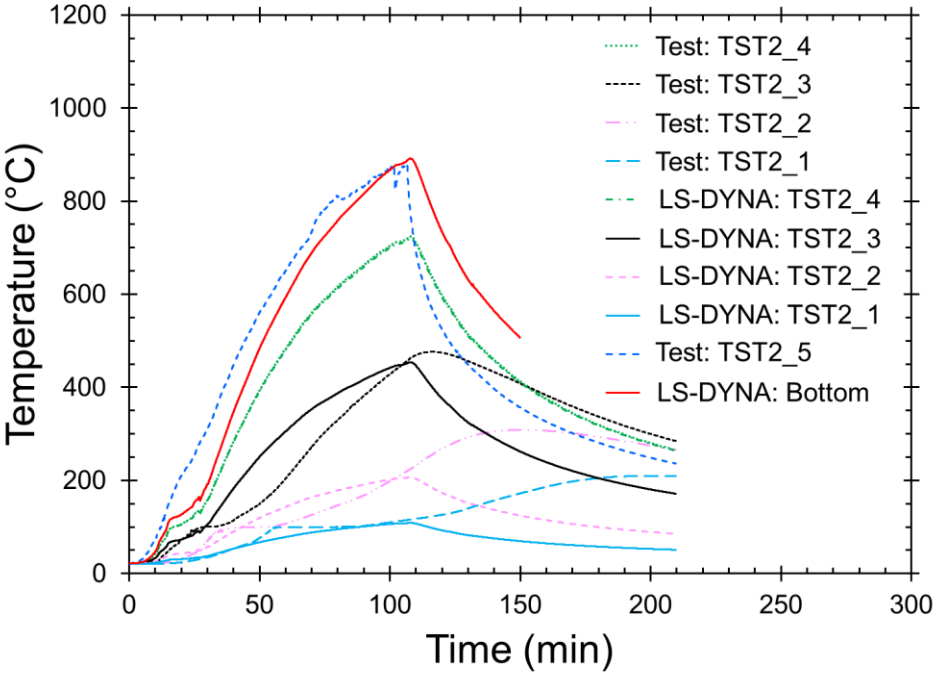

Fig. 74 Measured and applied temperature histories at the middle of south composite slab (location TST2 - thick section).

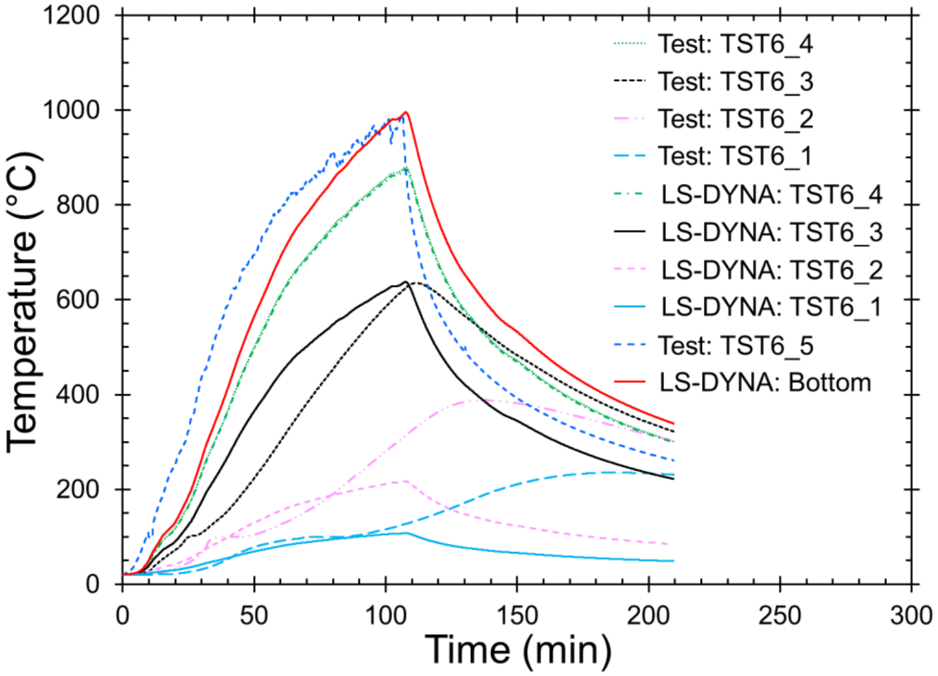

Fig. 75. Measured and applied temperature histories at the middle of north composite slab (location TST6 - thick section).

The applied temperature-time curves for the composite slab, representatives of which shown in Figs. 74 and 75, were implemented in LS-DYNA using the feature *LOAD_THERMAL_VARIABLE_SHELL_SET. Specifically, temperature-time curves were defined in LS-DYNA using the *DEFINE_CURVE feature and were called out in the feature *LOAD_THERMAL_VARIABLE_SHELL_SET using the variable TCURVE (curve ID for temperature vs. time curves presented in Figs. 71 and 72). The temperature-time curves were then assigned to the composite slab using the parameter SID (shell set ID). The temperature assignments for the composite slab using shell-set approach are shown in Figs. 76 to 79, where shell sets were defined for alternating strips of shell elements representing the thick and thin portions of both the south and the north composite slabs (shell sets are shown as strips of black color). Note that the slab temperatures were uniformly assigned over the length of each strip of shell elements.

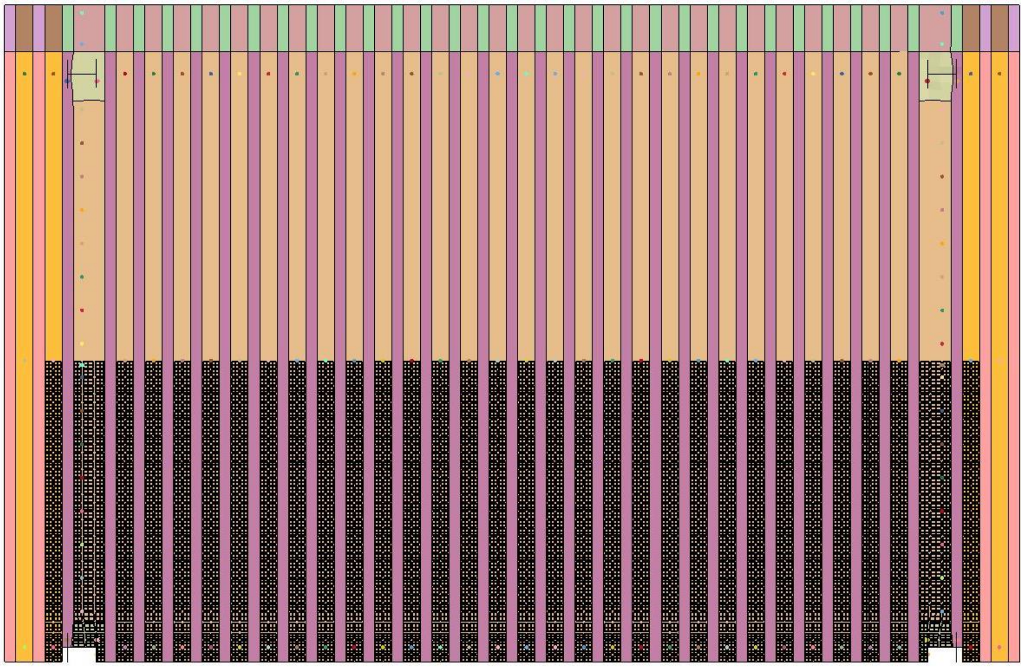

Fig. 76. Node set definition to assign temperatures to the composite slab - thick portions of the south slab.

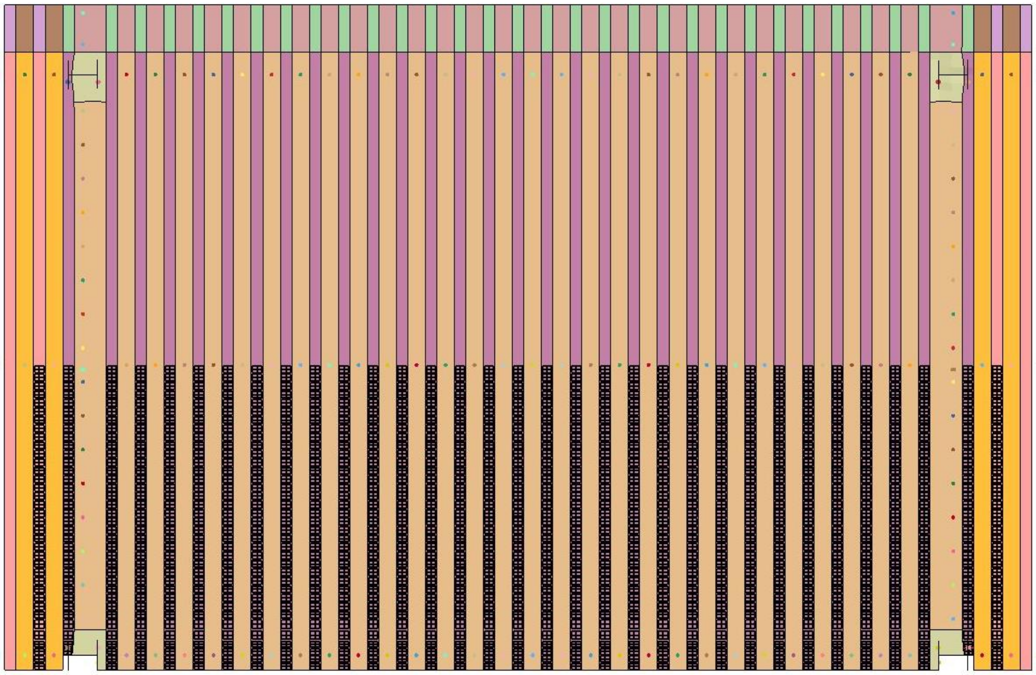

Fig. 77. Node set definition to assign temperatures to the composite slab - thin portions of the south slab.

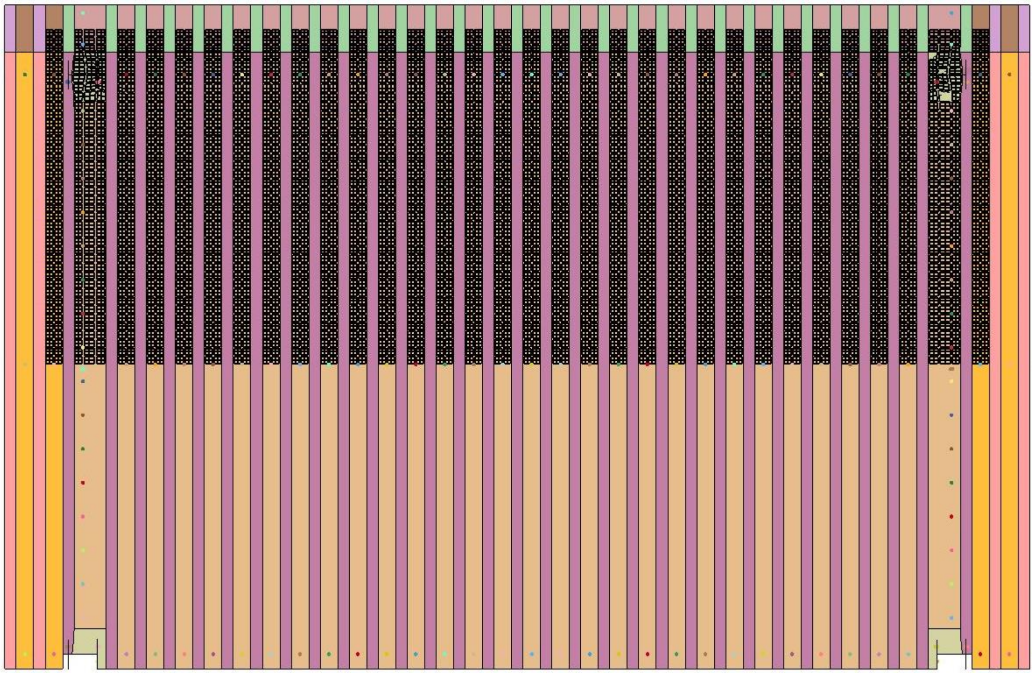

Fig. 78. Node set definition to assign temperatures to the composite slab - thick portions of the north slab.

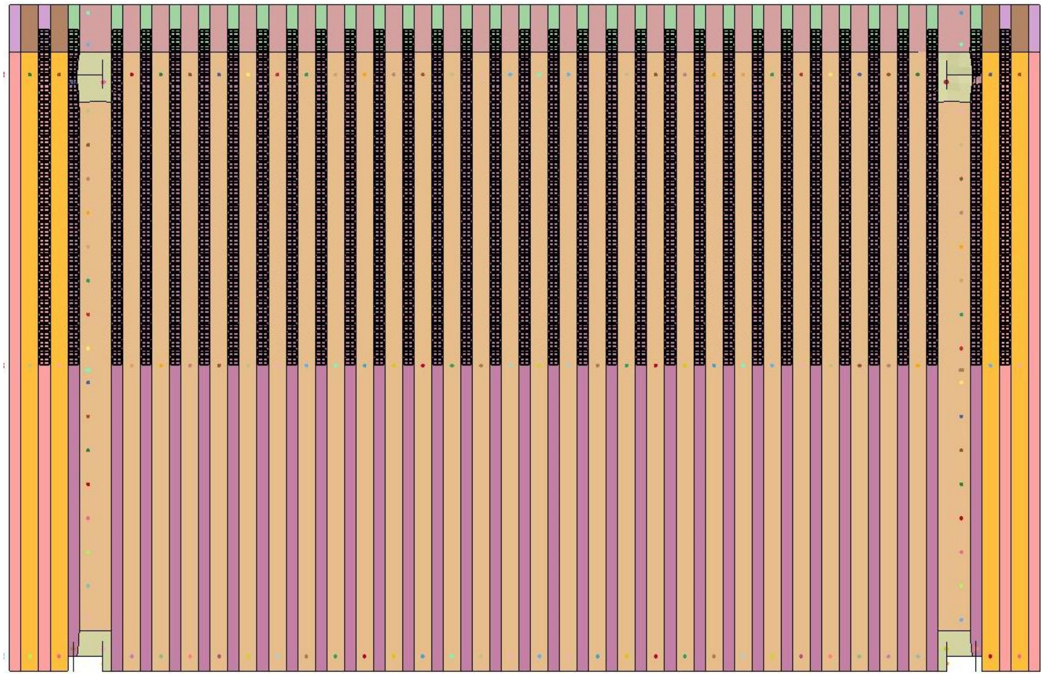

Fig. 79. Node set definition to assign temperatures to the composite slab - thin portions of the north slab.

4. Computational Model: Results and Validation

The modeling approach described in the previous chapter was validated against experimental data from the NIST NFRL CF 2 full-scale test on a composite concrete-steel deck floor system in a two-bay by three-bay, two-story steel framed building subjected to a compartment fire (refer to Chapter 2 for details of the NIST NFRL CF 2 Test). The model validation is illustrated and discussed in this chapter. Specifically, to examine the capabilities of the model, representative results and observations from the computational model, in terms of structural deformation and failure modes, are compared against corresponding results and observations from the experiment.

4.1. Basis for Validation

To validate the model, the following results (representative of the structural response of the composite floor system under fire exposure) from the analysis and the experiment were compared:

i. Displacements, including vertical displacements of the composite slab of the fire-tested floor, vertical and horizontal (lateral) displacements of the supporting steel beams, and horizontal (lateral) displacements of steel columns of both the fire-tested floor and the surrounding floors

ii. Observed and predicted deformation-related behaviors and potential failure modes of different components of the composite floor system, including bolted connections, beams, and composite slab

iii. Strains measured for beams of the surrounding floors, and columns of both the fire-tested and the surrounding floors

To facilitate the discussions and comparisons, a nomenclature was used to refer to different members of the composite floor system. This nomenclature is shown in Fig. 80. As indicated in Fig. 80, the three beams of the fire-tested floor are distinguished as the south, middle, and north W16×31 beams; the two girders are distinguished as the east and west W18×35 girders; the four columns are designated as southeast, southwest, northeast, and northwest columns; the upper and lower portions of the composite slab are referred to as north and south slab, respectively.

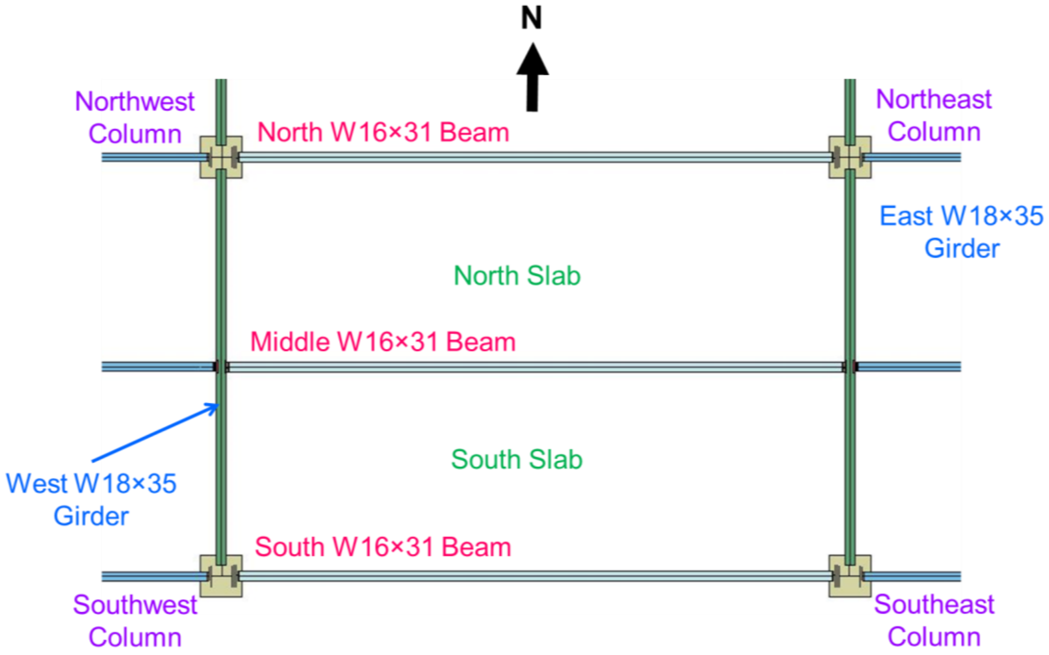

Fig. 80. Nomenclature for different members of the fire-tested composite floor.

It is important to note that results and observations from the fire experiment correspond to a temperature-time exposure that includes the uncontrolled cooling stage following a halt in the fire application, while observations from the computational model are based on a temperature-time exposure that only includes heating stage to the maximum gas temperature in the fire compartment under the tested floor. The computational model failed to converge for the bottom bolts of the extended shear tab connections at the south ends of the east and west W18×35 girders. This happened close to the maximum fire temperature point in the CF2 Test that occurred at around 130 minutes through the fire exposures. Therefore, the simulation did not consider the cooling phase of the fire in the CF2 Test.

To put observations and discussions in perspective, the state of temperature for steel components of the composite steel-framed structure when exposed to the maximum fire temperature is shown in Fig. 81. As observed in Fig. 81, only the members in the test bay were at elevated temperatures. The rest of the frame was at ambient temperature. Further, the maximum steel temperature of about 915 °C was observed at the web of the middle W16×31 beam. As can also be seen in Fig. 81, the connection temperatures were significantly lower than those of the beams and girders.

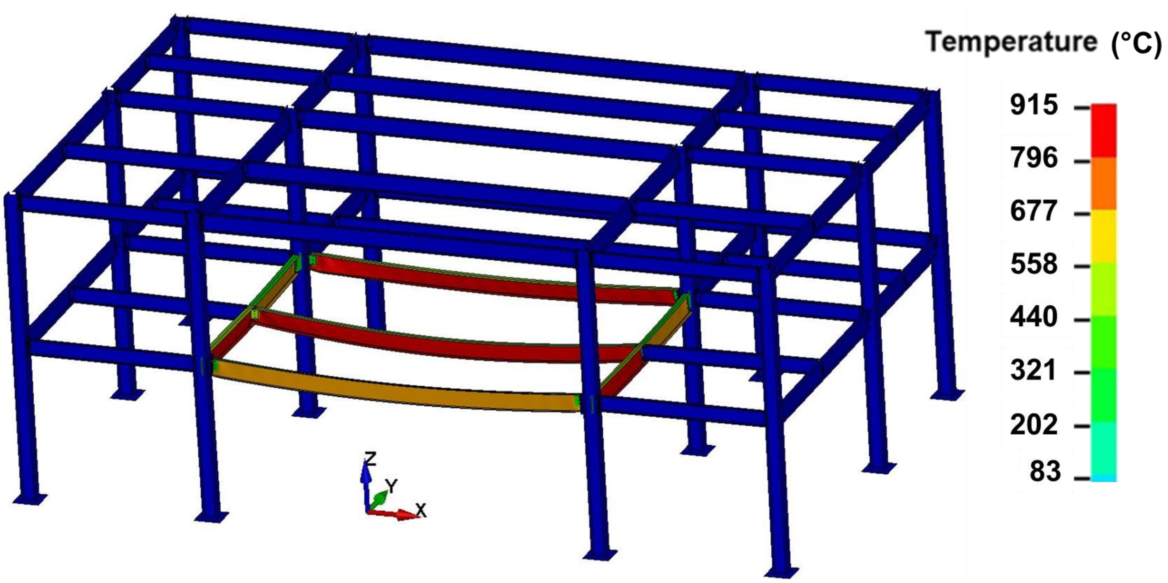

Fig. 81. A contour plot for steel temperatures corresponding to the maximum fire temperature.

4.1.1. Displacements

During the experiment, vertical and horizontal displacements were measured at different locations for both the steel frame components and the fire-tested composite floor. Figures 82 and 83 show the locations of the vertical and horizontal displacement measurements across the test floor assembly, respectively.

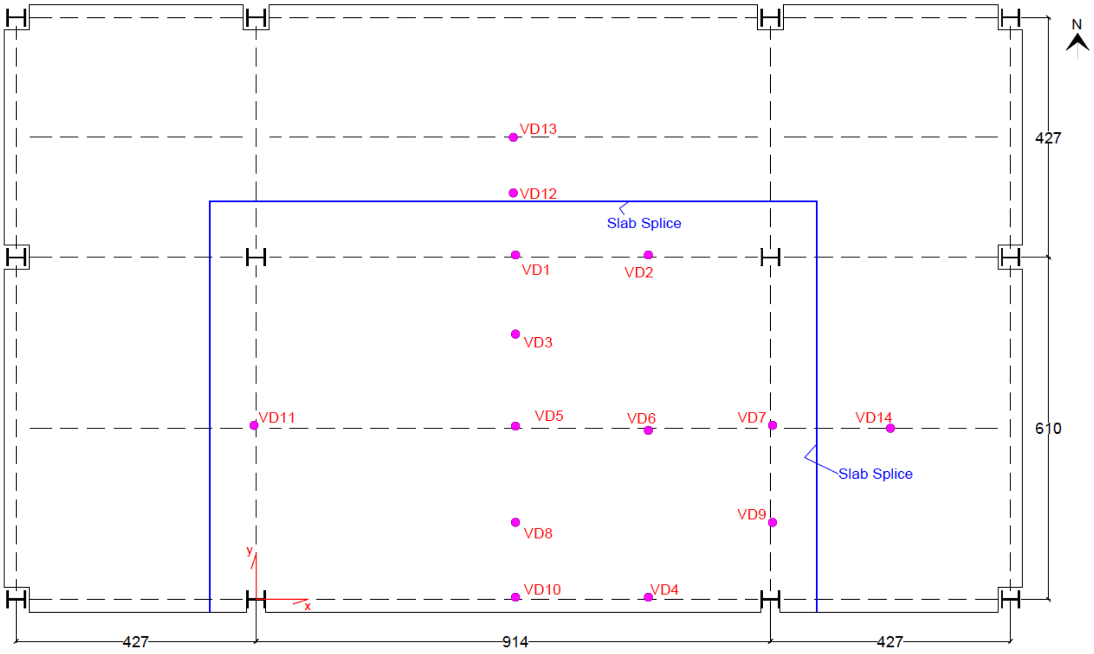

Fig. 82. Location of the vertical displacement (VD) measurements in the NIST NFRL CF2 Test [Choe et al. 2022].

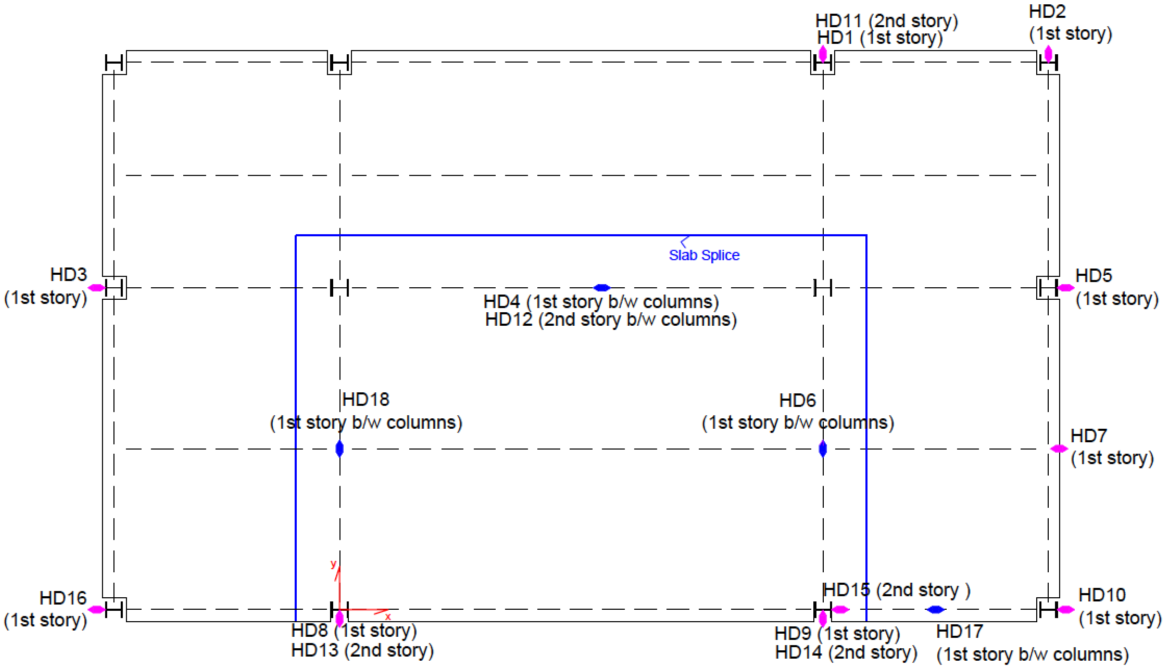

Fig. 83. Location of the horizontal displacement (HD) measurements in the NIST NFRL CF2 Test [Choe et al. 2022].

An overall view of displacements predicted in the analysis is presented in Fig. 84, where the calculated deformed shape of the composite steel-framed building at the state of maximum fire temperature is shown. Figures 85, 86, and 87 further show, respectively, the contours for the X- (horizontal), Y- (horizontal), and Z- (vertical) components of displacement for the steel frame at the state of maximum fire temperature. In addition, vertical displacements of the fire-tested composite floor slab at the maximum fire temperature are shown as a contour plot in Fig. 88.

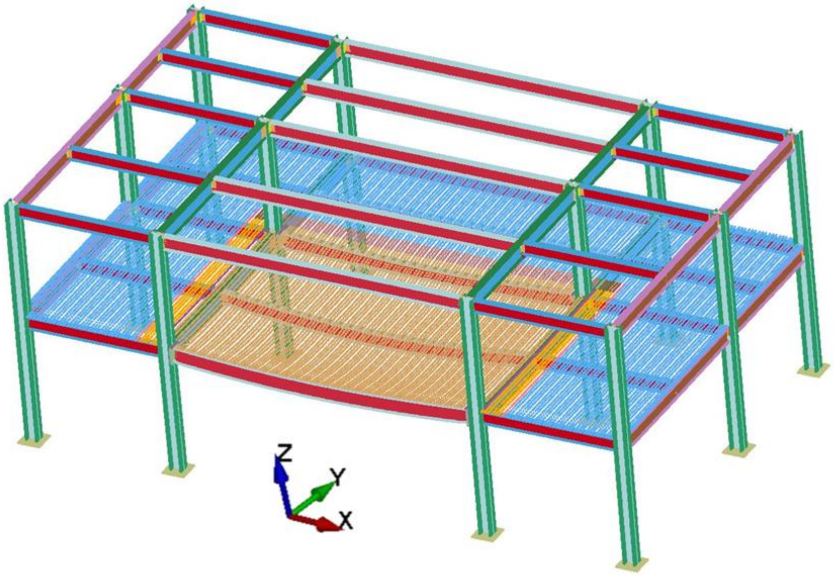

Fig. 84. Deformed shape of the composite steel-framed structure following fire simulation in LS-DYNA (corresponding to the maximum fire temperature).

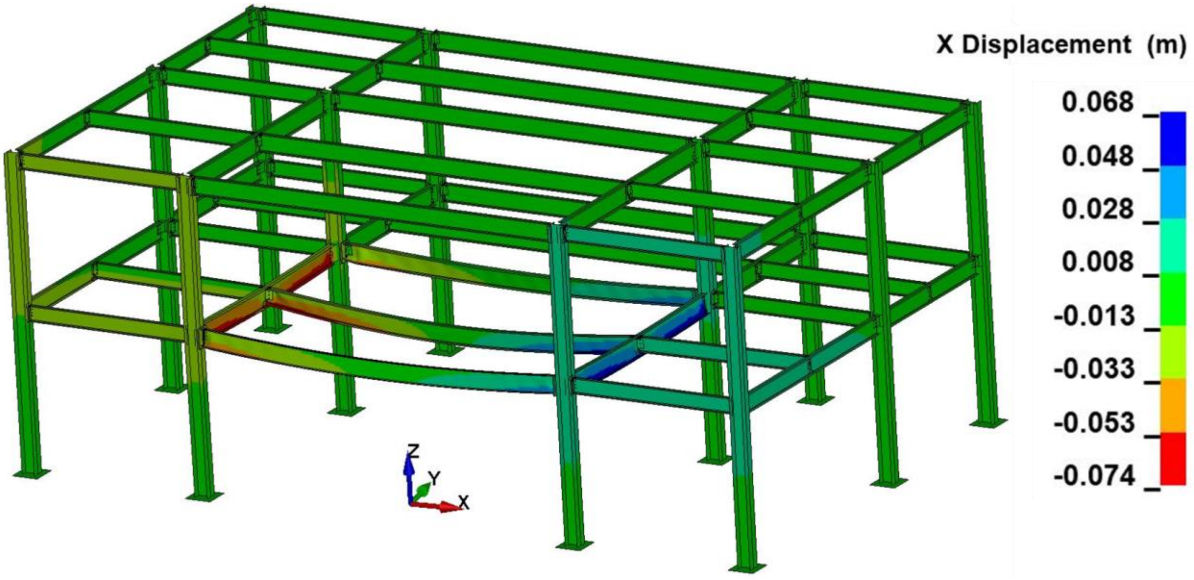

Fig. 85. A displacement contour plot for the steel frame at the peak fire temperature - horizontal X direction.

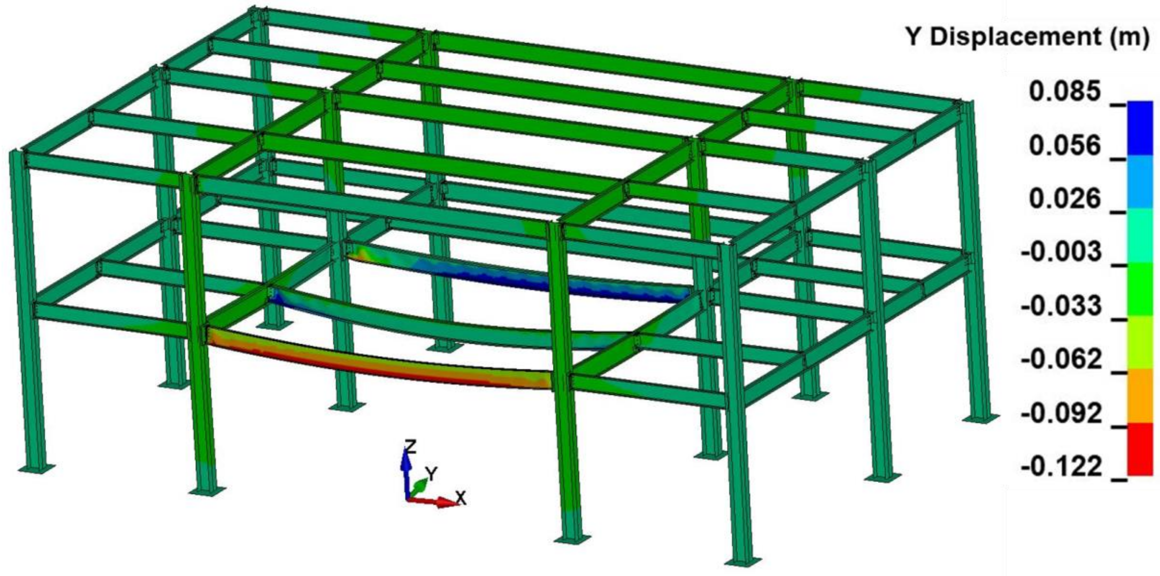

Fig. 86. A displacement contour plot for the steel frame at the peak fire temperature - horizontal Y direction.

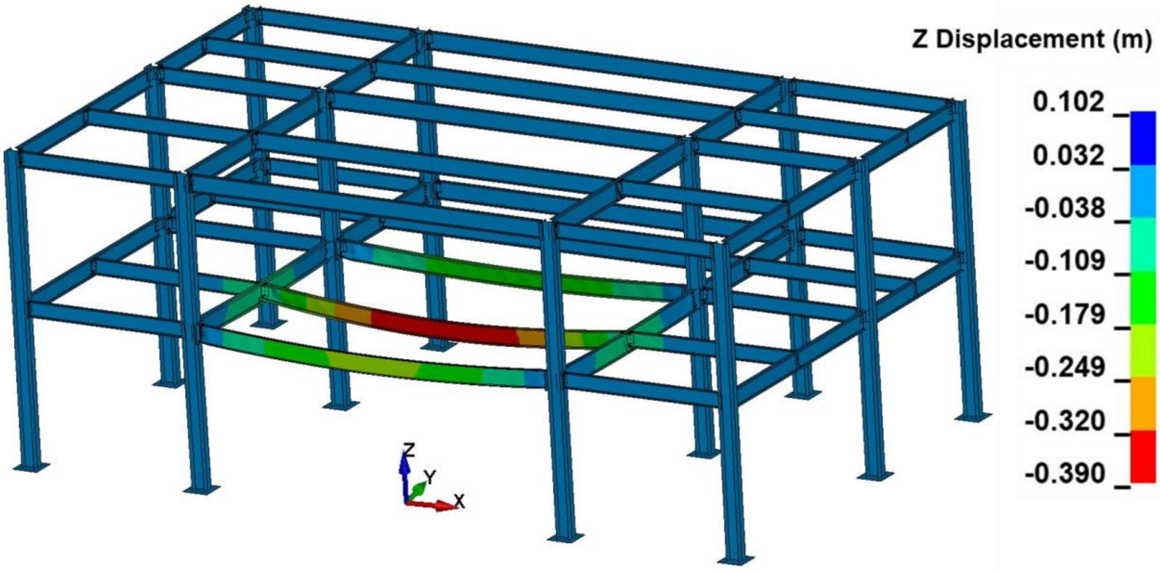

Fig. 87. A displacement contour plot for the steel frame at the peak fire temperature - vertical Z direction.

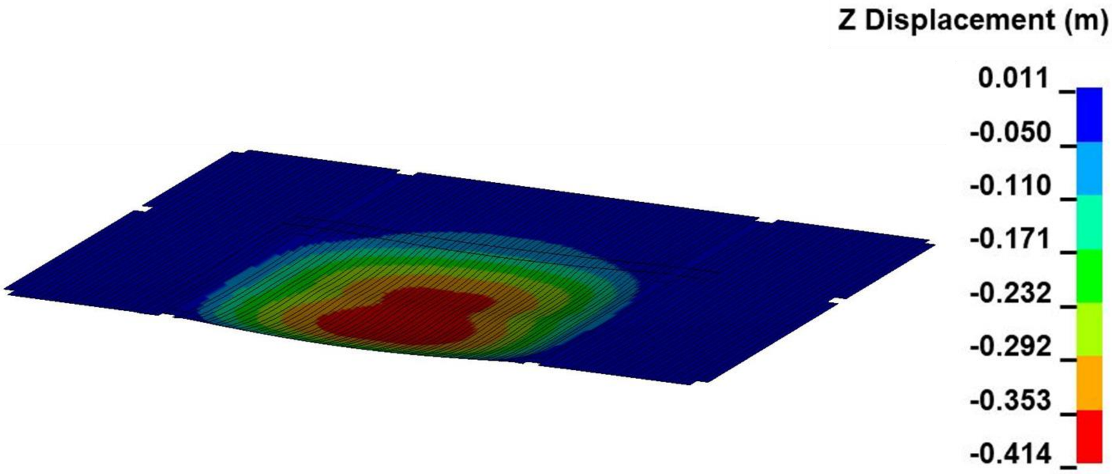

Fig. 88. A contour plot for slab vertical displacements following fire simulation in LS-DYNA (corresponding to the maximum fire temperature).

Several important observations can be made from the displacement contours presented in Figs. 85 to 88. First, Fig. 85 indicates that significant lateral displacements occurred for the lower flanges of both east and west W18×35 girders. The main drivers of out-of-plane lateral movement of the W18×35 girders were the axial displacements of the W16×31 beams (seen also in Fig. 85) due to thermal expansion. Second, lateral displacement of the lower flanges of the W16×31 beams can be observed in Fig. 86. The lateral displacements of the W16×31 beams were mainly caused by the restraint to thermal expansion from W18×35 girders, the composite slab, and the components of the steel frame outside of the test bay. These lateral displacements are more significant for the south W16×31 beam since the upper flange of this beam was only supported by the composite slab from one side. Further, Fig. 87 shows that the middle W16×31 beam experienced larger vertical displacements than the south and north beams. This is due to the higher temperature of and higher load demand on the middle beam in the test bay. Finally, Figs. 87 and 88 indicate that the composite slab resisted larger vertical displacements than those of the W16×31 beams in the fire test bay. As will be illustrated in Section 4.1.2, the observations from Figs. 85 to 88 are consistent with observations from the experiment.

The following sections provide details on the validation of the model in predicting displacements recorded during the test at different locations shown in Figs. 82 and 83. Specifically, vertical displacement of the fire-tested slab, vertical displacement of the supporting beams and girders of the fire-test bay, and horizontal displacement of the columns predicted from the simulation and measured in the test were compared.

4.1.1.1. Slab Displacements

To validate the capability of the model to capture slab displacements recorded during the test, displacements predicted from the analysis and measured in the test were compared at locations VD3 and VD8 shown in Fig. 82. Additionally, the accuracy of the model predictions was quantified as the percentage error in the difference between the predicted and measured slab displacements corresponding to the maximum fire temperature, representing the most extreme fire exposure for the system. It should also be noted that, in the CF2 Test, the actuator loading was maintained 2-hours into the cooling that resulted in continued increase of the slab vertical displacement beyond the 131 minutes of fire exposure.

Predicted and measured vertical displacements at the center of the north slab of the fire-tested floor (location VD3) are shown in Fig. 89. Note that the negative values for VD3 displacements indicate the downward vertical movement (in the -Z Direction) of the north slab of the fire-tested floor. As can be observed from Fig. 89, the largest discrepancy between the experimental and the simulated VD3 displacements occurred at the beginning of the fire test. Despite of this discrepancy and differences in displacement rate predictions, good agreements are observed between simulated and measured VD3 displacements. Specifically, the percent deviation between the experimental and computational VD3 displacements corresponding to the maximum fire temperature was about 0.3 %. Moreover, the maximum downward deflection of the center of north slab was about 350 mm (13.8 in.) at the maximum fire temperature.

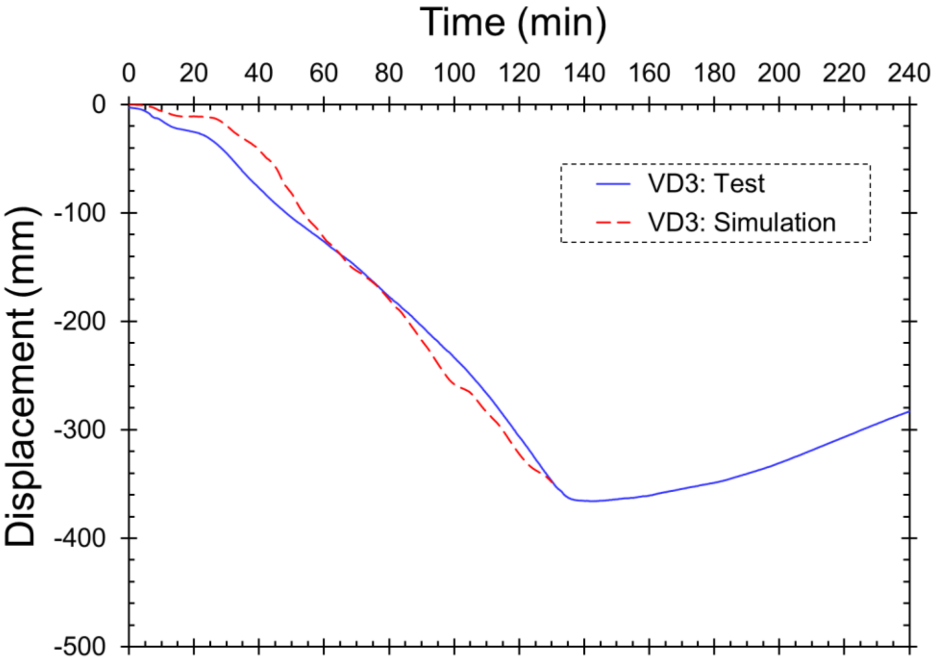

Fig. 89. Simulated and measured vertical displacement histories at the center of north slab (location VD3 in Fig. 82).

Figure 90 further compares the predicted and measured vertical displacements at the center of south slab of the fire-tested floor (location VD8). The negative values for VD8 displacements indicate the downward vertical movement (in the -Z Direction) of the south slab of the fire-tested floor. As can be observed from Fig. 90, the largest discrepancy between the experimental and the simulated VD8 displacements occurred at the beginning of the fire test. Despite of this discrepancy and differences in displacement rate predictions, good agreements are observed between simulated and measured VD8 displacements. Specifically, the percent deviation between the experimental and computational VD8 displacements corresponding to the maximum fire temperature was about 7 %. Moreover, the maximum downward deflection of the center of south slab was predicted at about 414 mm (16.3 in.) at the maximum fire temperature. Therefore, compared to the north slab, the south slab of the fire-tested floor experienced larger deflections.

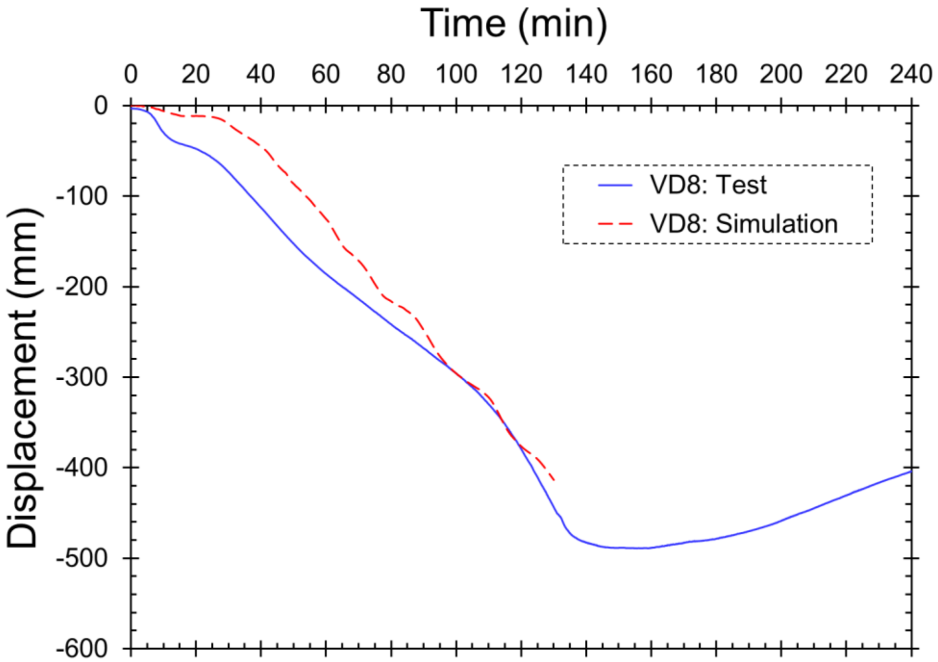

Fig. 90. Simulated and measured vertical displacement histories at the center of south slab (location VD8 in Fig. 82).

4.1.1.2. Beam and Girder Displacements

The modeling approach was also validated against measured displacements for the supporting beams and girders in the fire-tested slab. Specifically, measured vertical displacements at the midspan of the north, middle, and south W16×31 beams, and at the midspan of the east and west W18×35 girders were used in the model validation (refer to Fig. 80 for the location of these beams and girders). These are, respectively, locations VD1, VD5, VD10, VD7, and VD11 in Fig. 82. The accuracy of the model predictions was quantified as the percentage error in the difference between the predicted and measured beam and girder vertical displacements corresponding to the maximum fire temperature, representing the most extreme fire exposure for the system. It should also be noted that, in the CF2 Test, the actuator loading was maintained 2-

hours into the cooling that resulted in continued increase in the vertical displacement of the beams and girders beyond the 131 minutes of fire exposure.

Predicted and measured vertical displacements at the midspan of the north, middle, and south W16×31 beams of the fire-tested floor (locations VD1, VD5, and VD10 in Fig. 82) are shown in Figs. 91, 92, and 93, respectively. Note that the negative values for VD1, VD5, and VD10 displacements indicate the downward deflection (in the -Z Direction) of the supporting beams of the fire-tested floor. Note that the deflections measured for the south W16×31 beam (VD10 displacements in Fig. 93) became invalid at around 130 minutes of fire exposure (as indicated in the test report [Choe et al. 2022]). As a result, no experimental data were recorded for VD10 displacements (Fig. 93) beyond the maximum fire temperature. The percent deviations between the experimental and computational VD1, VD5, and VD10 displacements corresponding to the maximum fire temperature were about 12 %, 0.4 %, and 0.1 %, respectively. As further can be seen in Figs. 91, 92, and 93, the middle W16×31 beam experienced larger deflections compared to the north and south W16×31 beams. The maximum downward deflections predicted for the north, middle, and south W16×31 beams were about, respectively, 171 mm, 390 mm, and 211 mm (6.7 in., 15.3 in., and 8.3 in.) at the maximum fire temperature.

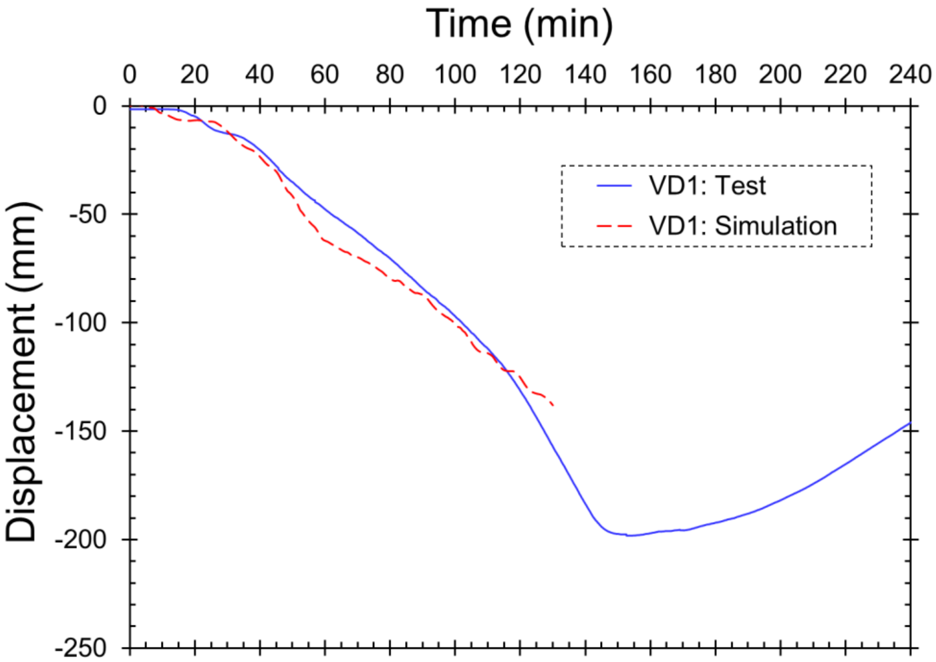

Fig. 91. Simulated and measured vertical displacement histories at the midspan of the north W16×31 beam (location VD1 in Fig. 82).

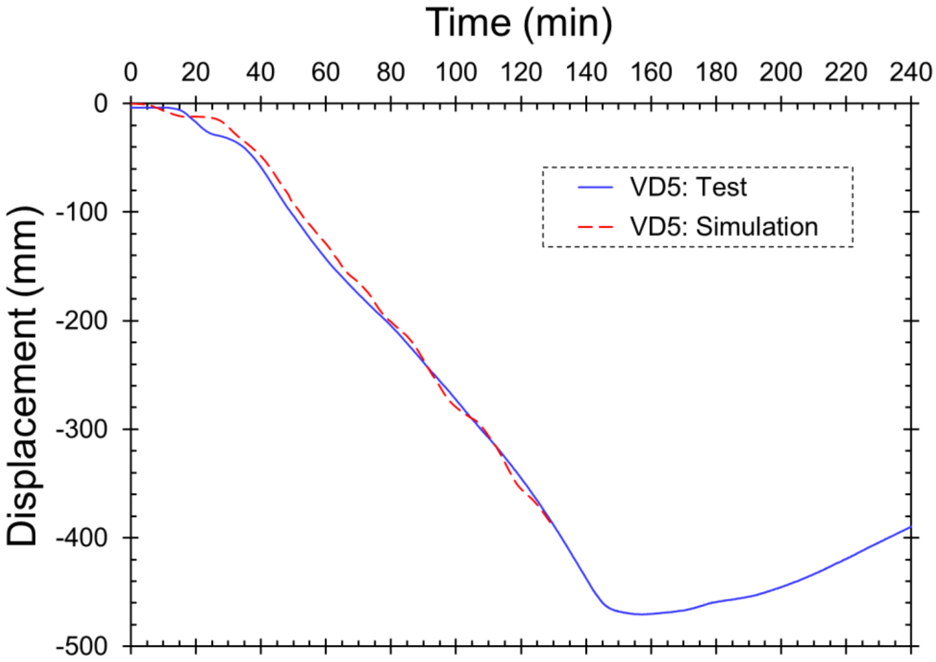

Fig. 92. Simulated and measured vertical displacement histories at the midspan of the middle W16×31 beam (location VD5 in Fig. 82).

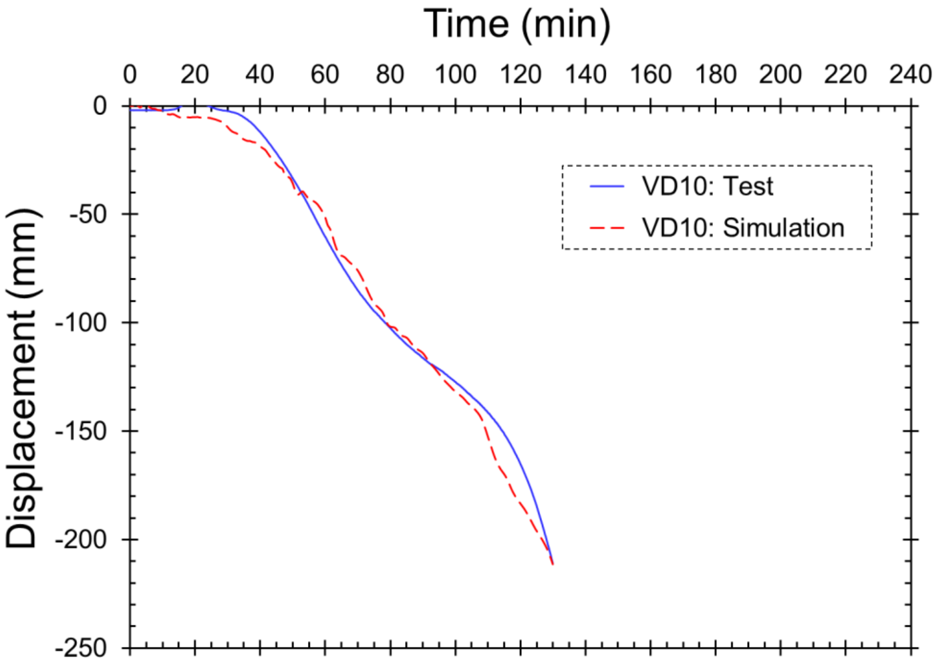

Fig. 93. Simulated and measured vertical displacement histories at the midspan of the south W16×31 beam (location VD10 in Fig. 82).

Figures 94 and 95 represent predicted and measured vertical displacements at the midspan of the east and west W18×35 girders of the fire-tested floor (locations VD7 and VD11 in Fig. 82), respectively. Note that the negative values for VD7 and VD11 displacements indicate the downward deflection (in the -Z Direction) of the supporting girders of the fire-tested floor. It can be seen from Figs. 94 and 95 that the differences between the predicted and measured displacements started after about 50 minutes of fire exposure, with a maximum discrepancy of about 37 % and 44 % at the maximum fire temperature for the east and west W18×35 girders, respectively. The reasons for these discrepancies are further discussed in the following paragraphs.

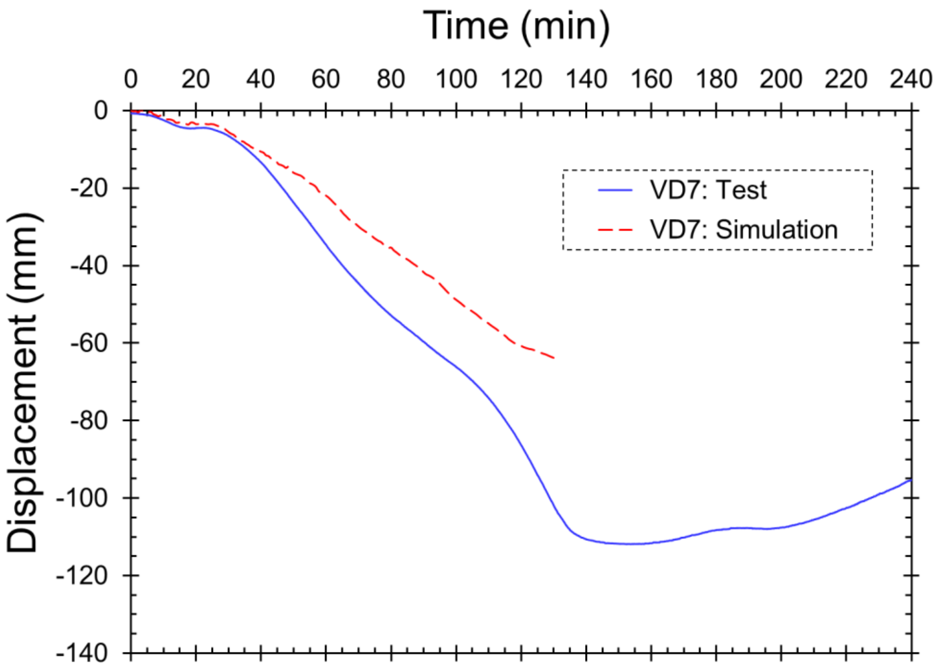

Fig. 94. Simulated and measured vertical displacement histories at the midspan of the east W18×35 girder (location VD7 in Fig. 82).

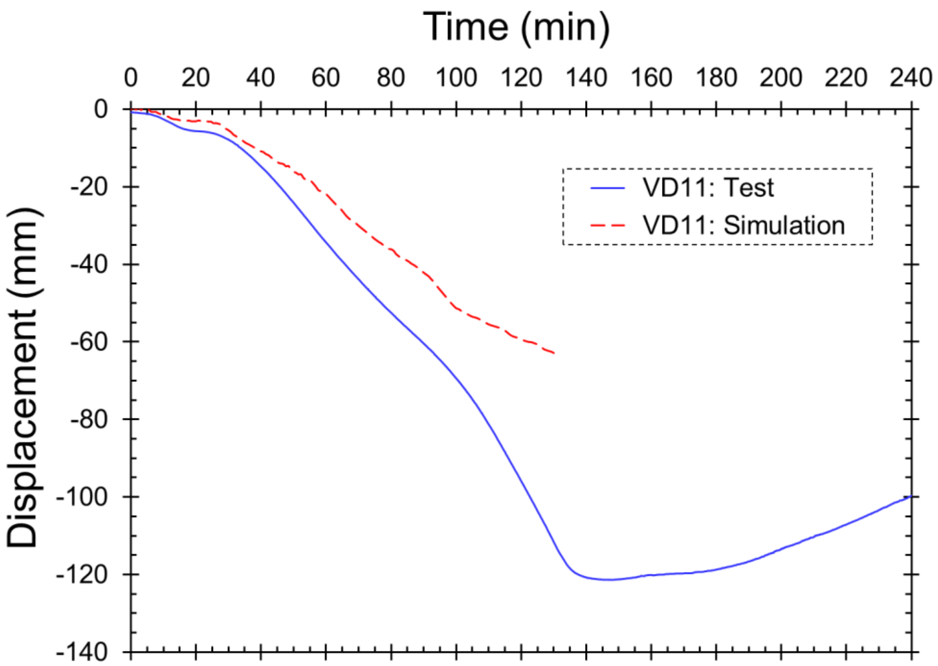

Fig. 95. Simulated and measured vertical displacement histories at the midspan of the west W18×35 girder (location VD11 in Fig. 82).

As observed in Figs. 91, 92, 93, 94 and 95, the discrepancies between measured and simulated vertical displacement histories were more significant for girders than for beams. To provide some context as to what caused the observed differences, the simulated and measured vertical displacement at the midspan of the east and west W18×35 girders as a function of bottom flange temperature are plotted and compared in Figs. 96 and 97, respectively. As seen in Figs. 96 and 97, when plotted as a function of bottom flange temperature, better agreements are observed between the predicted and measured displacements. Specifically, percent deviations between the experimental and computational VD7, and VD11 displacements corresponding to the maximum fire temperature were about 0.1 %, and 14.0 %, respectively.

The closer agreement of measured and simulated vertical displacement at the midspan of the east and west W18×35 girders, presented in Figs. 96 and 97 as compared to the ones shown in Figs. 94 and 95, is an indication of possible impact from thermal creep of steel, which is not explicitly considered in the simulation of the CF2 Test. More specifically, ignoring the explicit inclusion of creep in the mechanical model of the ASTM A992 steel at elevated temperatures resulted in a better agreement of simulated and measured displacements at a specific temperature rather than at a specific time during the fire exposure. Further, when compared at specific times, the simulated vertical displacements follow experimental values closer for the W16×31 beams than for the W18×35 girders (as seen in Figs. 91 to 95). This observation along with the observation that the behavior of W16×31 beams in the CF2 Test is governed by catenary action (refer to Section 5.1) rather than by flexure (the governing behavior for W18×35 girders) may suggest that the thermal creep of steel does not have significant impact on large deflections of axially restrained beams with catenary action.

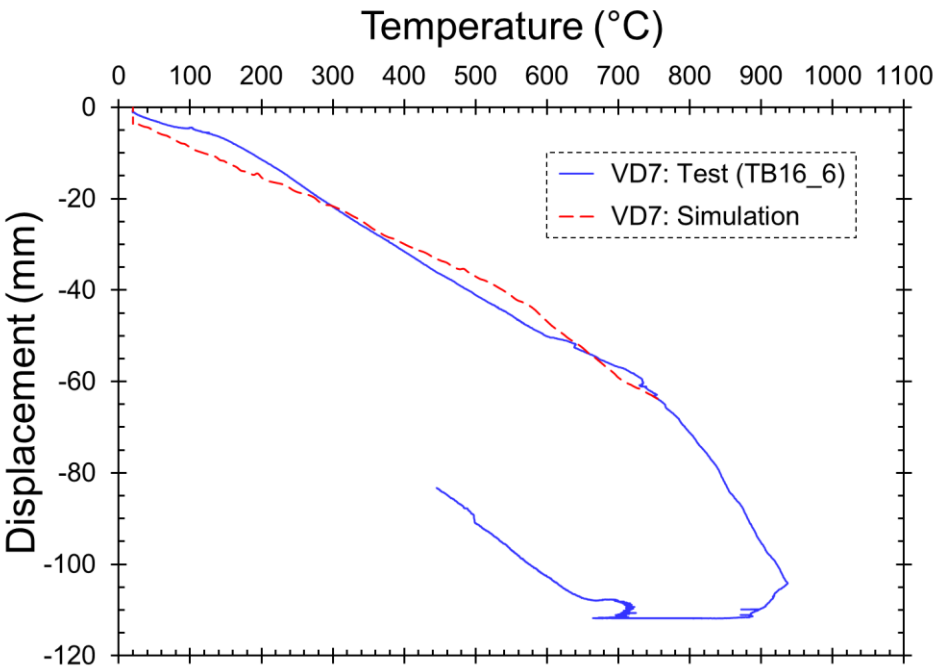

Fig. 96. Simulated and measured vertical displacement as a function of bottom flange temperature at the midspan of the east W18×35 girder (location VD7 in Fig. 82, and TB16-6 in Fig. 49).

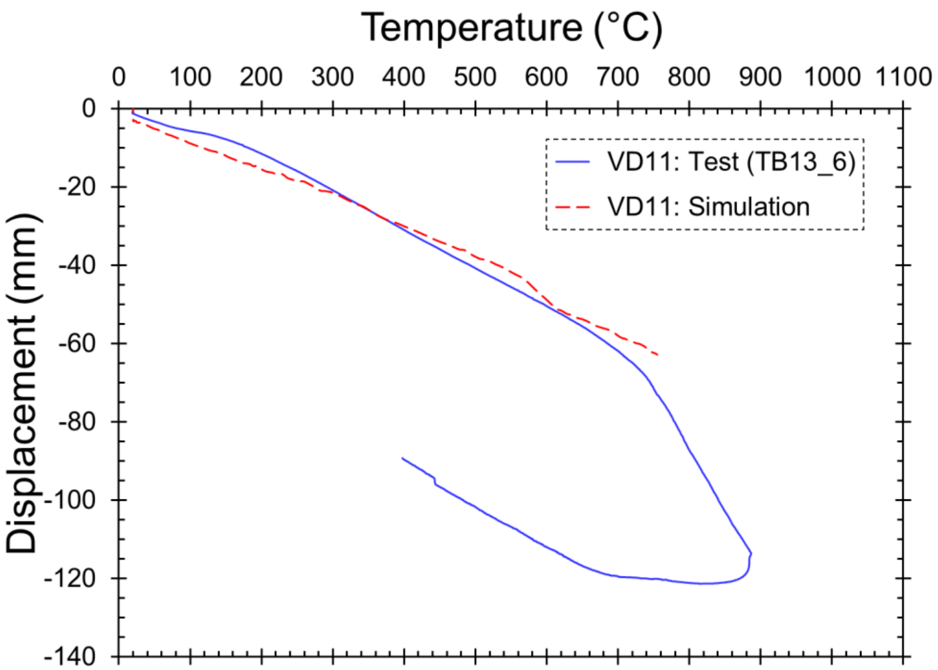

Fig. 97. Simulated and measured vertical displacement as a function of bottom flange temperature at the midspan of the west W18×35 girder (location VD11 in Fig. 82, and TB13-6 in Fig. 49).

The modeling approach was further validated against measured horizontal displacements (expansions) of the east, west, and north edges of the fire-tested slab (measurements at HD6, HD18, and HD4 locations in Fig. 83, respectively). The accuracy of the model predictions was quantified as the percentage error in the difference between the predicted and measured horizontal displacements (expansions) corresponding to the maximum fire temperature.

Calculated and measured horizontal displacements (expansions) of the east and west edges of the fire-tested floor (locations HD6 and HD18 in Fig. 83) are shown in Figs. 98 and 99, respectively. Note that the negative values for HD6 and HD18 displacements indicate the southward expansion (in the -Y Direction) of the east and west edges of the fire-tested floor. This is expected since there is less restraint to the thermal expansion of the fire-tested floor slab on its south edge. Further, good agreements are observed between simulated and measured HD6 and HD18 displacements in Figs. 98 and 99. Specifically, the percent deviation between the experimental and computational HD6 and HD18 displacements corresponding to the maximum fire temperature was about 0.4 % and 0.3 %, respectively. Moreover, the maximum expansions calculated for the east and west edges of the fire-tested floor slab were about 28 mm and 24 mm (1.1 in. and 0.9 in.) at the maximum fire temperature, respectively.

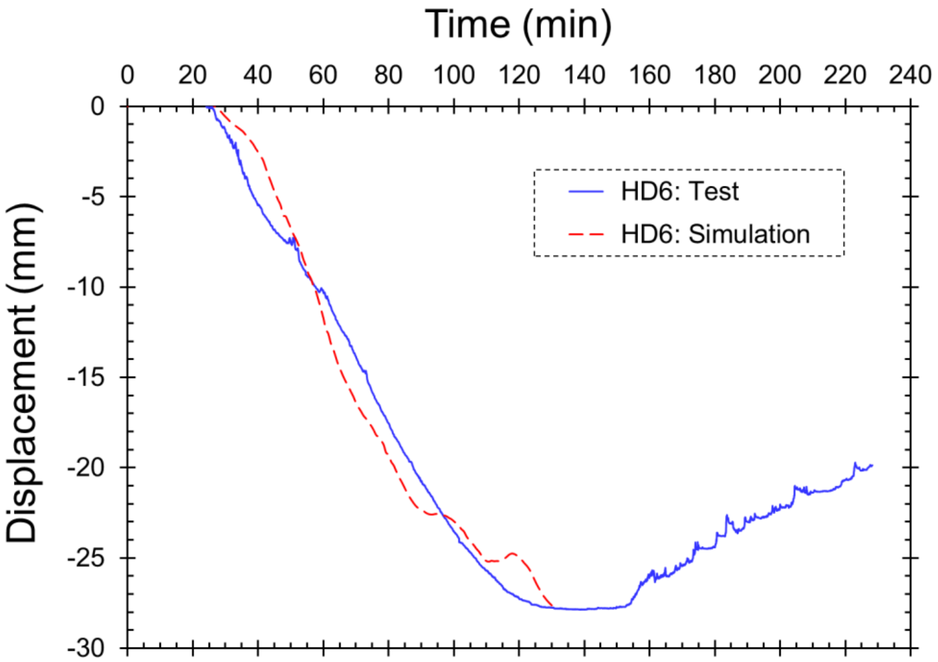

Fig. 98. Simulated and measured displacement histories for the thermal elongation of the east side of the fire-tested floor slab (location HD6 in Fig. 83).

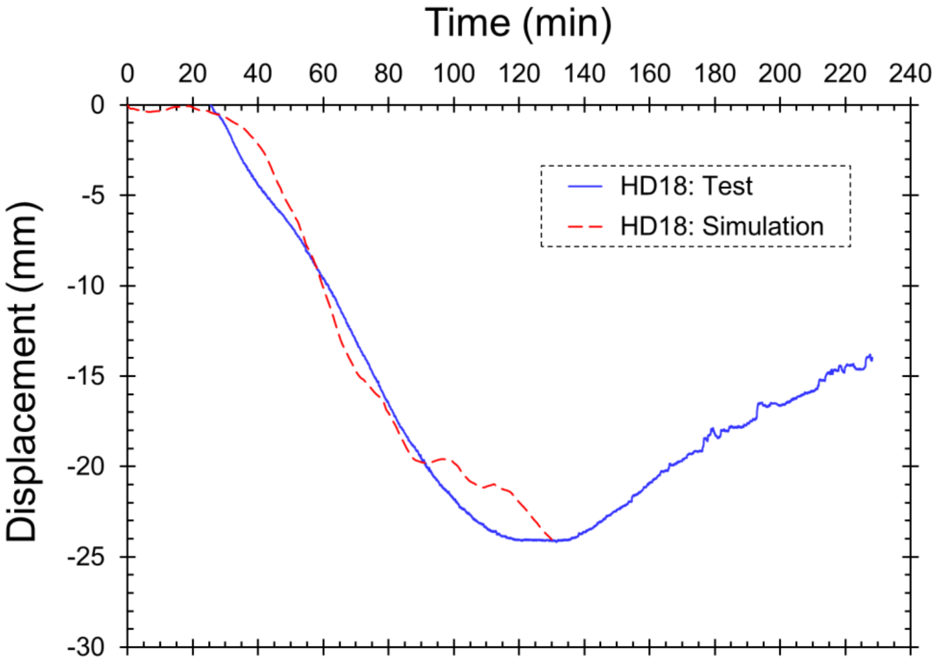

Fig. 99. Simulated and measured displacement histories for the thermal elongation of the west side of the fire-tested floor slab (location HD18 in Fig. 83).

Calculated and measured horizontal displacements (expansions) of the north edge of the fire-tested floor (locations HD4 in Fig. 83) are shown in Fig. 100. The negative values for HD4 displacements indicate the westward expansion (in the -X Direction) of the north edge of the fire-tested floor slab. Further, good agreements are observed between simulated and measured HD4 displacements in Fig. 100. Specifically, the percent deviation between the experimental and computational HD4 displacements corresponding to the maximum fire temperature was about 0.1 %. Moreover, the maximum expansions calculated for the north edge of the fire-tested floor slab was about 16 mm (0.63 in.) at the maximum fire temperature.

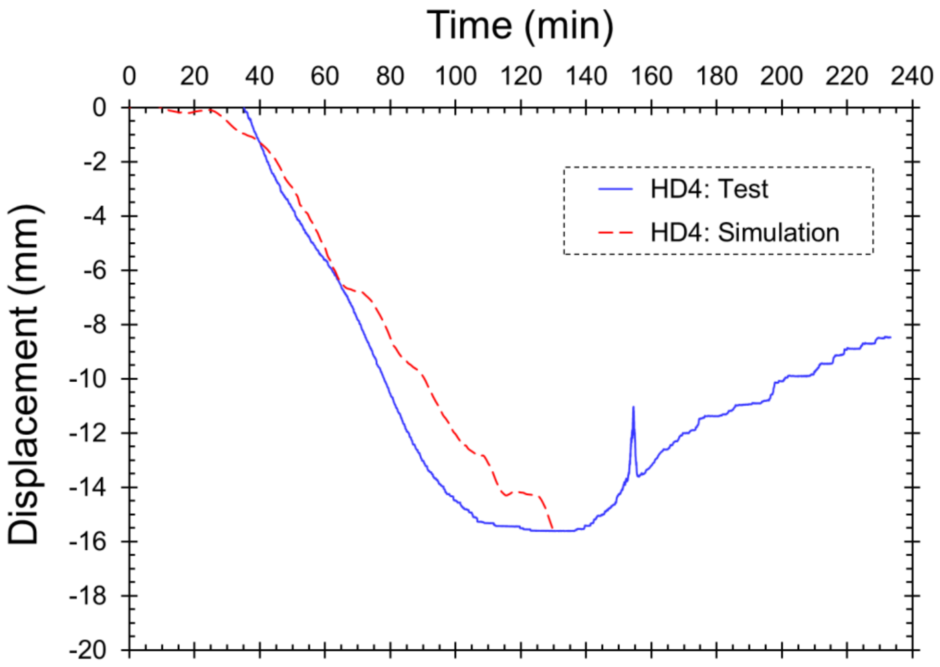

Fig. 100. Simulated and measured displacement histories for the thermal elongation of the north side of the fire-tested floor slab (location HD4 in Fig. 83).

4.1.1.3. Column Displacements

The validation of the model was further conducted using the data collected for horizontal (lateral) displacements of the first-story columns at different locations in the NIST NFRL CF2 Test. The data include the horizontal displacements of the southeast and southwest columns of the fire-tested floor (locations HD9 and HD8 in Fig. 83, respectively) in the north-south direction

(Y Direction). The data also include horizontal displacements of the perimeter columns outside of the fire-tested bay. Specifically, the data on the horizontal column displacements HD16, HD10, HD3, and HD5 (locations shown in Fig. 83) in the east-west direction (X Direction), and the horizontal column displacements HD1 and HD2 (locations shown in Fig. 83) in the north-south direction (Y Direction). The accuracy of the model predictions was quantified as the percentage error in the difference between the predicted and measured horizontal (lateral) column displacements at the maximum fire temperature, representing the most extreme fire exposure for the system.

Figures 101 and 102 compare calculated and measured horizontal displacements of the southeast and southwest columns of the fire-tested floor (locations HD9 and HD8 in Fig. 83), respectively. The negative values for HD9 and HD8 displacements indicate the southward lateral deflection (in the -Y Direction) of the southeast and southwest columns of the fire-tested floor as a result of thermal expansion of the fire-tested floor slab. It can also be seen from Figs. 101 and 102 that the largest discrepancy between the experimental and the simulated HD9 and HD8 displacements occurred at the beginning of the fire test. Despite this discrepancy and differences in displacement rate predictions, good agreements are observed between simulated and measured HD9 and HD8 displacements. Specifically, the percent deviation between the experimental and computational HD9 and HD8 displacements corresponding to the maximum fire temperature was about 0.9 % and 1.0 % for the southeast and southwest columns of the fire-tested floor, respectively. Moreover, the maximum horizontal displacements calculated for the southeast and southwest columns of the fire-tested floor were about 30 mm, and 28 mm (1.2 in. and 1.1 in.) at the maximum fire temperature, respectively.

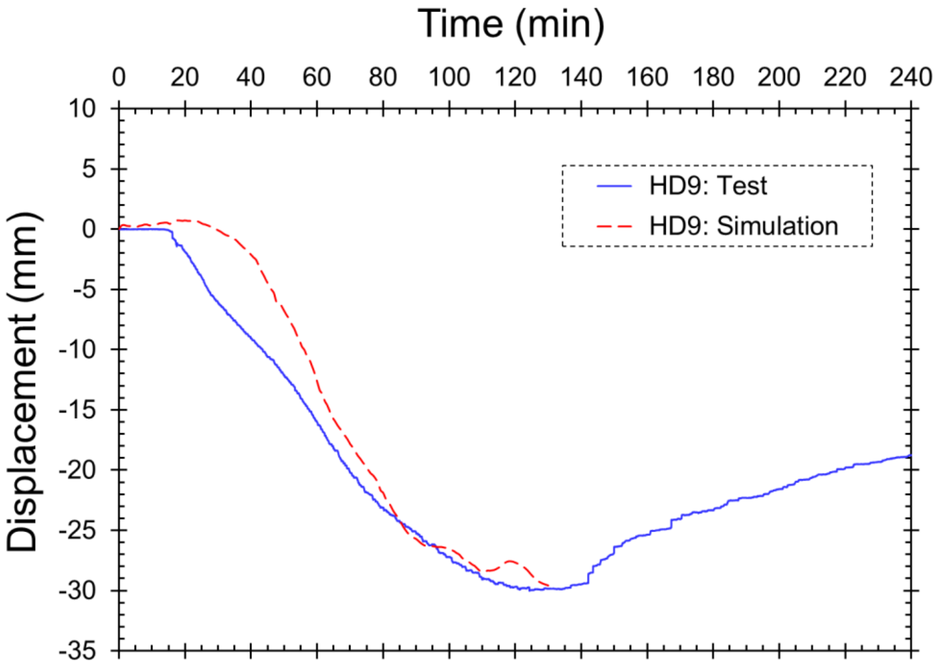

Fig. 101. Simulated and measured horizontal displacement histories for the southeast column at the first story level (location HD9 in Fig. 83).

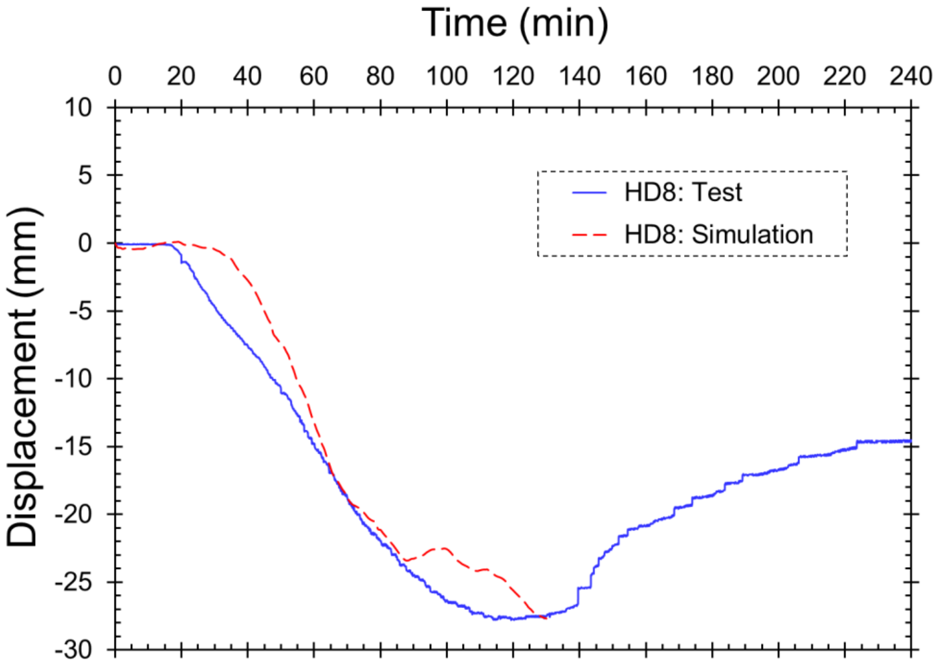

Fig. 102. Simulated and measured horizontal displacement histories for the southwest column at the first story level (location HD8 in Fig. 83).

Figures 103, 104, 105, and 106 compare calculated and measured horizontal displacements in the east-west direction (X Direction) for the perimeter columns outside of the fire-tested bay (locations HD16, HD10, HD3, and HD5 in Fig. 83). The negative values for HD16 and HD3 displacements indicate the westward lateral deflection (in the -X Direction), and the positive values for HD10 and HD5 displacements indicate the eastward lateral deflection (in the X Direction) of the perimeter columns outside of the fire-tested bay due to the thermal expansion of the fire-tested floor slab. Despite discrepancies and differences in displacement rate predictions seen in Figs. 103, 104, 105, and 106, the general shape of displacement-time curves from the analysis and experiment agree reasonably well. Specifically, the percent deviation between the experimental and computational HD16, HD10, HD3, and HD5 displacements corresponding to the maximum fire temperate were about 1.1 %, 0.1 %, 3.6 %, and 28.7 % for the perimeter columns outside of the fire-tested bay, respectively.

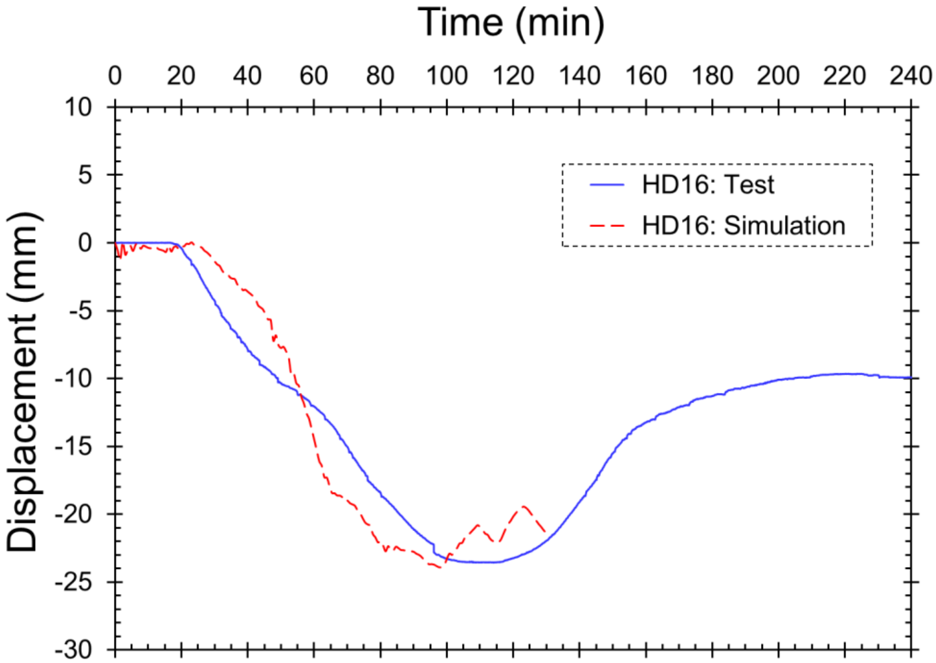

Fig. 103. Simulated and measured horizontal displacement histories for the first-story column west of the southwest column of the fire-test bay (location HD16 in Fig. 83).

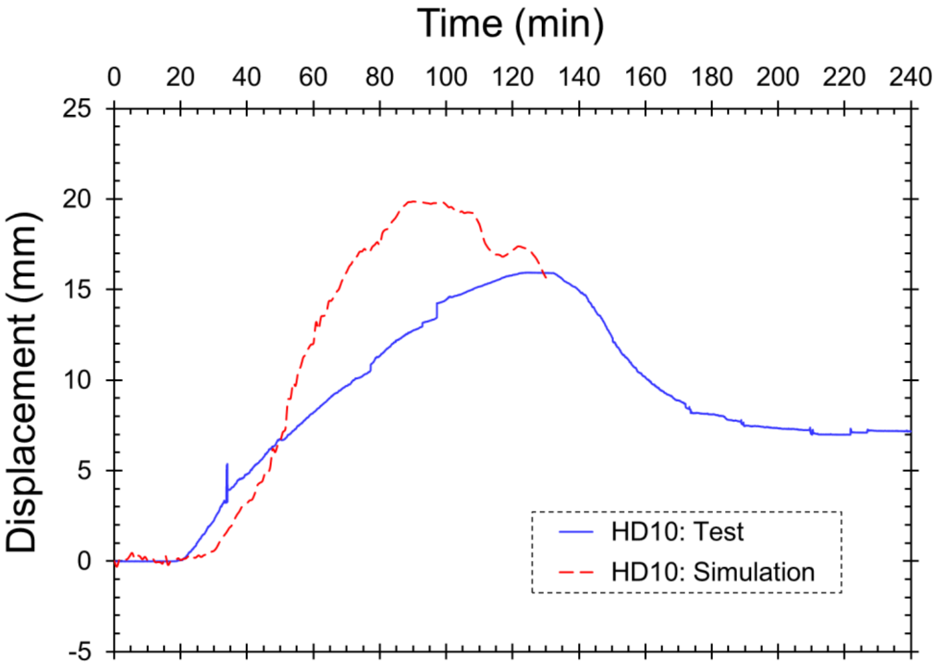

Fig. 104. Simulated and measured horizontal displacement histories for the first-story column east of the southeast column of the fire-test bay (location HD10 in Fig. 83).

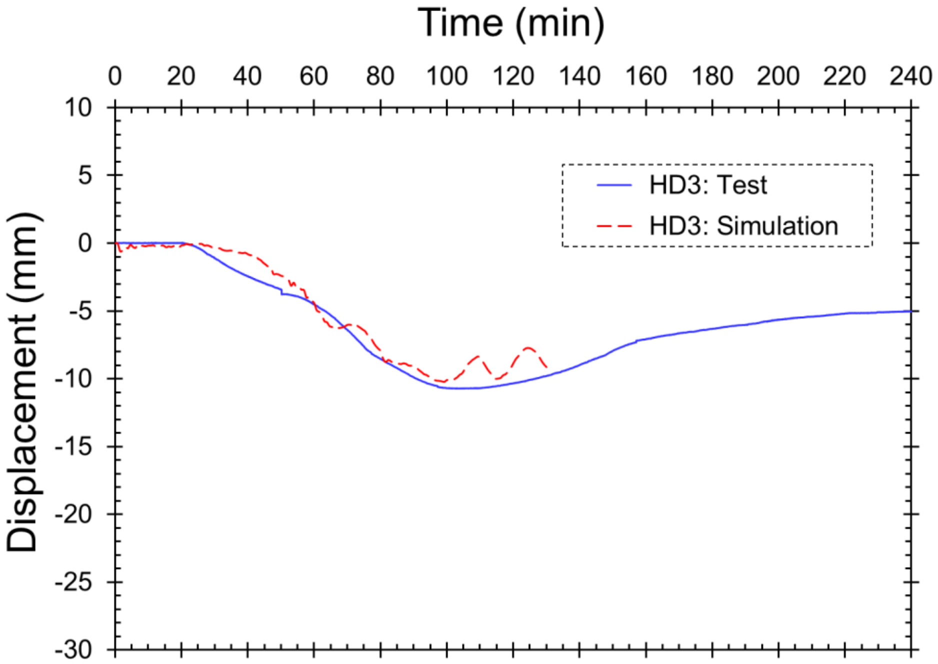

Fig. 105. Simulated and measured horizontal displacement histories for the first-story column west of the northwest column of the fire-test bay (location HD3 in Fig. 83).

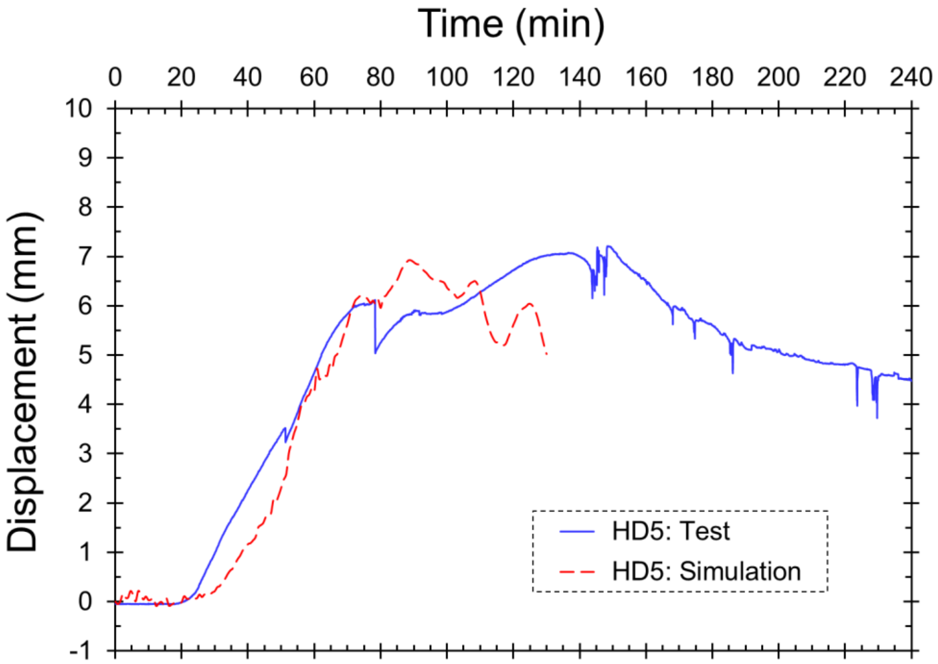

Fig. 106. Simulated and measured horizontal displacement histories for the first-story column east of the northeast column of the fire-test bay (location HD5 in Fig. 83).

Figures 107 and 108 compare calculated and measured horizontal displacements in the north-south direction (Y Direction) for the perimeter columns outside of the fire-tested bay (locations HD1 and HD2 in Fig. 83). The positive values for HD1 and HD2 displacements indicate the northward lateral deflection (in the Y Direction) of the perimeter columns outside of the fire-tested bay due to the thermal expansion of the fire-tested floor slab. Despite discrepancies seen in Figs. 107 and 108, the general shape of displacement-time curves from the analysis and experiment agree reasonably well. Specifically, the percent deviation between the experimental and computational HD1 and HD2 displacements corresponding to the maximum fire temperature was about 18.2 % and 7.1 % for the perimeter columns outside of the fire-tested bay, respectively.

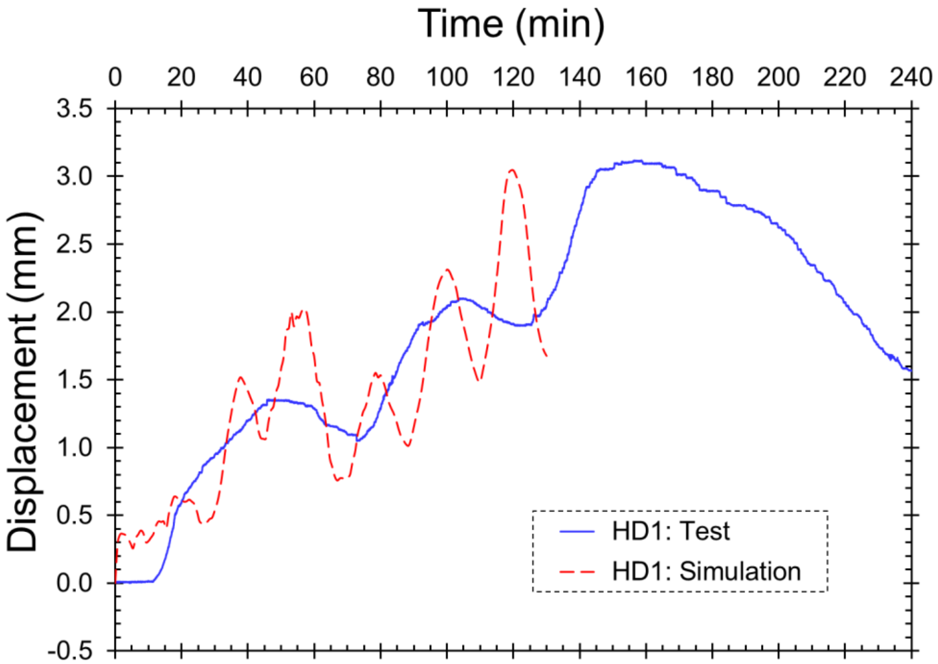

Fig. 107. Simulated and measured horizontal displacement histories for the first-story column north of the northeast column of the fire-test bay (location HD1 in Fig. 83).

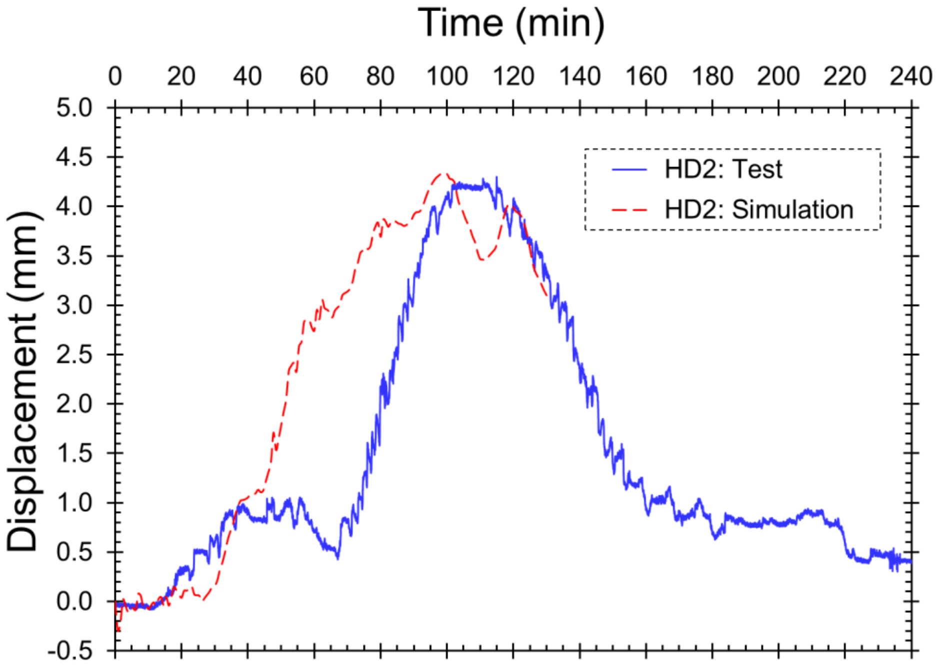

Fig. 108. Simulated and measured horizontal displacement histories for the first-story column northeast of the northeast column of the fire-test bay (location HD2 in Fig. 83).

4.1.2. Deformation-Related Failure Mechanisms

The computational model was also validated based on the deformation mechanisms observed in the experiment. These deformation mechanisms include lateral distortional buckling of W16×31 beams, local buckling of W16×31 beams, and excessive deformation of connection elements.

4.1.2.1. Lateral Distortional Buckling of Steel Beams

As illustrated and discussed previously in reference to Fig. 86, the W16×31 beams exhibited significant lateral displacement of their lower flanges. The lateral displacements of the W16×31 beams were mainly caused by the restraint to thermal expansion from W18×35 girders, the composite slab, and the elements of the steel frame outside of the test bay.

Figure 109 further demonstrates the phenomenon of the lateral distortional buckling of W16×31 beams. The W16×31 beams were isolated from the rest of the framing elements to better observe their laterally deflected shapes.

As can be seen from Fig. 109, the north W16×31 beam underwent significant twisting of its cross section as compared to the middle and south W16×31 beams. This significant twist is caused by the restraint to thermal expansion provided by the surrounding frame elements outside of the test bay. The most evenly restrained and uniformly loaded middle W16×31 beam exhibited the least amount of lateral displacement.

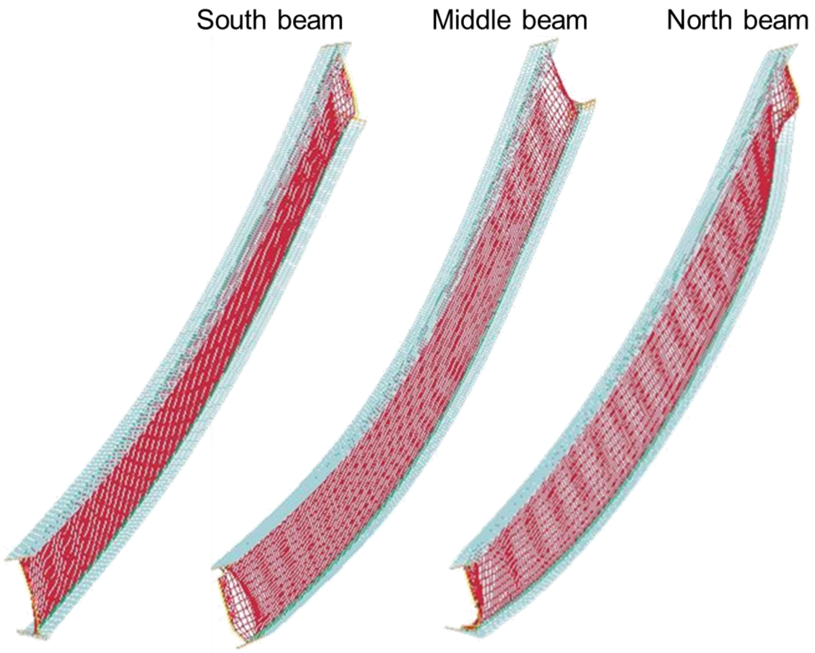

Fig. 109. Lateral displacement of the north, middle, and south W16×31 beams.

The predictions of the lateral displacement of secondary beams are further compared with those from the experiment and are presented in Fig. 110. As can be seen in Fig. 110, due to the significant lateral displacements of their lower flanges, the north and south beams exhibited lateral deformation resembling that of lateral distortional buckling. As seen clearly in Fig. 110, the computational model could predict the vertical load- and heat-induced lateral deformation mechanism of the W16×31 beams corresponding to the maximum fire temperature.

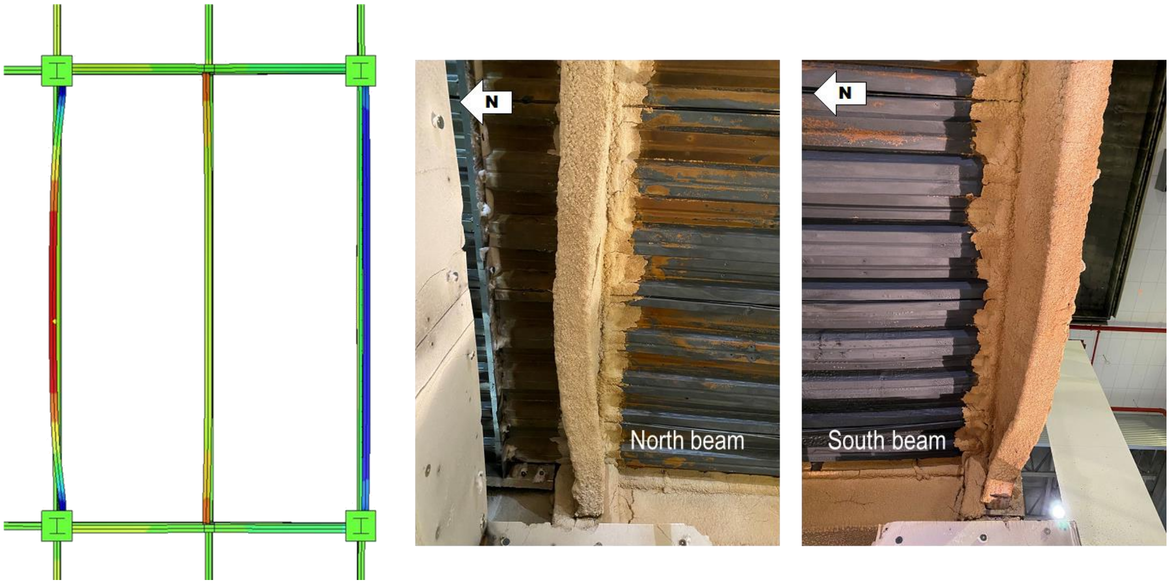

Fig. 110. Simulated and observed lateral displacement of bottom flanges of the north, and south W16×31 beams (test pictures are from Choe et al. 2022).

4.1.2.2. Local Buckling of Steel Beams

Local buckling of the web of the W16×31 beams was another deformation-related failure mechanism that was captured in the analysis. Web local buckling occurred due to the twisting of the beam cross section resulted from lateral displacement in the W16×31 beams. A sample of such observations is provided in Fig. 111, where the local deformations observed at both east and west ends of the south W16×31 beam are compared between the experiment and the simulation. As seen in Fig. 111, the computational model could capture the beam web local buckling failure mode in the connection region that was observed in the experiment.

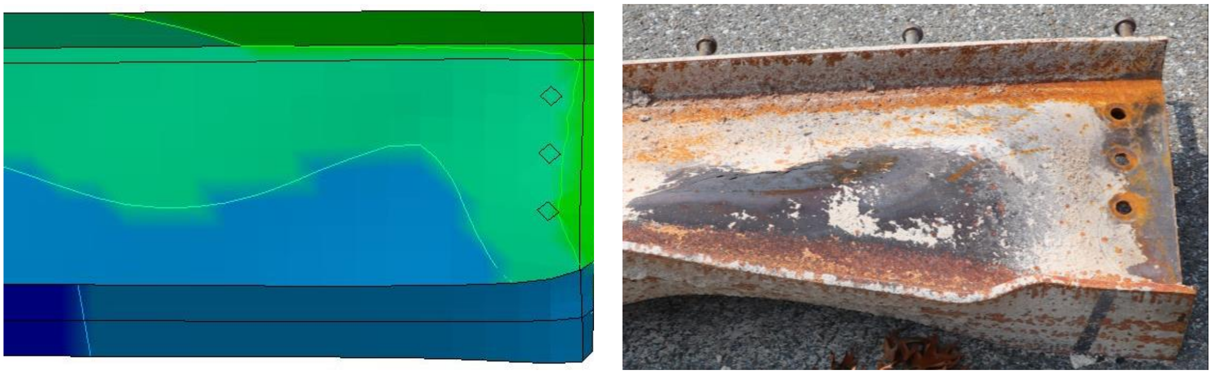

(a) East end

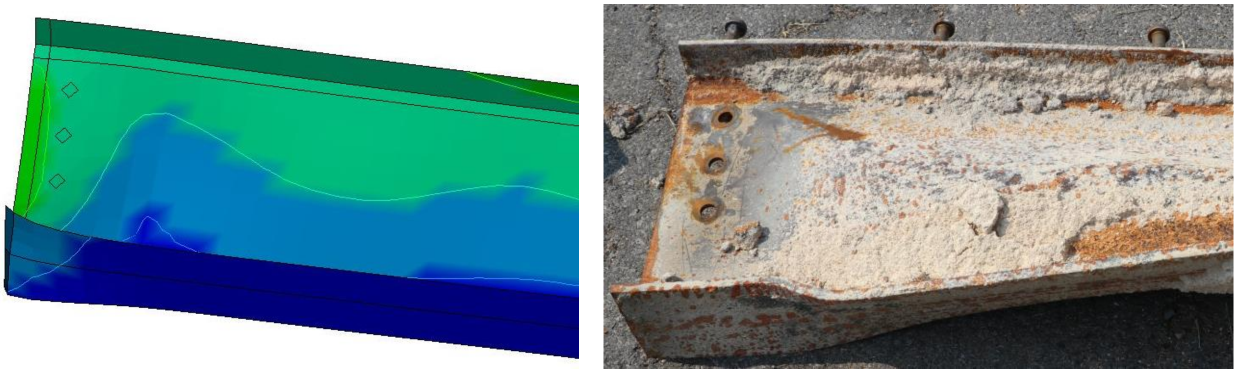

(b) West end

Fig. 111. Local buckling of the south W16×31 beam observed in the experiment and in the simulation: (a) east end; (b) west end (test pictures are from Choe et al. [Choe et al. 2022]).

Note that flange local buckling of the supporting beams did occur during the experiment but was not captured in the analysis. The flange local buckling most probably occurred during the cooling phase of the fire experiment when the bottom flange of the beam was in compression in the vicinity of the connection. Since the analysis was performed under the increasing temperatures and stopped at the point of maximum temperature, local buckling of the bottom flange of the beams due to cooling was beyond the scope of structural responses that were accounted for by the model.

4.1.2.3. Connections

Post-test evaluation of the composite floor system showed that even though connections did not fail, they underwent some major deformations. These observations were particularly relevant to the extended shear tab connections between the W18×35 girders and columns. As shown in Fig. 112, the extended shear tabs torsionally twisted as the composite floor assembly of the test bay expanded in the east-west direction. This east-west expansion occurred because of significant thermal elongation of W16×31 beams. As further seen in Fig. 112, the bottom bolts connected at the south ends of the girders exhibited some degree of bending. As observed in Fig. 112, the computational model was capable of predicting the significant deformations of the extended shear tab connections during the exposure to standard fire.

Note that the bending direction for the shear tab plates predicted in the simulation is opposite to that observed in the experiment (as seen in Fig. 112). This is because observations from the test correspond to a temperature-time environment that includes the cooling phase, while predictions from the simulation are based on a temperature-time environment that only includes the heating phase to the maximum gas temperature in the compartment. More specifically, during the heating phase of the fire, the W16×31 beams of the test bay elongated in response to increasing temperatures. The thermal expansion of the W16×31 beams resulted in outward bending of the extended shear tabs (as shown in Fig. 112 for the simulation). During the cooling phase, thermal contraction of W16×31 beams resulted in inward bending of the extended shear tabs (as shown in Fig. 112 for the simulation).

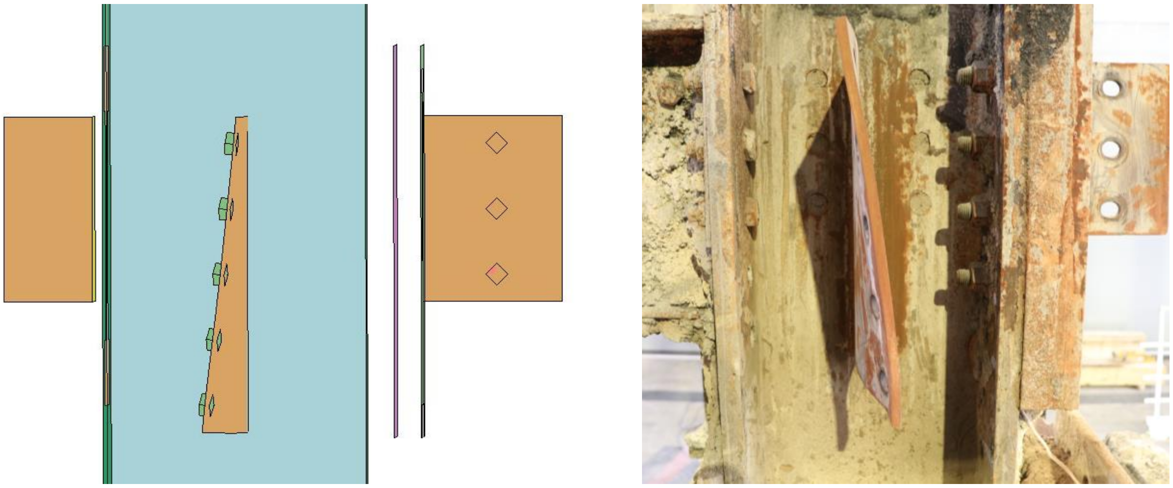

(a) Southeast column

(b) Southwest column

Fig. 112. Deformation of the extended shear tab plates connected to the south columns: (a) southeast column; (b) southwest column (test pictures are from Choe et al. [Choe et al. 2022]).

4.1.2.4. Composite Slab

Formation of cracks in composite slab results in direct exposure of slab reinforcement to fire temperatures that can impact the tensile membrane action of the composite slab and compromise the overall stability of the composite steel-framed structures in fire. Therefore, the ability of the computational model to predict crack formation in the composite slab was of particular interest. In the analysis of composite steel-framed structure, the effective plastic strain was adopted to predict damage or crack formation in the composite slab under the applied load and increasing temperatures.

Figure 113 illustrates the observed crack pattern from the experiments and the crack pattern obtained from the computational model. As can be observed from Fig. 113, the model could predict the crack formation in the composite floor slab with acceptable accuracy.

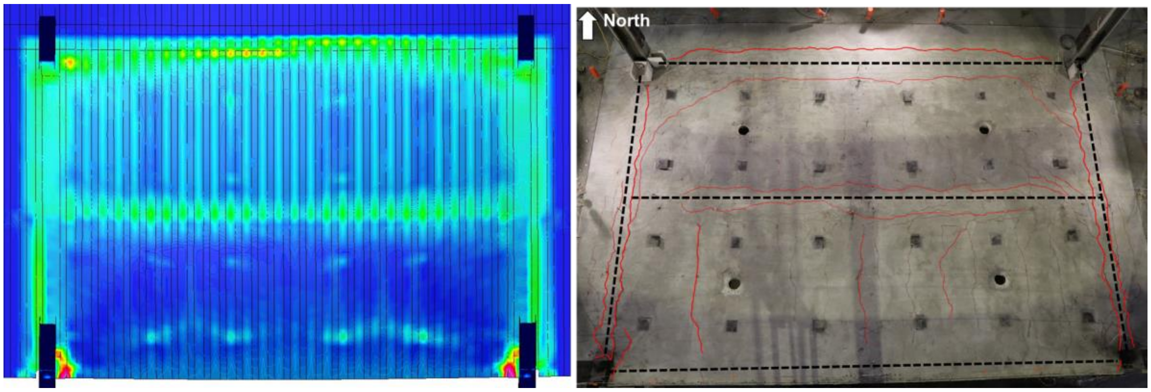

Fig. 113. Simulated and observed cracks in the composite slab of the test bay (test picture is from Choe et al. [Choe et al. 2022]).

4.1.3. Strains

During the NIST NFRL CF2 Test, strains were also measured at different locations along the length of the surrounding beams, and the height of both the supporting and the surrounding columns to quantify the response of structural members in surrounding bays to a compartment fire in the middle bay of the test building. The locations of strain measurement are shown in Fig. 114. Figures 115 and 116 further show the strain probe locations over the cross sections of columns, and beams and girders, respectively. Note that strains were measured at two levels along the column height. Strain gauges with numbers 0 to 3 were installed at 100 mm, while the rest of the strain gauges were installed at 340 mm from the strong floor.

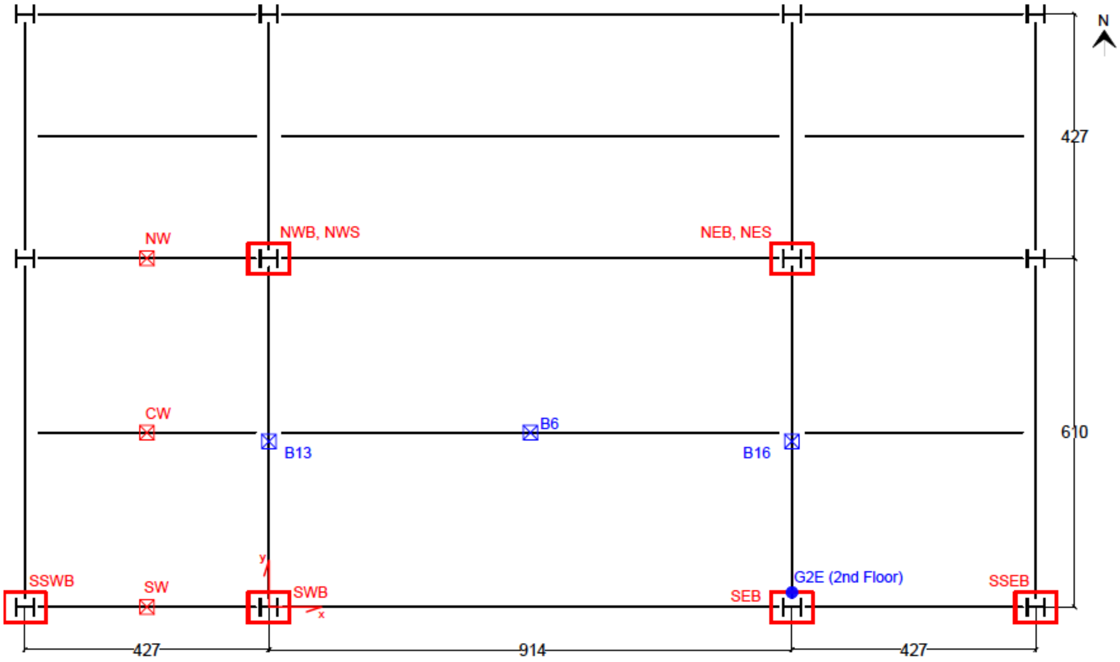

Fig. 114. Location of the measured strains in the NIST NFRL CF2 Test [Choe et al. 2022].

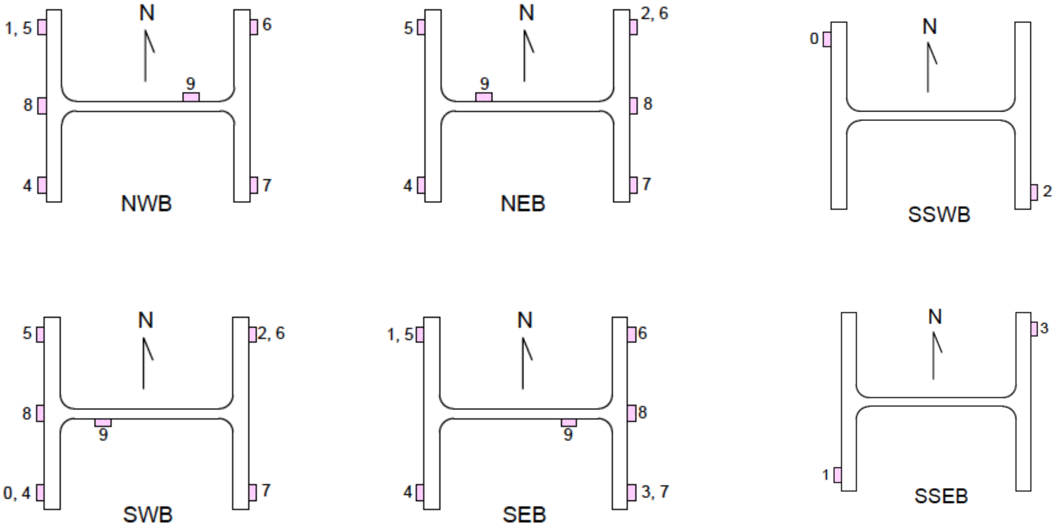

Fig. 115. Location of strain measurement over the cross-section of steel columns in the NIST NFRL CF2 Test [Choe et al. 2022].

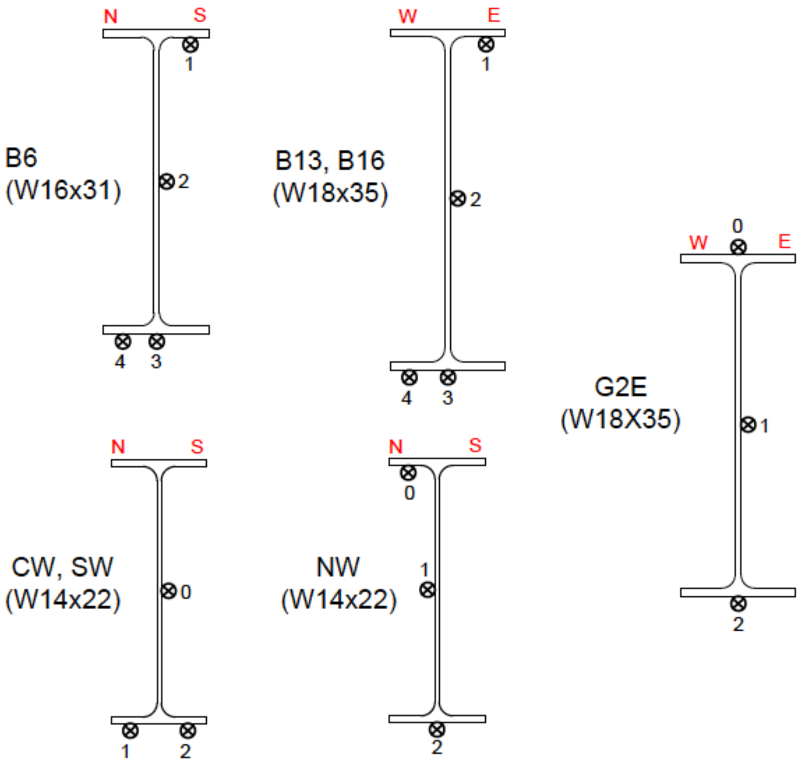

Fig. 116. Location of strain measurement over the cross-section of steel beams and girders in the NIST NFRL CF2 Test [Choe et al. 2022].

4.1.3.1. Column Strains

The computational model was further validated using strain measurements at the bases of the columns supporting the fire-tested floor slab. The accuracy of the model predictions was quantified as the percentage error in the difference between the predicted and measured column strains at the maximum fire temperature.

Figures 117 and 118 compare calculated and measured strains for the southeast column of the fire-tested floor (locations SEB1 and SEB3 in Fig. 115). The positive values for SEB1 and negative values for SEB3 strains indicate the eastward lateral displacement (in the X Direction) of the southeast column of the fire-tested floor due to the thermal expansion of the south edge of the fire-tested floor slab. Despite discrepancies seen in Figs. 117 and 118, the general shape of strain-time curves from the analysis and the experiment agree reasonably well. Specifically, the percent deviation between the experimental and computational SEB1 and SEB3 strains corresponding to the maximum fire temperature was about 13.1 % and 0.6 % for the southeast column of the fire-tested floor, respectively.

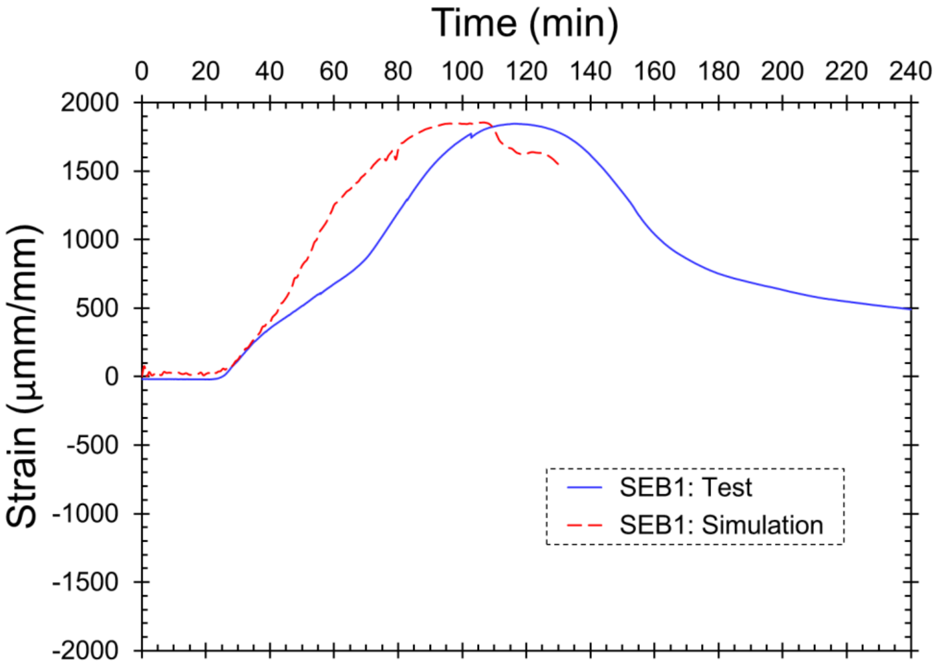

Fig. 117. Simulated and measured strain histories for the southeast column (location SEB1 in Fig. 115).

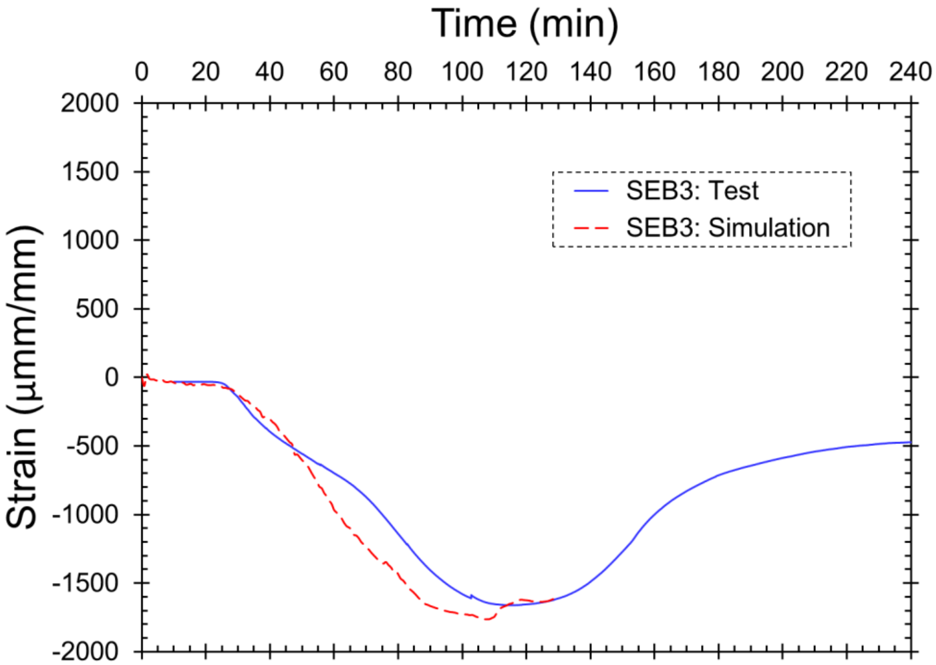

Fig. 118. Simulated and measured strain histories for the southeast column (location SEB3 in Fig. 115).

Figures 119 and 120 compare calculated and measured strains for the southwest column of the fire-tested floor (locations SWB0 and SWB2 in Fig. 115). The negative values for SWB0 and positive values for SWB2 strains indicate the westward lateral displacement (in the -X Direction) of the southwest column of the fire-tested floor due to the thermal expansion of the south edge of the fire-tested floor slab. Despite discrepancies seen in Figs. 119 and 120, the general shape of strain-time curves from the analysis and experiment agree reasonably well. Specifically, the percent deviation between the experimental and computational SWB0 and SWB2 strains corresponding to the maximum fire temperature was about 1.3 % and 4.1 % for the southwest column of the fire-tested floor, respectively.

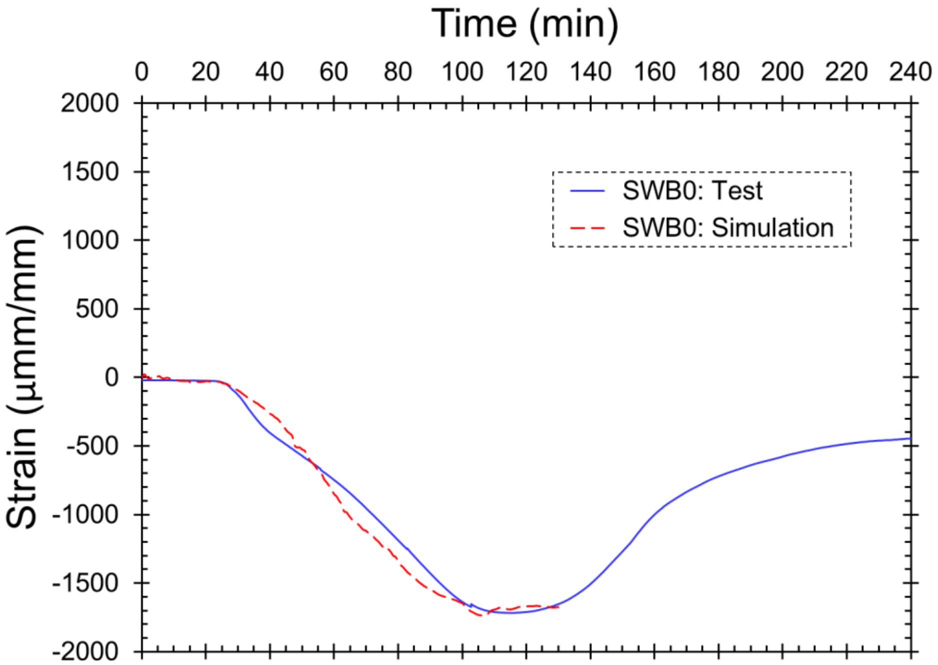

Fig. 119. Simulated and measured strain histories for the southwest column (location SWB0 in Fig. 115).

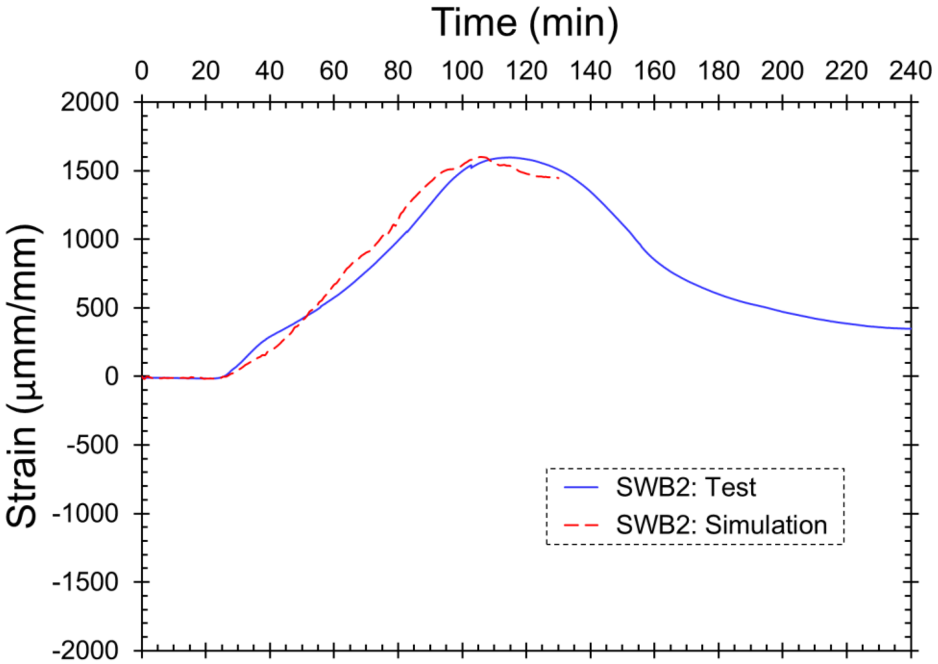

Fig. 120. Simulated and measured strain histories for the southwest column (location SWB2 in Fig. 115).

Figures 121 and 122 compare calculated and measured strains for the northeast column of the fire-tested floor (locations NEB5 and NEB7 in Fig. 115). The positive values for NEB5 and negative values for NEB7 strains indicate the eastward lateral displacement (in the X Direction) of the northeast column of the fire-tested floor due to the thermal expansion of the north edge of the fire-tested floor slab. Despite discrepancies seen in Figs. 121 and 122, the general shape of strain-time curves from the analysis and experiment agree reasonably well. Specifically, the percent deviation between the experimental and computational NEB5 and NEB7 strains corresponding to the maximum fire temperature was about 27.1 % and 17.3 % for the northeast column of the fire-tested floor, respectively.

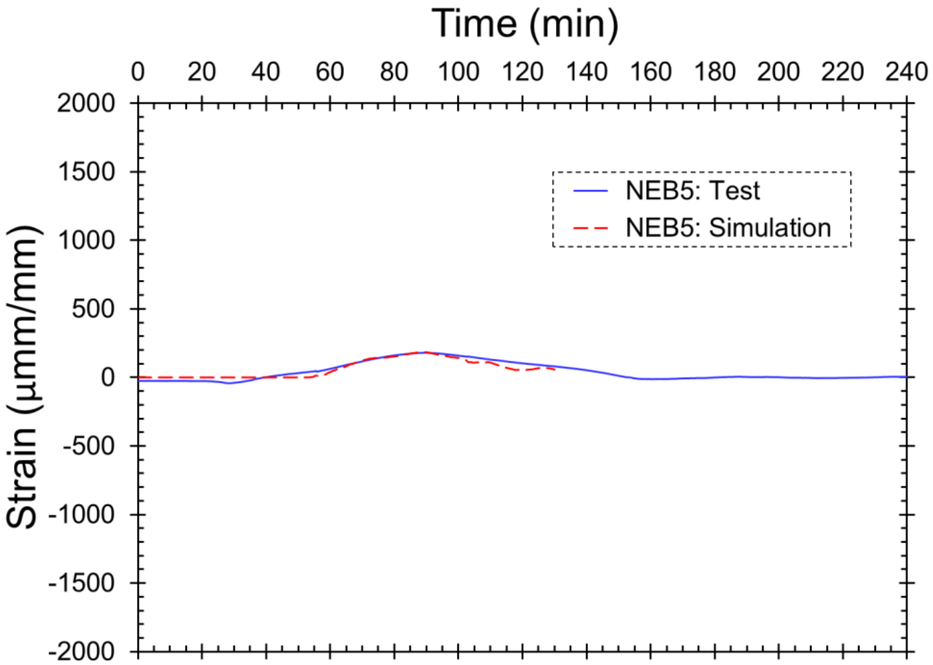

Fig. 121. Simulated and measured strain histories for the northwest column (location NEB5 in Fig. 115).

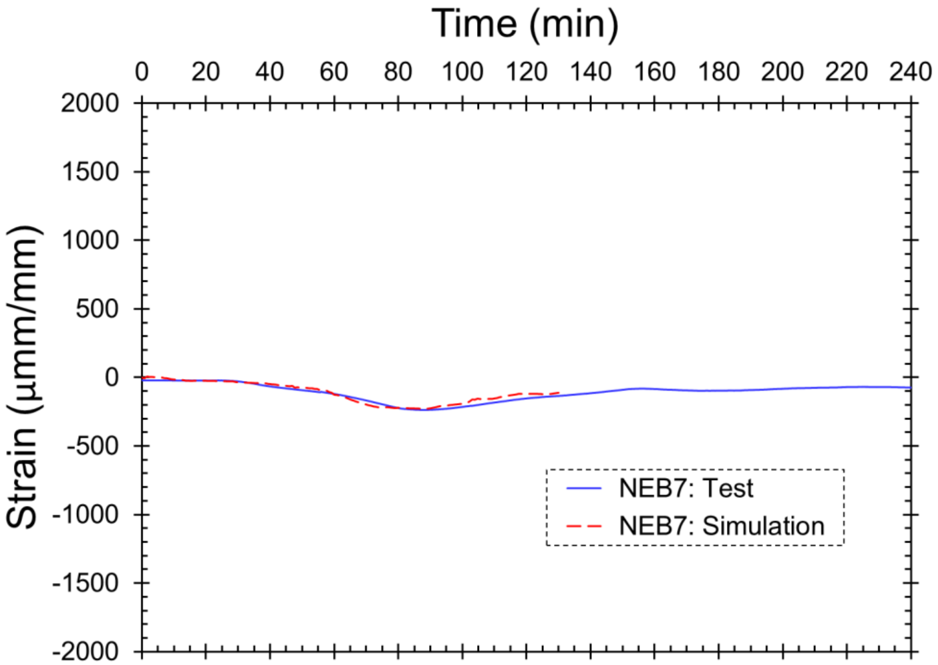

Fig. 122. Simulated and measured strain histories for the northwest column (location NEB7 in Fig. 115).

Figures 123 and 124 compare calculated and measured strains for the northwest column of the fire-tested floor (locations NWB1 and NWB7 in Fig. 115). The negative values for NWB1 and positive values for NWB7 strains indicate the westward lateral displacement (in the -X Direction) of the northwest column of the fire-tested floor due to the thermal expansion of the south edge of the fire-tested floor slab. Despite discrepancies seen in Figs. 123 and 124, the general shape of strain-time curves from the analysis and experiment agree reasonably well. Specifically, the percent deviation between the experimental and computational NWB1 and NWB7 strains corresponding to the maximum fire temperature was about 21.9 % and 23.9 % for the southwest column of the fire-tested floor, respectively.

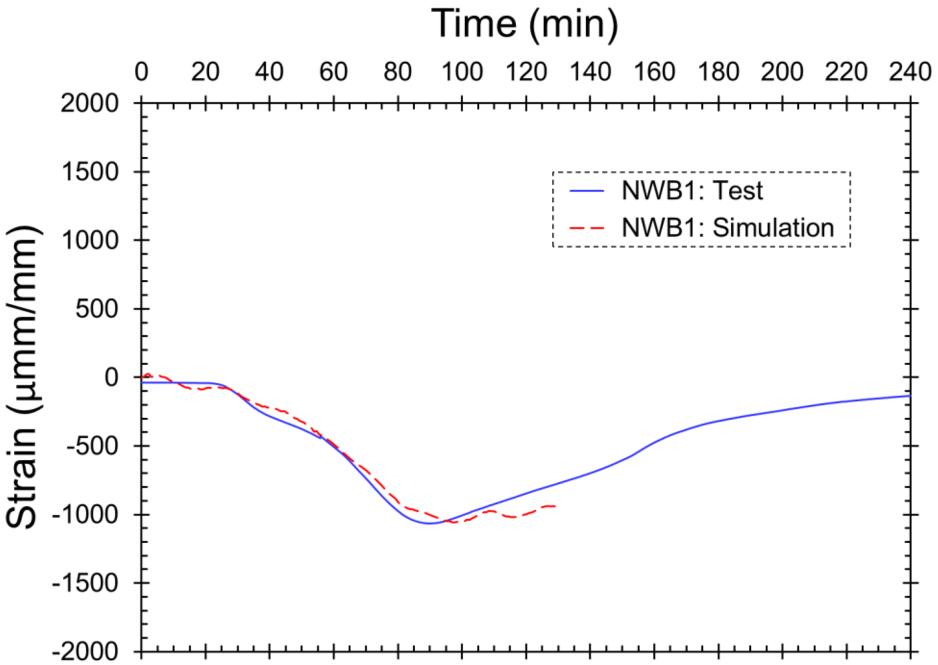

Fig. 123. Simulated and measured strain histories for the northwest column (location NWB1 in Fig. 115).

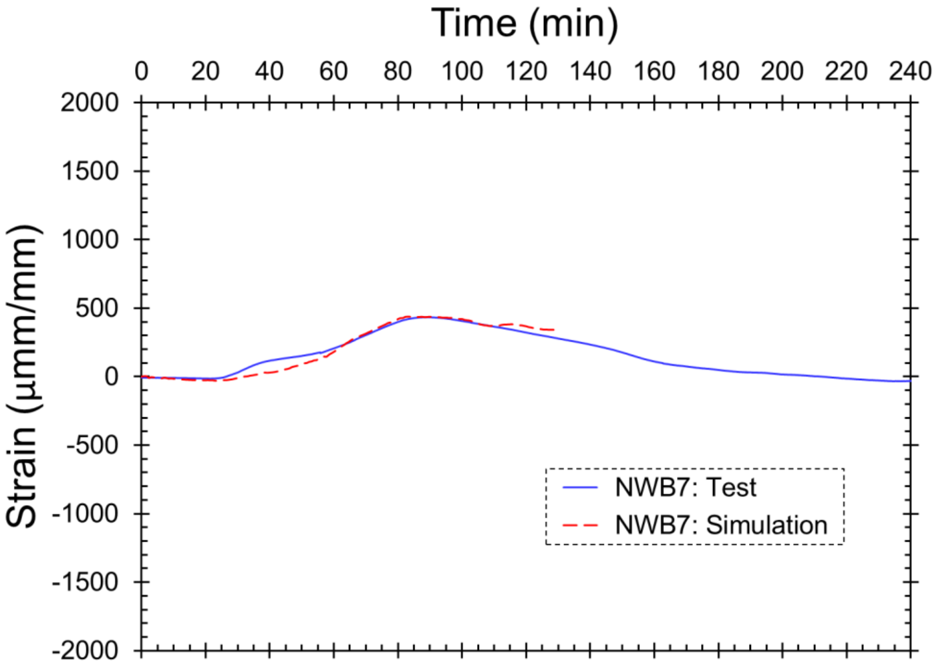

Fig. 124. Simulated and measured strain histories for the northwest column (location NWB7 in Fig. 115).

4.1.3.2. Beam Strains

Strain measurements at the midspan of the north, center, and south W14×22 beams (locations NW, CW, and SW in Fig. 114, respectively), of the floor bay west of the test bay, were also utilized to validate the computational model. The accuracy of the strain predictions was quantified as the percentage error in the difference between the predicted and measured beam strains at the maximum fire temperature. Note that one of the factors contributing to the discrepancies observed between simulated and measured beam strains is the beam temperature. The W14×22 beams were assumed to stay at ambient temperature (20 °C as indicated in Fig. 81) in the simulation, while these beams were exposed to temperatures up to 50 °C in the experiment [Choe et al. 2022].

Figures 125, 126, and 127 compare calculated and measured strains at the midspan of the north W14×22 beam (locations NW0, NW1, and NW2 in Fig. 116, respectively). The negative values for NW0, NW1, and NW2 strains indicate the westward axial displacement (in the -X Direction) of the north W14×22 beam of the west bay due to the thermal expansion of the W16×31 beams of the fire-tested floor slab. Despite discrepancies seen in Figs. 125, 126, and 127, the general shape of strain-time curves from the analysis and the experiment agree reasonably well. Specifically, the percent deviation between the experimental and computational NW0, NW1, and NW2 strains corresponding to the maximum fire temperature was about 19.3 %, 17.1 %, and 35.8 % for the north W14×22 beam of the bay west of the fire-tested floor, respectively.

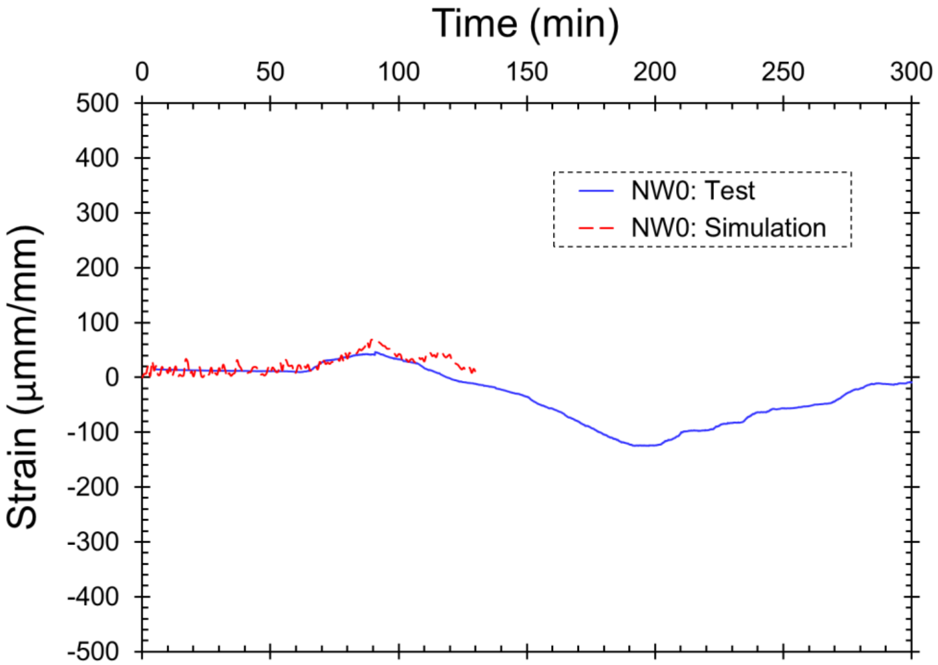

Fig. 125. Simulated and measured strain histories at the midspan of the north W14×22 beam (location NW0 in Fig. 116).

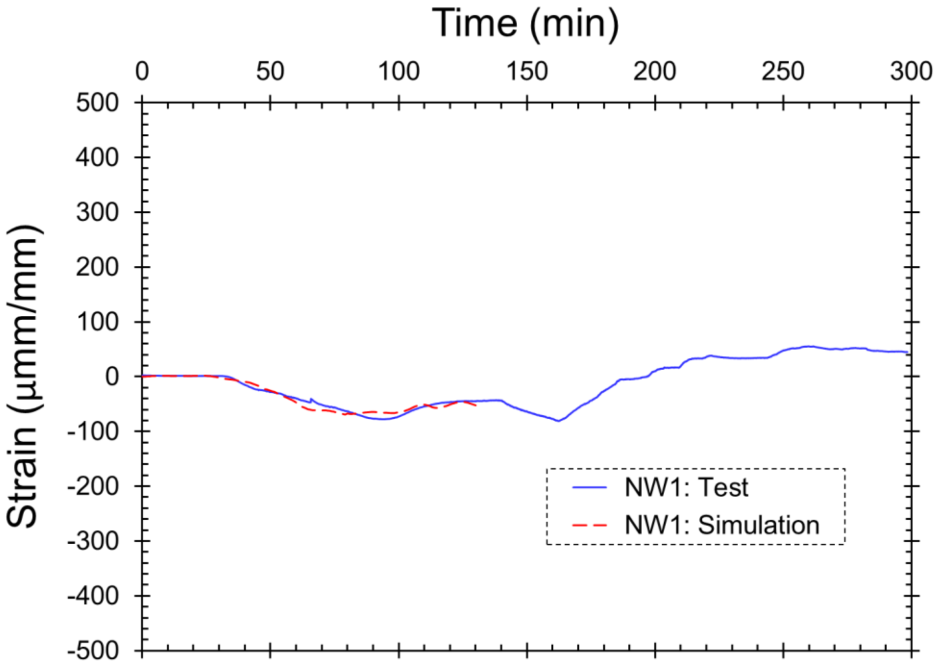

Fig. 126. Simulated and measured strain histories at the midspan of the north W14×22 beam (location NW1 in Fig. 116).

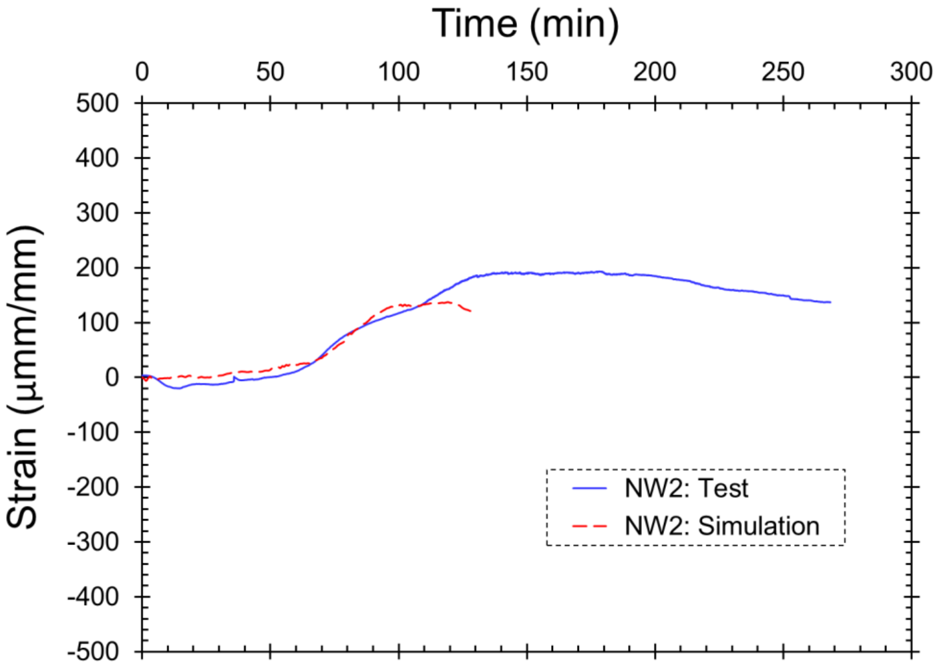

Fig. 127. Simulated and measured strain histories at the midspan of the north W14×22 beam (location NW2 in Fig. 116).

Figures 128, 129, and 130 further present calculated and measured strains at the midspan of the center W14×22 beam (locations CW0, CW1, and CW2 in Fig. 116, respectively). As seen in Figs. 128, 129, and 130, the overall shape of strain-time curves from the analysis agrees quite reasonably with the corresponding one from the experiment. Specifically, the percent deviation between the experimental and computational CW0, CW1, and CW2 strains corresponding to the maximum fire temperature was about 8.5 %, 8.0 %, and 9.3 % for the center W14×22 beam of the bay west of the fire-tested floor, respectively.

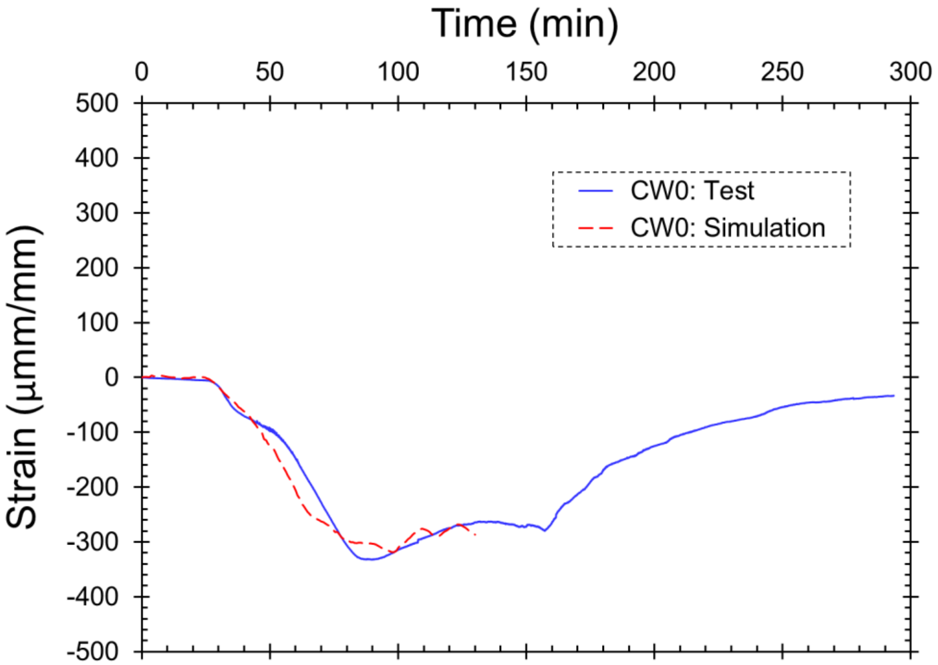

Fig. 128. Simulated and measured strain histories at the midspan of the center W14×22 beam (location CW0 in Fig. 116).

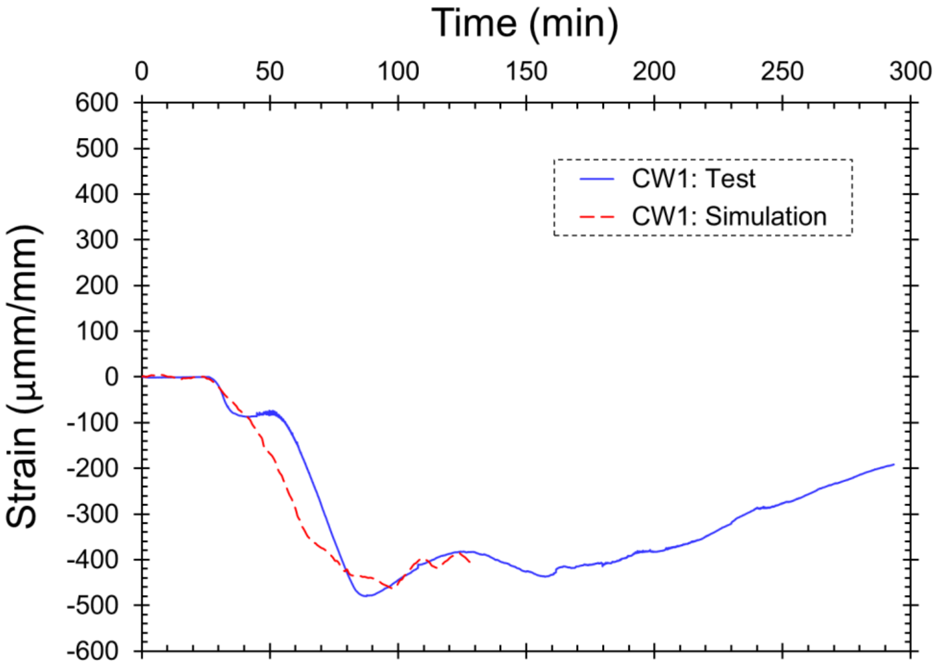

Fig. 129. Simulated and measured strain histories at the midspan of the center W14×22 beam (location CW1 in Fig. 116).

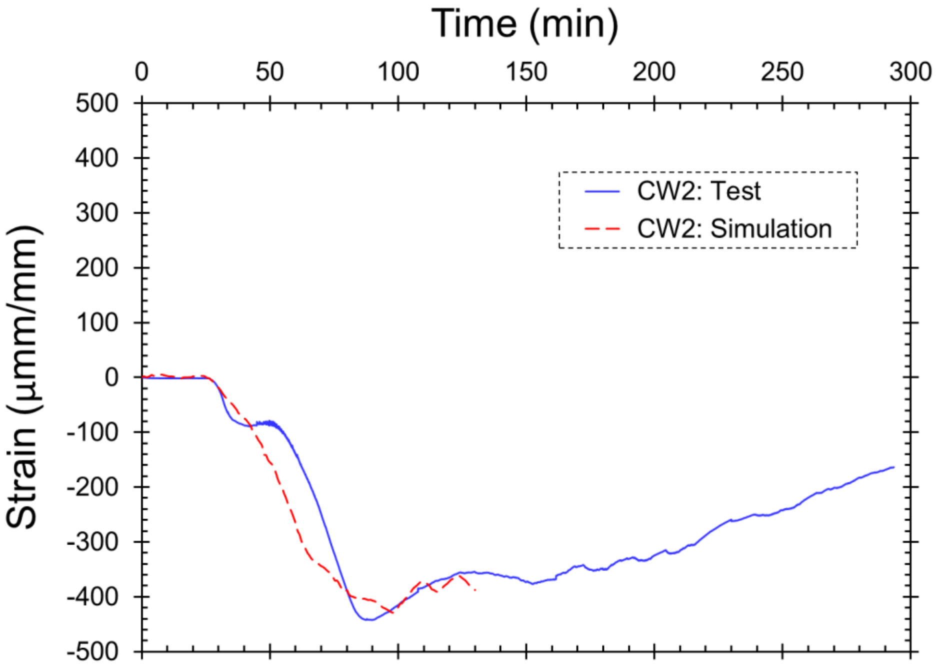

Fig. 130. Simulated and measured strain histories at the midspan of the center W14×22 beam (location CW2 in Fig. 116).

Comparisons between simulated and measured strains at the midspan of the south W14×22 beam (locations SW1 and SW2 in Fig. 116) are also shown in Figs. 131, and 132, respectively. As seen in Figs. 131, and 132, the overall shape of strain-time curves from the analysis agrees quite reasonably with the corresponding one from the experiment. Specifically, the percent deviation between the experimental and computational SW1, and SW2 strains corresponding to the maximum fire temperature was about 4.7 %, and 83.2 % for the south W14×22 beam of the bay west of the fire-tested floor, respectively.

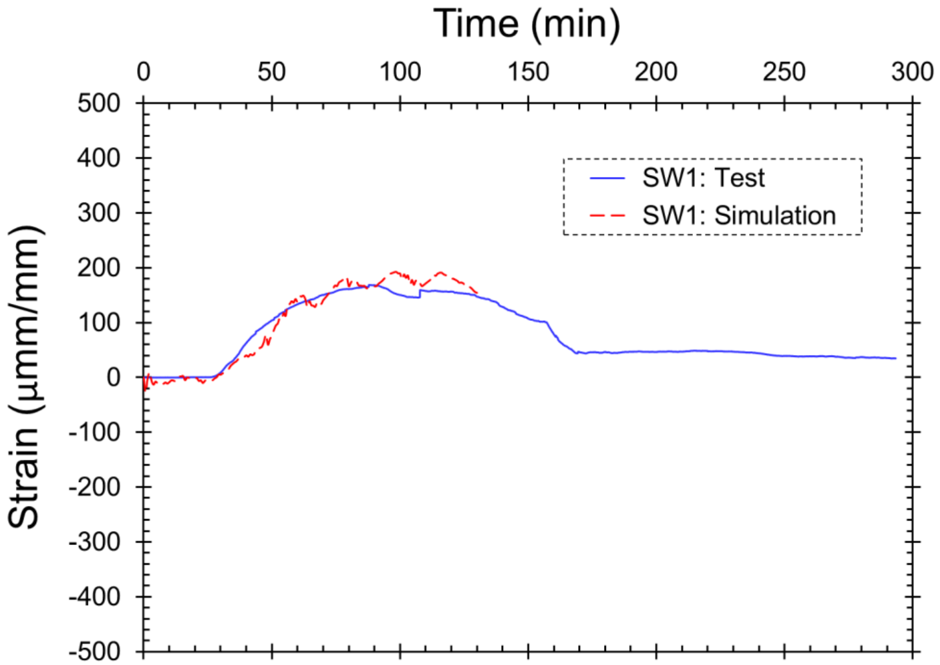

Fig. 131. Simulated and measured strain histories at the midspan of the south W14×22 beam (location SW1 in Fig. 116).

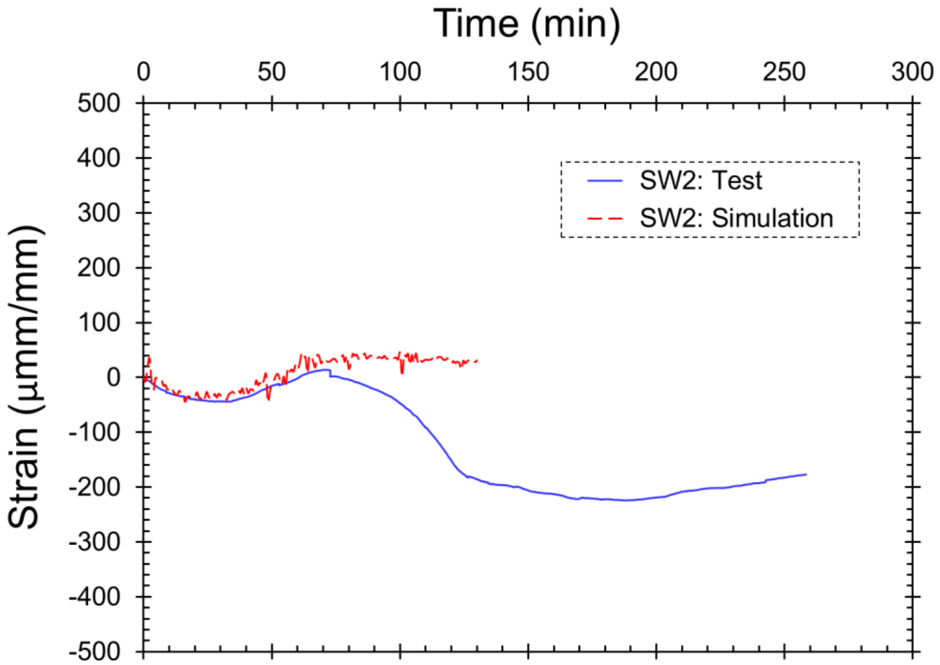

Fig. 132. Simulated and measured strain histories at the midspan of the south W14×22 beam (location SW2 in Fig. 116).

5. Computational Model: Extended Results

The validated model was used to examine the forces and stresses developed at locations of the CF2 Test that did not have measurements. More specifically, the model was used to study crucial information such as stresses in bolts and axial forces in secondary beams that were not directly measured in the CF2 Test. These analysis results beyond observations from experiment are provided and discussed in this section.

5.1. Forces

As discussed previously in reference to Fig. 85, the W16×31 beams in the test bay exhibit a large increase in length due to exposure to increasing fire temperatures. These thermal deformations are further restrained by the W18×35 girders in the test bay, the composite slab, and the members of the steel frame outside of the test bay. The restraint to thermal expansion results in axial forces in the W16×31 beams. The accurate evaluation of these axial forces is crucial since they can potentially cause failure of shear tab connections at beam ends.

Figure 133 shows a plot of axial force histories for the north, middle, and south W16×31 beams obtained at beam ends in the simulation. As seen in Fig. 133, and as also expected, the north W16×31 beam with the highest degree of thermal restraint exhibits significant axial load levels during the exposure to elevated temperatures. The high axial force demand for the north W16×31 beam also explains the significant twist in the cross section and lateral distortional behavior of this beam as discussed previously in reference to Fig. 86. Degradations of both strength and stiffens of structural steel with increasing temperatures result in large deflections and hence reductions in axial compressive forces in W16×31 beams as shown in Fig. 133.

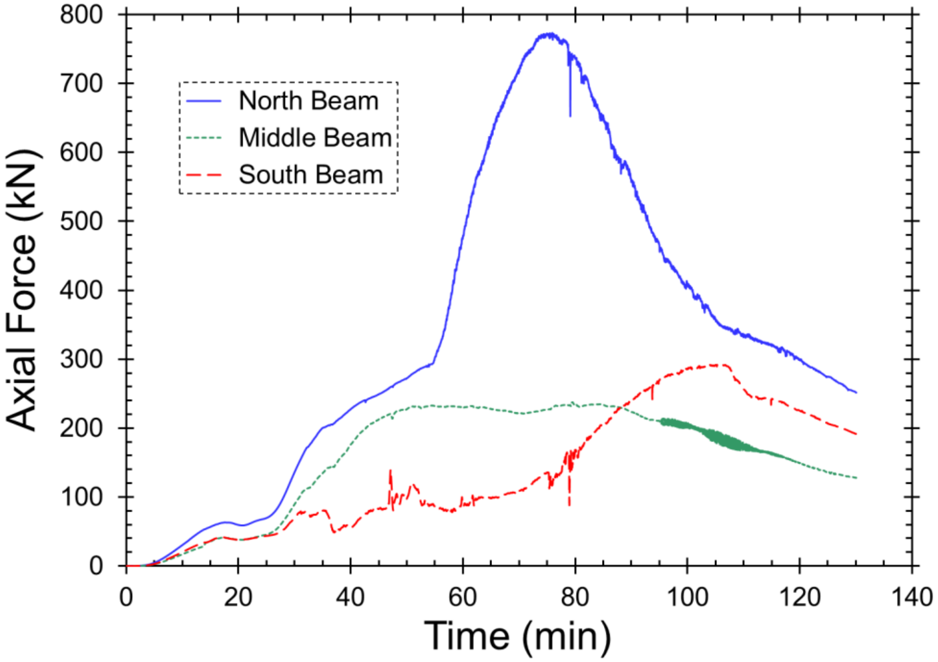

Fig. 133. Simulated axial force histories for the north, middle, and south W16×31 beams.

5.2. Stresses

Accurate accounting of stresses in the different components of connections in composite steel-framed buildings is important in identifying failure modes of connections exposed to fire temperatures. Of special interest are stresses in the bolts. Overstressing of the bolts in response to the axial forces induced by heating and/or cooling might lead to bolt failure and propagate to full connection failure.

The validated model was used to evaluate bolt shear stresses at various connection locations in the test bay, and to gain insight into the behavior and potential failure modes of the composite floor system subjected to the test fire. Representative results for bolt shear stress as a function of temperature are shown in Figs. 134, 135, and 136 for the three bolts of the shear tab connections at the east end of the north, middle, and south W16×31 beams, respectively. Additionally, Figs. 137, and 138 present variations in bolt shear stresses with temperature for the five bolts of the extended shear tab connections at the north and south ends of the east W18×35 girder, respectively. For reference, pictures of bolts following the CF2 fire test are also included as inserts. Note that the bolts shown in Fig. 135 did not actually fracture during the test, rather they were torch cut to disassemble the damaged beam after the test. Further, note that the bolt shear stresses in Figs. 134, 135, 136, 137, and 138 are presented as effective plastic stresses. The effective (equivalent) plastic stresses are computed in LS-DYNA using the von Mises criterion (shown as Eq. 11)) to represent bolt shear stresses under multiaxial stress conditions. The effective plastic stresses, $\bar{\sigma}$, are defined in terms of principal stresses (σ_1, σ_2, σ_3) in Eq. (11).

$$\bar{\sigma} = \sqrt{\left(\frac{1}{2}\right)\left[(\sigma_1 - \sigma_2)^2 + (\sigma_2 - \sigma_3)^2 + (\sigma_3 - \sigma_1)^2\right]} \tag{11}$$

Furthermore, as discussed in Sections 3.1.1.3 and 3.2.2, a macro-modeling approach was used to represent the axial load-displacement behavior of each bolt row in shear tab connections. The axial load-displacement relationship for each bolt row was then converted to a stress-strain relationship based on the dimensions of the solid elements used in the macro-modeling. Therefore, the bolt stresses in Figs. 134 to 138 depend on the geometry of the bolt in the computational model and cannot be directly compared with the nominal or experimental values for bolt strength at ambient and elevated temperatures (e.g., values reported in Table 1).

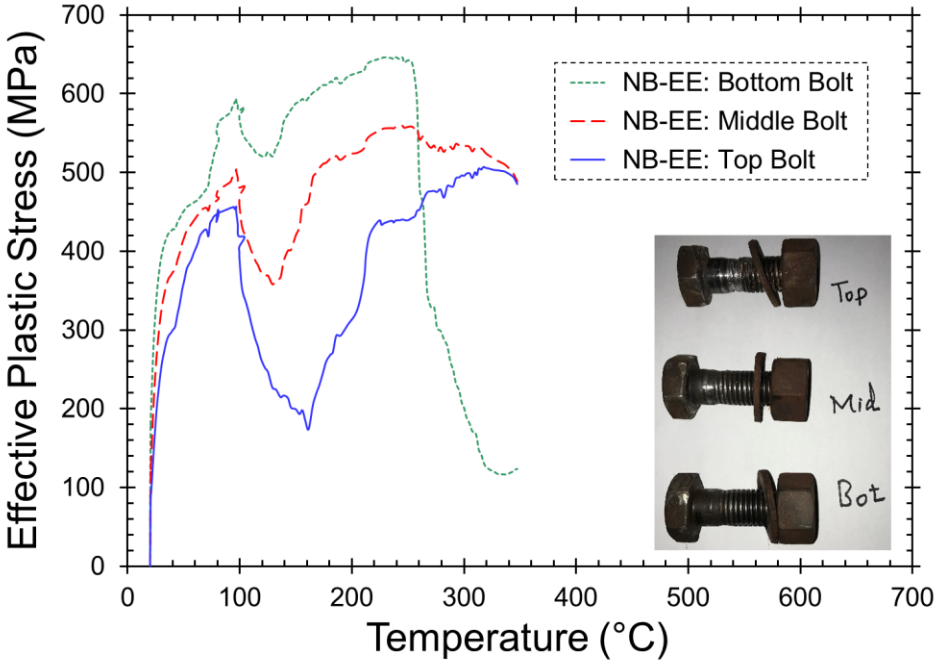

Fig. 134. Simulated bolt shear stress-temperature histories at the east-end (EE) of the north W16×31 beam (NB).

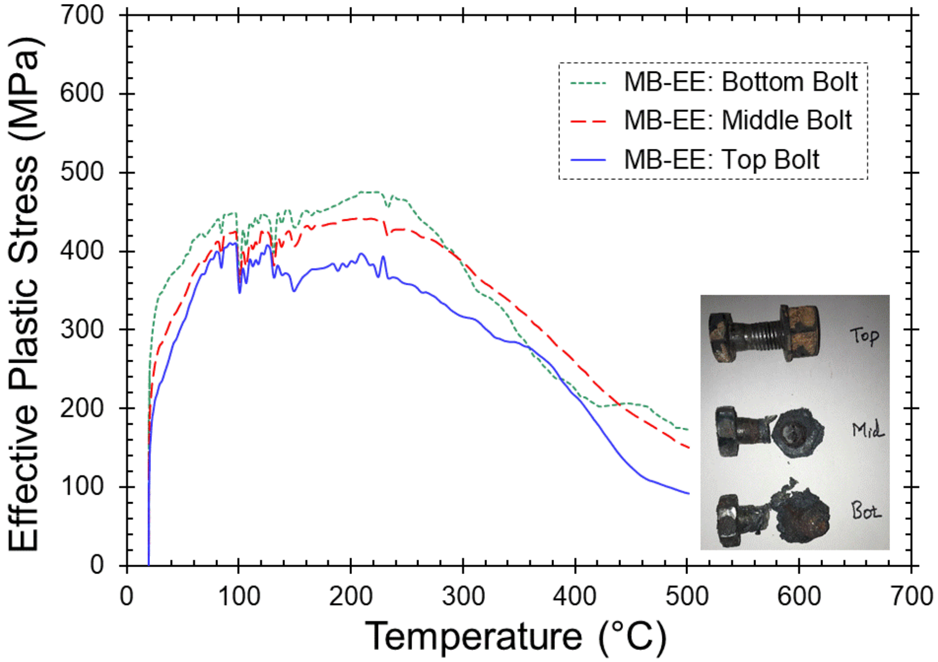

Fig. 135. Simulated bolt shear stress-temperature histories at the east-end (EE) of the middle W16×31 beam (MB).

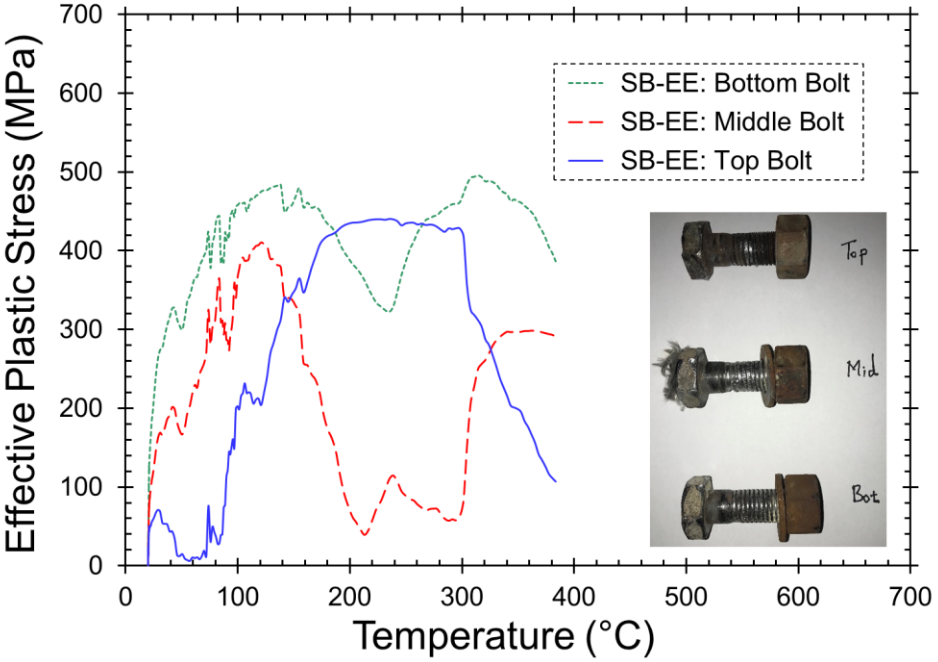

Fig. 136. Simulated bolt shear stress-temperature histories at the east-end (EE) of the south W16×31 beam (SB).

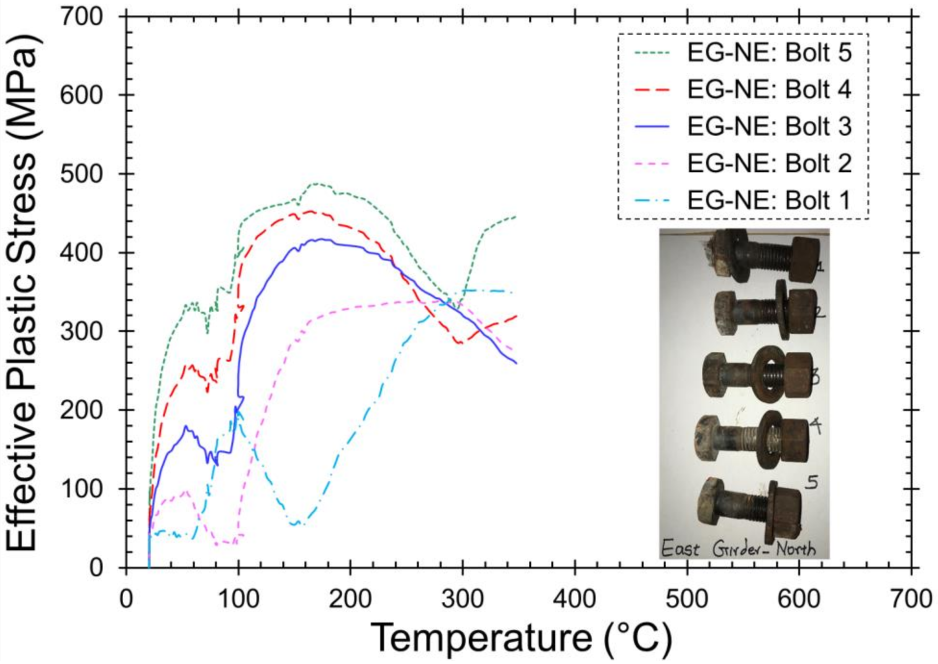

Fig. 137. Simulated bolt shear stress-temperature histories at the north-end (NE) of the east W18×35 girder (EG).

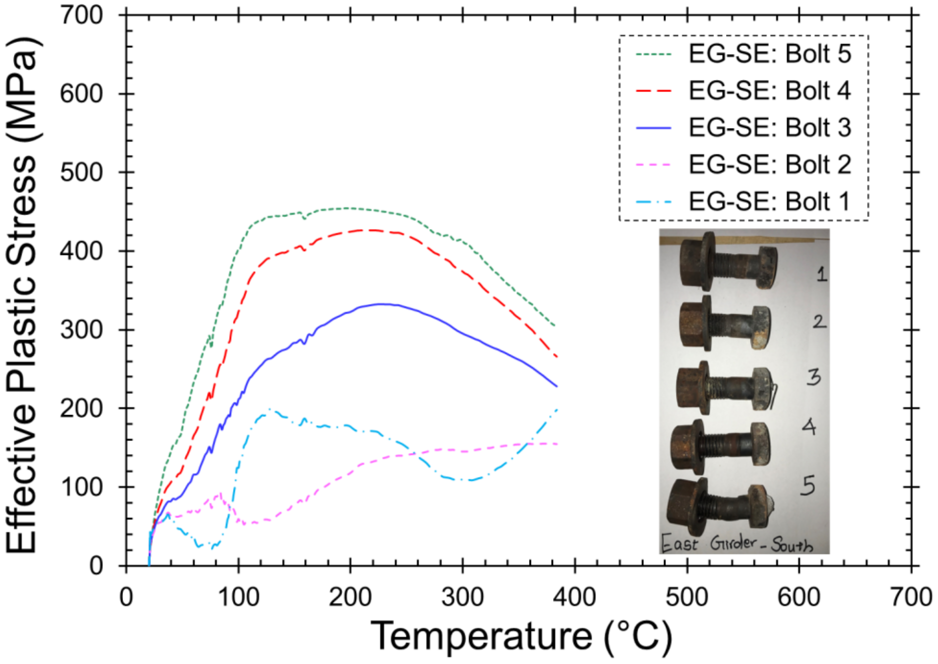

Fig. 138. Simulated bolt shear stress-temperature histories at the south-end (SE) of the east W18×35 girder (EG).

Important observations can be made from the bolt shear stress data presented in Figs. 134 to 138. First, bolt stresses are higher for the north W16×31 beam (Fig. 134). This is expected since the north W16×31 beam had the highest degree of thermal restraint, and thus developed significant axial loads during the exposure to elevated temperatures. In other words, the bolt stress level corresponds to the level of thermal-restraint conditions at the beam ends. Second, the concave-up deflections of the W16×31 beams and W18×35 girders in response to increasing fire temperatures resulted in higher stresses in the bottom bolts. Third, as specifically seen in Fig. 134, the buckling of the beam web in the vicinity of the connection resulted in relaxation of bolt stresses.

Overall, the information presented in Figs. 134 to 138 on bolt shear stresses indicate relatively complex unloading and reloading paths of bolt stresses with increasing temperatures. With no experimental data available in the literature to understand and characterize the complex behaviors of connections experiencing load reversal (hysteresis) while subjected to elevated temperatures, it is difficult to separate the concurrent influences of load reversal and material-driven degradation in strength and stiffness of the connection components.

To provide some context and explanation for the complex unloading and reloading stress paths for bolts with increasing temperatures, a strain-based approach is adopted where bolt shear strains in the form of effective plastic strains are calculated and plotted as functions of temperature. The bolt response to fire temperatures is then represented in the form of effective plastic stress versus effective plastic strain and is compared with the stress-strain characterization of the bolt at elevated temperatures. As an example, the shear strains in response to increasing fire temperatures are plotted in Fig. 139 for the bolts of the extended shear tab connection at the north-end of the east W18×35 girder. Shear strains in Fig. 139 are presented as effective plastic strains. The effective (equivalent) plastic strains are computed in LS-DYNA using the von Mises criterion (shown as Eq. (12)) to represent bolt shear strains under multiaxial strain conditions. The effective plastic strains, $\bar{\varepsilon}$, are defined in terms of principal strains (ε_1, ε_2, ε_3) in Eq. (12).

$$\bar{\varepsilon} = \sqrt{\left(\frac{2}{3}\right)\left(\varepsilon_1^2 + \varepsilon_2^2 + \varepsilon_3^2\right)} \tag{12}$$

It is important for the reader to note that, as discussed in Sections 3.1.1.3 and 3.2.2, the bolt shear strains in Fig. 139 depend on the geometry of the bolt in the computational model and cannot be directly compared with the nominal or experimental values for bolt deformation at ambient and elevated temperatures.

Similar to observations from the bolt shear stress histories shown in Fig. 138, Fig. 139 indicates higher shear strains for the bottom bolt (Bolt 5). This is again due to the concave up deflection of the east W18×35 girder in response to increasing fire temperatures. The differences between strain magnitudes for different bolts, however, are higher than those for stresses. More importantly, several periods of constant strain can be seen for bolt shear strain-temperature histories in Fig. 139. In other words, restraint from other connection components results in intervals where bolts are not deforming while the entire connection undergoes deformation in response to deflections of the east W18×35 girder and fire exposure.

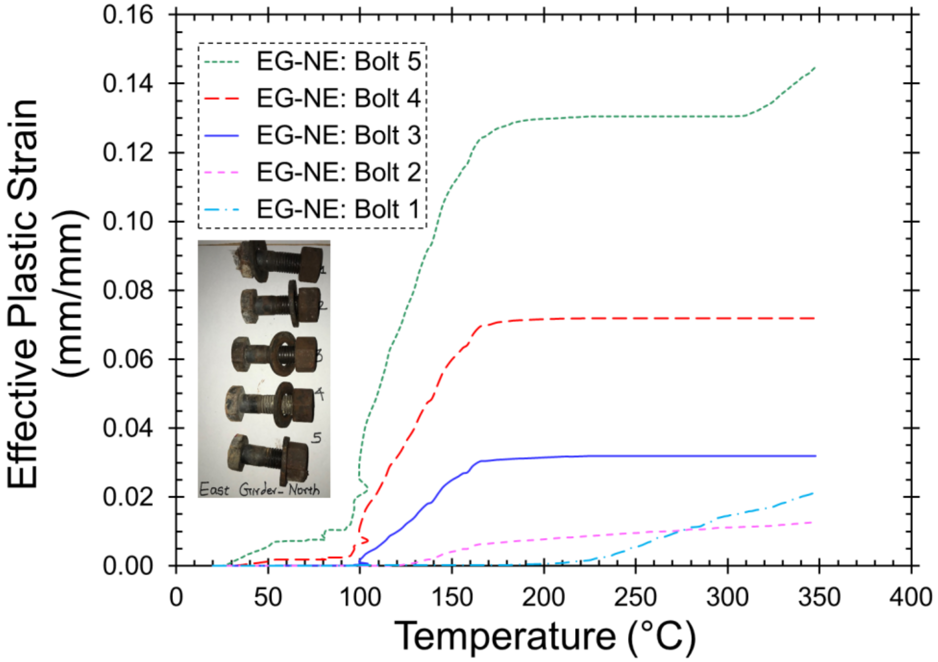

Fig. 139. Simulated bolt shear strain-temperature histories at the north-end (NE) of the east W18×35 girder (EG).

Figure 140 further shows the shear stress-strains response for the bottom bolt (Bolt 5) of the extended shear tab connection at the north-end of the east W18×35 girder. The bolt behavior is represented in terms of effective plastic stress versus effective plastic strain. The plastic stress-plastic strain curves representing the uniaxial material model of the bolts at different temperatures are also shown in Fig. 140. Note that, as seen in Fig. 140, plotting the stress-strain behavior in terms of effective stresses and effective strains allows for direct comparison between the bolt behavior under complex multiaxial loading conditions with the one from uniaxial tensile test.

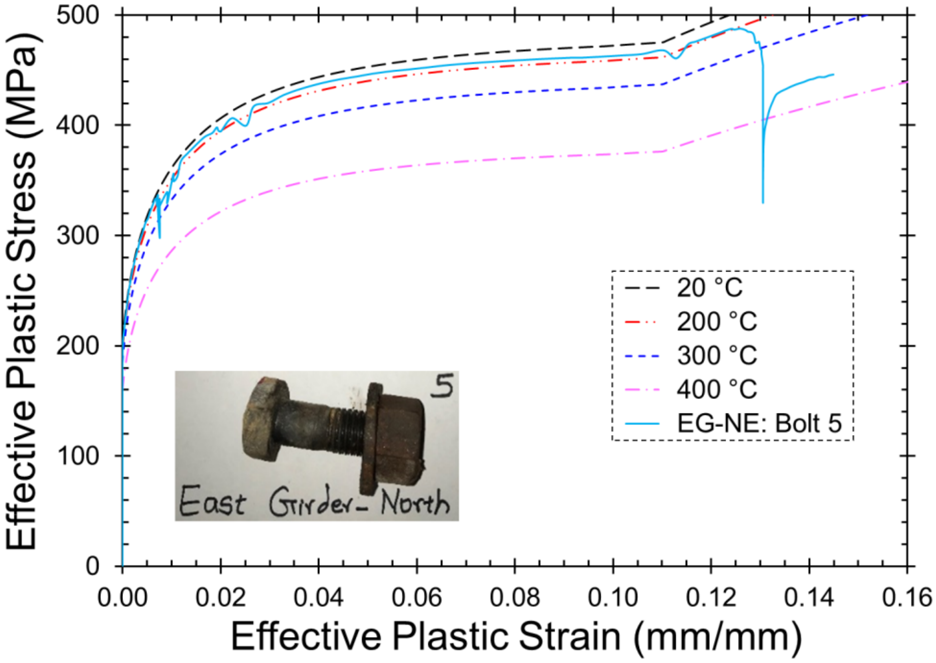

Fig. 140. Simulated bolt shear stress-strain to fire temperatures for the bottom bolt (Bolt 5) of the extended shear tab connection at the north-end (NE) of the east W18×35 girder (EG).

Figure 140, indicates that the stress-strain behavior of the bottom bolt (Bolt 5) lies between the uniaxial stress-strain curves at ambient and 200 °C up to the plastic strain of about 0.125 mm/mm. This observation is consistent with the calculated temperatures of the Bolt 5 between ambient and 150 °C for the plastic strain ranges of zero to 0.125 mm/mm. Figure 140 further shows several drops in the shear stresses for Bolt 5. These stress drops correspond to the intervals of constant strain shown in Fig. 139. The major drop in Bolt 5 shear stresses occurs at the shear strain of about 0.125 mm/mm. This stress drop corresponds to the constant shear strain condition shown in Fig. 139 for bolt temperatures between 150 °C and 310 °C.

The drops in bolt shear stresses at elevated temperatures in Fig. 140 are indicative of the phenomenon of stress relaxation of bolts at elevated temperatures. Stress relaxation or decrease in stresses with time occurs when steel is subjected to constant strain and temperature. The phenomenon of stress relaxation for steel at elevated temperatures is shown in Fig. 141, in which stress-strain curves are presented for samples of ASTM A992 steel subjected to constant strain intervals at temperatures of 300 °C and 400 °C. As further seen in Fig. 142, the ASTM A992 steel specimens were subjected to the constant strain intervals of 30 min. and 3 min. in tension tests at 300 °C and 400 °C. Figure 143 further plots stress variations with time where the drop in stress values over each constant strain interval is clearly observed.

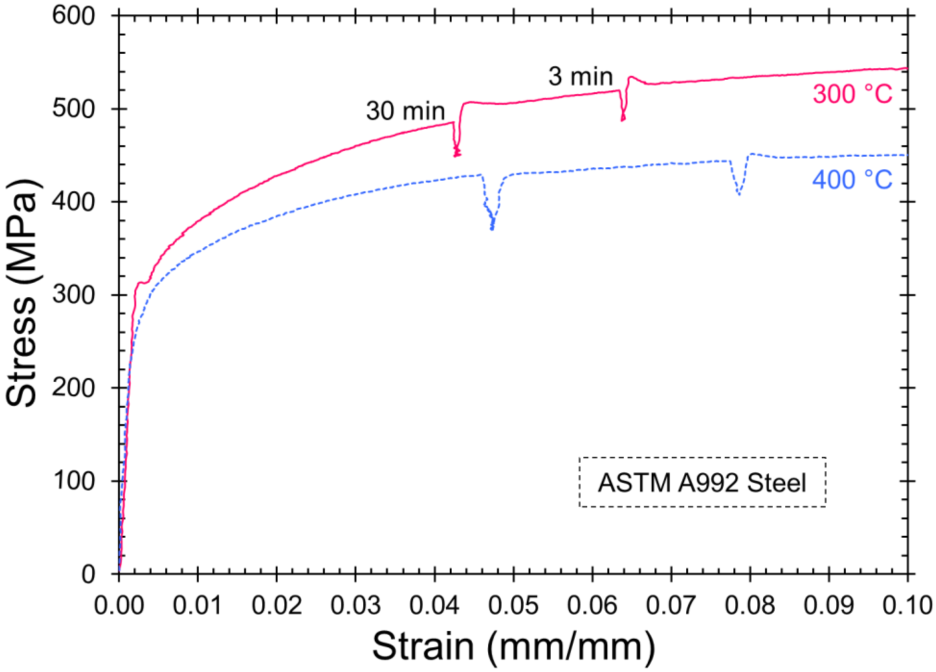

Fig. 141. Stress-strain curves with constant strain intervals for ASTM A992 steel at elevated temperatures [Lee et al. 2013].

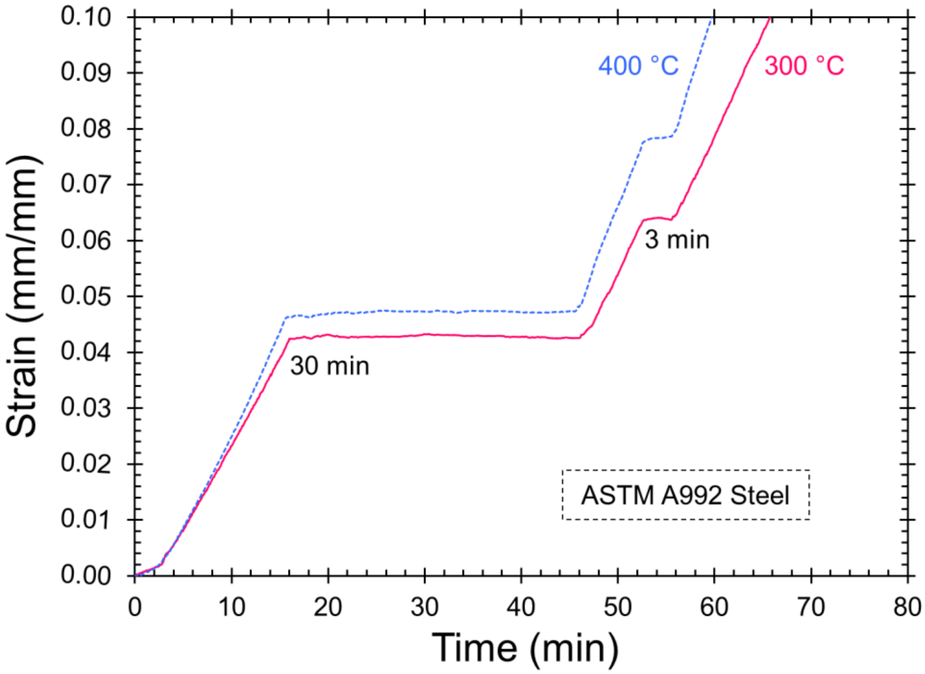

Fig. 142. Strain-time histories with the two constant strain intervals for ASTM A992 steel at elevated temperatures [Lee et al. 2013].

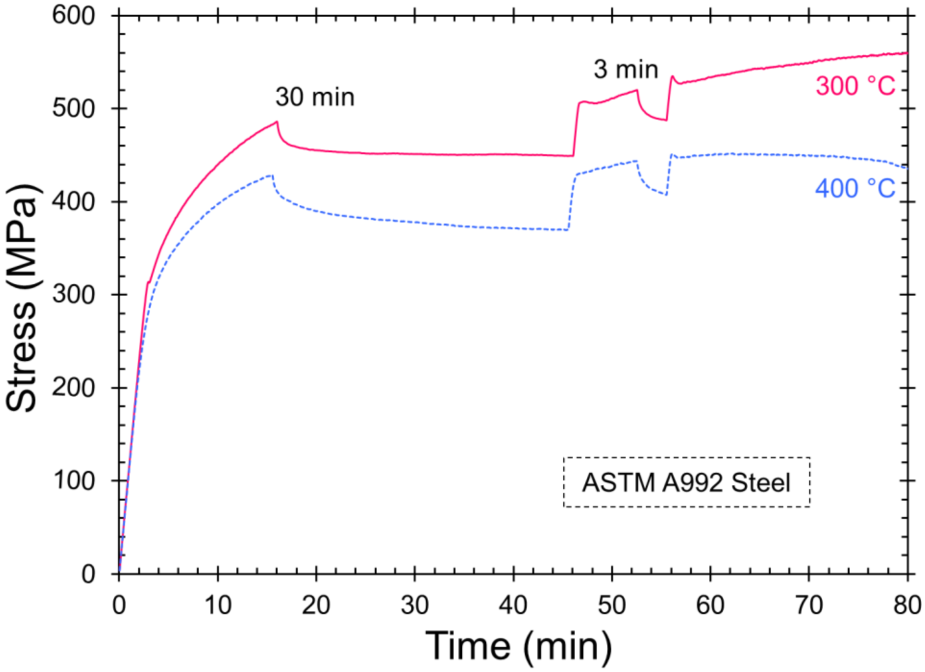

Fig. 143. Stress-time histories with the two stress relaxation intervals for ASTM A992 steel at elevated temperatures [Lee et al. 2013].

As observed in Figs. 141, 142, and 143, the phenomenon of stress relaxation of steel is influenced by the magnitude of applied strains and temperatures as well as the duration of exposure to elevated temperatures. Figures 141, 142, and 143 also indicate that the stress relaxation phenomenon for steel can occur at lower temperatures of 300 °C and 400 °C, which can be developed within protected steel members in fire. Moreover, Figs. 141, 142, and 143 represent stress relaxation of steel at constant elevated temperatures. As seen in Fig. 140, the stress relaxation for the bolts of shear tab connections is more significant since these bolts are subjected to increasing temperatures in fire exposure.

In the absence of material models capable of describing explicit time-dependent inelastic behavior of structural bolts at elevated temperatures, the bolt stress relaxations observed in Fig. 140 cannot be fully modeled. In fact, the simulation failed to converge as a result of its inability to model bolt stress relaxation that can potentially allow bolts to withstand the imposed forces and deformations during the fire exposure.

6. Summary and Conclusions

This report summarized the development and validation of a computational model for the analysis of steel gravity frames with composite floor systems exposed to fire. The computational model included detailed representation of the components of the composite floor system including the concrete slab with profiled steel decking, primary and secondary steel beams and supporting columns, shear studs, and connections. The computational model was developed using the general-purpose finite element program LS-DYNA using an explicit solution algorithm. Description of the computational model along with the modeling approach were presented in Chapter 3. Specifically, the material modeling, the composite shell representation for the floor slab, and the application of thermal and mechanical loadings were discussed. The validation of the computational model using the data from the NIST NFRL CF2 Test along with representative results from the analysis were detailed in Chapters 4 and 5.

This section summarizes important observations from the computational study of the steel gravity frame structure with composite floor slab exposed to a compartment fire, with upper-layer gas temperatures similar to the temperature-time curve defined in the ASTM E119 standard [ASTM International 2022c]. It is important to note that although the upper-layer gas temperature history was similar to that prescribed in an ASTM E119 furnace test [ASTM International 2022c], the test conditions in the NIST NFRL CF2 Test were much more representative of a building fire, with mechanical loading applied in conjunction with the fire-induced heating and with realistic boundary conditions for the composite floor slab provided by the surrounding bays of the test structure. The limitations of the current modeling approach are also discussed in this section, and the section ends with some recommendations for future research.

6.1. Summary of Major Observations

Using the results from the validated computational approach presented in this report, the following key observations were made:

1) Overall, good agreement was observed between the experimental and the computational results. The simulation adequately predicted the deformations (displacements) of different

components of the composite floor assembly (i.e., steel beams, connections, and composite slab). The accuracy of the model predictions was quantified as the percentage error in the difference between the predicted and measured displacements at the end of the simulation, which occurred after 130 minutes of fire exposure corresponding to the maximum fire temperature in the CF2 Test. Specifically, the vertical displacement at the middle of the fire-tested slab predicted by the computational modeling approach agreed with that observed in the NFRL CF2 Test with the maximum percent deviation of 7 %. The maximum percent deviation between the experimental and computational vertical displacements at the midspan of W16×31 beams and W18×35 girders was about 12 % and 44 %, respectively. Additionally, the maximum percent deviation between the experimental and computational horizontal (lateral) displacement of the first-story columns of the fire-tested floor, and the perimeter columns outside of the fire-tested bay was about 1 % and 29 %, respectively.

2) The computational model was able to predict the deflections of the W16×31 beams and W18×35 girders of the fire-tested composite floor. The model was further able to capture the deformation-related failure mechanisms observed in the experiment, such as web local buckling, lateral distortional buckling of steel beams, and cracking of the concrete slab.

3) The model was able to capture the influences of thermal restraint and showed that the response of W16×31 beams of the test bay to restrained thermal expansion was governed by large axial and lateral displacements, and high axial forces. The north W16×31 beam, with the highest degree of thermal restraint, developed the largest axial loads during the exposure to standard fire temperatures. The south W16×31 beam exhibited the largest lateral (out-of-the web plane) displacements during the exposure to standard fire temperatures.

4) The computational model showed that the thermal expansion of W16×31 beams induced large lateral displacements in the W18×35 girders. As a result, the extended shear tab connections between the W18×35 girders and W12×106 columns experienced significant out-of-plane bending of shear tab plates and bending of bottom bolts.

5) Both the W16×31 beams and W18×35 girders experienced lateral deformation resembling that of lateral distortional buckling, as well as web local buckling during the exposure to

elevated temperatures. The model was able to capture the relaxation of stresses in the bolts that are adjacent to the area of the beam where local buckling occurred.

6) Significant deformations of connection plates and bolts were observed following the CF2 Test fire exposure that included the cooling phase. After approximately 130 minutes of fire exposure, close to the maximum gas temperature in the CF2 Test, the computational analysis terminated due to a failure of convergence in the modeling of the bottom bolts of the extended shear tab connections at the south ends of the east and west W18×35 girders. Therefore, the simulation did not consider the cooling phase of the fire in CF2 Test. This convergence issue is potentially due to the significant relaxation of stresses in the bottom bolt of the extended shear tab connection at the south end of the east W18×35 girder. Specifically, the model was not able to capture the bolt stress relaxation since thermal creep was not explicitly considered in the material stress-strain behavior of bolts.

6.2. Limitations of the Study

The developed computational approach to model the behavior of composite floor systems in fire has the following limitations:

1) Rather than performing a coupled thermal-structural analysis, this study used a temperature-dependent structural analysis approach in which measured temperature-time histories obtained from the fire experiment were prescribed as nodal temperature histories in the finite element model.

2) The results and observations from the validated computational model are limited to fire conditions with rising temperatures since the analysis terminated due to convergence problems when the upper-layer gas temperature was near the maximum value. Consequently, the computational approach has not been validated for the cooling phase of the fire exposure.

3) The results and observations from the validated computational model are limited to the specific type of connections used in the full-scale experiment. Specifically, the computational approach was validated for a steel frame with shear tab connections.

4) The steel columns in the composite steel frame of the NIST NFRL CF2 Test were not subjected to thermal loads. Thermal loading on columns can have an impact on the overall stability and the governing failure mechanisms of the composite steel frame systems.

5) Thermal creep or time-dependent plasticity was not considered explicitly in the temperature-dependent material models for structural steel, bolts, shear studs, and reinforced concrete. Explicit modeling of creep could enhance the robustness of the proposed computational methodology, as specifically discussed in the context of stress relaxation in bolts of shear tab connections.

6.3. Conclusions and Recommendations

Observations, results, and comparison between the simulation and the experiment indicate that:

1) Under fire exposure, steel beams and girders experience significant lateral displacements. These displacements create demands on the composite slab and on the connections, and potentially impact the stability of composite steel-framed buildings. More work is needed to understand and characterize lateral stability-related failures of composite framing members.

2) The lateral displacement of girders subjected to rising fire temperatures imposes significant deformation demands on the girder-to-column connections. In addition, lateral and axial displacements of secondary beams exposed to fire result in significant deformation and force demands on the beam-to-column connections. Further research is needed to better understand and characterize connection behavior in steel-composite frame buildings, specifically during the cooling phase of the fire.

3) During exposure to the rising fire temperatures, connection temperatures were significantly lower than the connecting beam and girder temperatures in the NIST NFRL CF2 Test. During the heating phase of the fire, temperature rise in the connections was slower than in the connecting beams and girders due to the greater concentration of steel mass (additional plates, bolts, etc.), thicker layers of SFRM, lesser exposure to heat, and higher capacity for heat dissipation in the connection region. These conditions also resulted in a slower cooling rate for the connections than for the connecting beams during the cooling phase of the fire. Future research is needed to better understand these disparities in temperature between the

connections and the beams and their impact on the overall stability of multi-story composite steel-framed buildings during the cooling phase of fire.

4) The robustness of the proposed computational approach in predicting the behavior of composite steel-framed buildings can be enhanced through parametric studies. Specifically, parametric analyses are needed to provide a better understanding of the contribution of the columns (particularly in multi-story buildings) and the thermal restraint provided by the cooler parts of the structure to the overall stability of composite floor systems exposed to fire.

5) Thermal creep was shown to impact the load and deformation capacity of steel members (e.g., buckling of columns [Morovat 2014]) and connections (e.g., stress relaxation of bolts [Morovat et al. 2018]). Further research is needed to better characterize the time-dependent or creep effects on the stress-strain responses of structural steel and bolts to elevated temperatures in fire.

References

[1] ANSI/AISC 360 (2016) *Specification for Structural Steel Buildings* (American Institute of Steel Construction, Chicago, IL).

[2] American Society of Civil Engineers (2017) *ASCE 7 - Minimum Design Loads and Associated Criteria for Buildings and Other Structures* (American Society of Civil Engineers, Reston, VA).

[3] ASTM International (2019) *ASTM A36/A36M - Standard Specification for Carbon Structural Steel* (ASTM International, West Conshohocken, PA). https://doi.org/10.1520/A0036_A0036M-19

[4] ASTM International (2021) *ASTM A572/A572M - Standard Specification for High-Strength Low-Alloy Columbium-Vanadium Structural Steel* (ASTM International, West Conshohocken, PA). https://doi.org/10.1520/A0572_A0572M-21E01

[5] ASTM International (2022a) *ASTM A992/A992M - Standard Specification for Structural Steel Shapes* (ASTM International, West Conshohocken, PA). https://doi.org/10.1520/A0992_A0992M-22

[6] ASTM International (2022b) *ASTM E8/E8M - Standard Test Methods for Tension Testing of Metallic Materials* (ASTM International, West Conshohocken, PA). https://doi.org/10.1520/E0008_E0008M-22

[7] ASTM International (2022c) *ASTM E119 - Standard Test Methods for Fire Tests of Building Construction and Materials* (ASTM International, West Conshohocken, PA). https://doi.org/10.1520/E0119-22

[8] ASTM International (2022d) *ASTM F3125/F3125M - Standard Specification for High Strength Structural Bolts and Assemblies, Steel and Alloy Steel, Heat Treated, Inch Dimensions 120 ksi and 150 ksi Minimum Tensile Strength, and Metric Dimensions 830 MPa and 1040 MPa Minimum Tensile Strength* (ASTM International, West Conshohocken, PA). https://doi.org/10.1520/F3125_F3125M-22

[9] Breunese A, Roosefid M, Franssen JM, Zilli G, Zhao B, Hanus F, Koutlas G (2011) *Connections of Steel and Composite Structures under Natural Fire Conditions (COSSFIRE)* (European Commission, Directorate-General for Research and Innovation, Luxembourg, Luxembourg), Publications Office EUR 25046. https://data.europa.eu/doi/10.2777/16400

[10] British Steel (1999) *The Behaviour of Multi-Storey Steel Framed Buildings in Fire* (British Steel plc, Swinden Technology Centre, South Yorkshire, United Kingdom).

[11] CEN EN 1992-1-2 (2004) *Eurocode 2, Design of Concrete Structures – Part 1-2: General Rules – Structural Fire Design* (European Committee for Standardization, Brussels, Belgium).

[12] Choe L, Ramesh S, Dai X, Hoehler M, Bundy M, Bryant R, Story B, Chakalis A, Chernovsky A (2021) *Fire Resilience of a Steel-Concrete Composite Floor System: Full-Scale Experimental Evaluation for U.S. Prescriptive Approach with a 2-Hour Fire-Resistance Rating (Test #1)* (National Institute of Standards and Technology, Gaithersburg, MD), NIST Technical Notes (TN) NIST TN 2165. https://doi.org/10.6028/NIST.TN.2165

[13] Choe L, Hoehler M, Bundy M, Bryant R, Story B, Chakalis A, Chernovsky A, Ramesh S, Dai X (2022) *Fire Resilience of a Steel-Concrete Composite Floor System: Full-Scale Experimental Evaluation for Influence of Slab Reinforcement (Test #2)* (National Institute of Standards and Technology, Gaithersburg, MD), NIST Technical Notes (TN) NIST TN 2203. https://doi.org/10.6028/NIST.TN.2203

[14] Crocker J, Chambers J (2004) Single plate shear connection response to rotation demands imposed by frames undergoing cyclic lateral displacements. *Journal of Structural Engineering* 130(6):934-941. https://doi.org/10.1061/(ASCE)0733-9445(2004)130:6(934)

[15] Dara S (2015) Behavior of the shear studs in composite beams at elevated temperatures. Ph.D. Thesis. (University of Texas at Austin, Austin, TX). Available at http://hdl.handle.net/2152/33269

[16] Dieter GE (1976) *Mechanical Metallurgy* (McGraw-Hill, New York, N.Y.), 2nd Ed.

[17] Franssen JM, Cooke GME, Latham DJ (1995) Numerical simulation of a full scale fire test on a loaded steel framework. *Journal of Constructional Steel Research* 35(3):377-408. https://doi.org/10.1016/0143-974X(95)00010-S

[18] International Code Council (2021) *IBC 2021 – International Building Code* (International Code Council, Washington, DC).

[19] Jiang J, Main JA, Sadek FH, Weigand JM (2017) *Numerical Modeling and Analysis of Heat Transfer in Composite Slabs with Profiled Steel Decking* (National Institute of Standards and Technology, Gaithersburg, MD), NIST Technical Notes (TN) NIST TN 1958. https://doi.org/10.6028/NIST.TN.1958

[20] Jiang J, Main JA, Weigand JM, Sadek FH (2020a) Reduced-order modeling of composite floor slabs in fire. I: heat transfer analysis. *Journal of Structural Engineering* 146(6):04020080. https://doi.org/10.1061/(ASCE)ST.1943-541X.0002650

[21] Jiang J, Main JA, Weigand JM, Sadek F (2020b) Reduced-order modeling of composite floor slabs in fire. II: thermal-structural analysis. *Journal of Structural Engineering* 146(6):04020081. https://doi.org/10.1061/(ASCE)ST.1943-541X.0002607

[22] Lee J, Morovat MA, Hu G, Engelhardt MD, Taleff EM (2013) Experimental Investigation of Mechanical Properties of ASTM A992 Steel at Elevated Temperatures. *Engineering Journal*, American Institute of Steel Construction 50(4):249-272.

[23] Lou G, Wang C, Jiang J, Jiang Y, Wang L, Li G (2018) Fire tests on full-scale steel portal frames against progressive collapse. *Journal of Constructional Steel Research* 145(6):137-152. https://doi.org/10.1016/j.jcsr.2018.02.024

[24] LSTC (Livermore Software Technology Corporation) (2016) *LS-DYNA Keyword User's manual, R9.0* (Livermore Software Technology Corporation, Livermore, CA).

[25] Main JA, Sadek FH, Weigand JW, Jiang J, Choe L, Ramesh S, Hoehler MS, Gross JL (2017) Performance of Composite Beams in Fire: Pre-test Analysis of Full-scale Experiments. *Proceedings, Eighth International Conference on Composite Construction in Steel and Concrete*, American Institute of Steel Construction, 702-713.

[26] Morovat MA (2014) Creep buckling behavior of steel columns subjected to fire. Ph.D. Thesis. (University of Texas at Austin, Austin, TX). Available at http://hdl.handle.net/2152/29083

[27] Morovat MA, El Ghor AH, Hantouche EG (2018) Time-Dependent Response of Flush Endplate Connections to Fire Temperatures. *Journal of Structural Engineering* 144(4): 04016178. https://doi.org/10.1061/(ASCE)ST.1943-541X.0002006

[28] Mwangi S (2017) Why Broadgate Phase 8 composite floor did not fail under fire: Numerical investigation using ANSYS® FEA code. *Journal of Structural Fire Engineering* 8(3):238-257. https://doi.org/10.1108/JSFE-05-2017-0032

[29] Ollgaard JG, Slutter RG, Fisher JW (1971) Shear strength of stud connectors in lightweight and normal-weight concrete. *Engineering Journal*, American Institute of Steel Construction 8(2):55-64.

[30] Ramesh S, Choe L, Seif MS, Hoehler MS, Grosshandler WL, Sauca A, Bundy M, Luecke WE, Bao Y, Klegseth M, Chen G., Reilly J, Glisic B (2019) *Compartment Fire Experiments on Long-Span Composite-Beams with Simple Shear Connections Part 1: Experiment Design and Beam Behavior at Ambient Temperature* (National Institute of Standards and Technology, Gaithersburg, MD), NIST Technical Notes (TN) NIST TN 2054. https://doi.org/10.6028/NIST.TN.2054

[31] Ramesh S, Choe L (2022) Structural integrity of composite floors in fire: A comparison of two large-scale experiments with varying slab reinforcement. *Fire Safety Journal* 134(12): 103669. https://doi.org/10.1016/j.firesaf.2022.103669

[32] Rex CO, Easterling WS (2003) Behavior and modeling of a bolt bearing on a single plate. *Journal of Structural Engineering* 129(6):792-800. https://doi.org/10.1061/(ASCE)0733-9445(2003)129:6(792)

[33] Richard RM, Abbott BJ (1975) Versatile elastic-plastic stress-strain formulation. *Journal of Engineering Mechanics* 101(EM4):511-515.

[34] Seif MS, Choe L, Main JA, Zhang C, Weigand JM, Gross JL, Sadek FH, McColskey D, Luecke WE (2016a) *Temperature-Dependent Material Modeling for Structural Steels: Formulation and Application* (National Institute of Standards and Technology, Gaithersburg, MD), NIST Technical Notes (TN) NIST TN 1907. https://doi.org/10.6028/NIST.TN.1907

[35] Seif MS, Main JA, Weigand JM, McAllister TP, Luecke WE (2016b) Finite element modeling of structural steel component failure at elevated temperatures. *Structures* 6(5):134-145. https://doi.org/10.1016/j.istruc.2016.03.002

[36] Seif MS, Peixoto R, Weigand JM, Main JA, Vieira L (2018) *Shear Behavior of High-strength Bolts at Elevated Temperatures: Testing and Formulation of Reduced-order Model* (National Institute of Standards and Technology, Gaithersburg, MD), NIST Technical Notes (TN) NIST TN 1978. https://doi.org/10.6028/NIST.TN.1978

[37] Shyam-Sunder S, Gann RG, Grosshandler WL, Lew HS, Bukowski RW, Sadek FH, Gayle FW, Gross JL, McAllister TP, Averill JD, Lawson JR, Nelson HE, Cauffman SA (2005) *Federal Building and Fire Safety Investigation of the World Trade Center Disaster: Final Report of the National Construction Safety Team on the Collapses of the World Trade Center Towers* (National Institute of Standards and Technology, Gaithersburg, MD), NIST

National Construction Safety Team Act Reports (NCSTAR) NIST NCSTAR 1. https://doi.org/10.6028/NIST.ncstar.1

[38] The MathWorks, Inc. (2023) *MATLAB version: 9.14.0 (R2023a).* (The MathWorks, Inc., Natick, MA). https://www.mathworks.com

[39] Wald F, Simões da Silva L, Moore DB, Lennon T, Chladná M, Santiago A, Beneš M, Borges L (2006) Experimental behaviour of a steel structure under natural fire. *Fire Safety Journal* 41(7):509-522. https://doi.org/10.1016/j.firesaf.2006.05.006

[40] Wang YC (2000) An analysis of the global structural behaviour of the Cardington steel-framed building during the two BRE fire tests. *Engineering Structures* 22(5):401-412. https://doi.org/10.1016/S0141-0296(98)00127-8

[41] Wang YC (2002) *Steel and Composite Structures: Behaviour and Design for Fire Safety* (Spon Press, New York, N.Y.), 1st Ed.

[42] Weigand JM (2014) The Integrity of Steel Gravity Framing System Connections Subjected to Column Removal Loading. Ph.D. Thesis. (University of Washington, Seattle, WA). Available at http://hdl.handle.net/1773/26518

[43] Weigand JM (2017) Component-Based Model for Single-Plate Shear Connections with Pretension and Pinched Hysteresis. *Journal of Structural Engineering* 143(2): 04016178. https://doi.org/10.1061/(ASCE)ST.1943-541X.0001662

[44] Weigand JM, Peixoto R, Vieira LCM, Main JA, Seif MS (2018) An empirical component-based model for high-strength bolts at elevated temperatures. *Journal of Constructional Steel Research* 147(8):87-102. https://doi.org/10.1016/j.jcsr.2018.03.034

[45] Yu H, Burgess IW, Davison JB, Plank RJ (2009) Experimental investigation of the behaviour of fin plate connections in fire. *Journal of Constructional Steel Research* 65(3):723-736. https://doi.org/10.1016/j.jcsr.2008.02.015

[46] Zhang C, Pintar A, Weigand JM, Main JA, Sadek FH (2021) Impact of variability in thermal properties of SFRM on steel temperatures in fire. *Fire Safety Journal* 123(7): 103361. https://doi.org/10.1016/j.firesaf.2021.103361

[47] Zhao B, Kruppa J (1997) *Fire resistance of composite slabs with profiled steel sheet and of composite steel concrete beams: Part 2: Composite beams* (European Commission, Directorate-General for Research and Innovation, Luxembourg, Luxembourg), Publications Office EUR 16822.

[48] Zhao B, Roosefid M, Vassart O (2008) Full Scale Test of a Steel and Concrete Composite Floor Exposed to ISO Fire. *Proceedings of the Fifth International Conference on Structures in Fire (SiF'08)*, (SiF 2008 Organising Committee, Singapore), pp 539-550.